UNIVERSITÀ DI PISA

FACULTY OF ENGINEERING

Master of Science in Nuclear Engineering

EXPERIMENTAL INVESTIGATION ON THE DYNAMIC BEHAVIOUR OF SPREADING DROPLETS

Candidate:

Giacomo Saccone

University of Pisa Tutor:

Prof. Ing. Paolo Di Marco, Prof. Walter Ambrosini

CEA tutors:

Dr. Matteo Bucci; Dr. Benjamin Cariteau

“Sentir, riprese, e meditar: di poco
Esser contento: da la meta mai
Non torcer gli occhi: conservar la mano
Pura e la mente: de le umane cose
Tanto sperimentar, quanto ti basti
Per non curarle: non ti far mai servo:
Non far tregua coi vili: il santo Vero
Mai non tradir: nè proferir mai verbo,
Che plauda al vizio, o la virtù derida.”

In morte di Carlo Imbonati,
Alessandro Manzoni

Al Presidio di Libera Pisa « Giancarlo Siani »,

Alle vittime del terrorismo e di tutte le mafie,

A mia sorella, Silvia,

Part I : Introduction to the work

1 Introduction 7

Why do we need to understand the dynamics of contact angles? 7

Aim of the present work 10

2 State of the art 11

A short introduction to wetting phenomena 11

Dynamic contact angles 12

Part II : Experimental activity

3 Experimental Apparatus, Operating Procedures and Test Matrix 20

Test sample 20

Injection system 22

Camera and light 22

Operating procedure 22

Test Matrix 23

Part III : Analysis of experimental results

4 Post-processing techniques 25

Common features of the post-processing codes 26

The Geometrical Code by DESTEC 28

Konduru's code 29

5 Momentum balance and dynamics of a spreading droplet 32

6 Non-dimensional vertical momentum balance and contact angle verification 42

7 Experimental technique to estimate surface tension 53

8 Contact angle 56

9 Momentum balance within radial approach 60

10 Energy balance 70

11 Comparison of different material behaviours 73

Insight in the least squares curve fitting theories 73

Insight in the wetting properties of the materials tested 76

Comparison of surfaces (qualitative – 1st way) 77

Comparison of surfaces (quantitative – 2nd way) 81

12 Effects of roughness 84

13 Conclusions, acknowledgement and future prospect 87

Part I: Introduction to the work

1 Introduction

Why do we need to understand the dynamics of contact angles?

Wetting and de-wetting phenomena are of major interest for both industrial and technological applications, since they have a key role in the optimization of a wide class of processes which involve momentum, heat and mass transfer.
In conventional industrial applications, they are of interest in many processes involving droplets dynamics, such as oil recovery, lubrication, liquid coating, and spray quenching. The growth and spreading of a drop is influenced by external force fields: understanding wetting or drying phenomena requires a detailed and accurate study of surface tension forces, contact angle and contact line dynamics.
In nuclear energy applications, wetting and de-wetting phenomena are essential for the understanding of boiling and condensation. These phenomena are key to determining nucleate boiling conditions, critical heat flux (CHF) and quenching, all relevant to define design, operating condition and thus safety margins of nuclear reactors.
Contact angle refers to the angle at the tree phase contact line, where the fluid meets its vapour and the solid surface; it is calculated from the liquid side. Its dynamic seems to affect every behaviour of the bubble: nucleation, spreading upon the solid surface and detachment.
The most famous correlation for fully developed nucleate boiling is probably the one proposed by Rohsenow and Griffith [1]. They suggested that the heat transfer enhancement under boiling conditions is the result of local liquid circulation in the region close to the heating surface, promoted by successive bubble detachments. The correlation reads:

$$\frac{q''_{\mathrm{nb}}}{\mu_{\mathrm{l}}\, h_{\mathrm{lg}}}\left[\frac{\gamma}{g\left(\rho_{\mathrm{l}}-\rho_{\mathrm{g}}\right)}\right]^{0.5} = \left(\frac{1}{C_{\mathrm{sf}}}\right)^{\frac{1}{\mathrm{r}}} Pr_{\mathrm{l}}^{-\frac{\mathrm{s}}{\mathrm{r}}}\left[\frac{Cp_{\mathrm{l}}\left(T_{\mathrm{w}}-T_{\mathrm{sat}}(P_{\mathrm{l}})\right)}{h_{\mathrm{lg}}}\right]^{\frac{1}{\mathrm{r}}} \tag{1}$$

where r and s for water are 0.33 and 1.0, respectively. Rohsenow and Griffith introduced an empirical constant C_{sf} to account for the material and the roughness of the boiling surface. Later, Liaw and Dhir [2] and Vachon et al. [3] identified a clear dependence between C_{sf} and the contact angle during pool boiling of water on copper. Furthermore, by varying the surface roughness, they obtained different contact angles and showed that contact angle and C_{sf} decrease as the surface is made smoother. They studied experimentally the variation of the wall heat flux with the contact angles in fully developed nucleate boiling, with heat fluxes close to CHF. Their results showed that as the surface wettability is improved, that is, as the contact angle decreases, a higher superheat is necessary to achieve the same heat flux.
More recently, Kandlikar [4] has investigated the dependence of CHF on contact angle. They have proposed a theoretical expression for CHF in which the contact angle θ appears explicitly:

$$q''_{\mathrm{chf}} = h_{\mathrm{lg}}\rho_{\mathrm{g}}^{0.5}\left(\frac{1+\cos\theta}{16}\right)\left[\frac{2}{\pi}+\frac{\pi}{4}(1+\cos\theta)\right]^{0.5}\left[\gamma\, g\left(\rho_{\mathrm{l}}-\rho_{\mathrm{g}}\right)\right]^{0.5} \tag{2}$$

Their experiments confirm that a low contact angle (highly wetting liquid) will result in a higher value of CHF, while a high contact angle, such as a non-wetting surface, will result in drastic reduction in CHF, as also confirmed by Costello and Frea [6].
Hai Trieu Phan et Al. [7], [12], Sher and Hetsroni [8], Mukherjee and Kandlikar [9][11], Son, Dhir e Ramanujapu [10], Kandlikar and Steinke [13], Chandra et al. [14], Liao et al. [15], all investigated the effect of contact angle on heat transfer, both theoretically and experimentally, confirming the importance of this parameter. As affirmed by Rohsenow and Griffith [1], bubble detachment creates a near-wall-turbulence, which improves heat transfer. Furthermore, the bubble detachment frequency directly affects the heat exchange and so does the average bubble diameter at departure, as shown in Figure 1 through Figure 4.

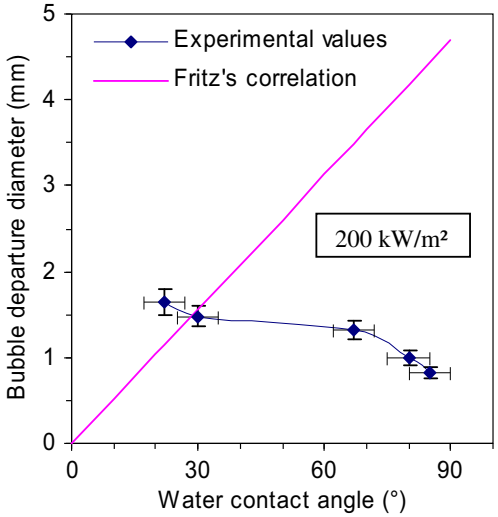

Figure 1: Bubble departure diameter vs. water contact angle (figure from [4])

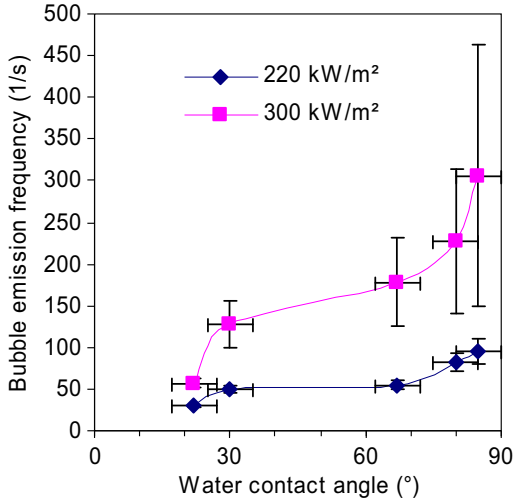

Figure 2: Bubble emission frequency vs. water contact angle (figure from [4])

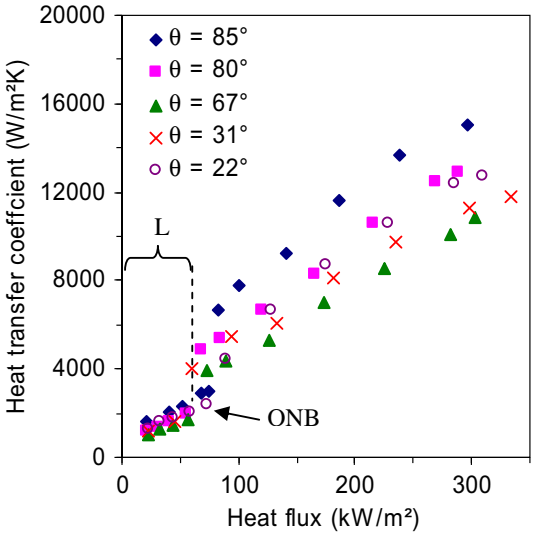

Figure 3: Heat transfer coefficient vs. heat flux for different contact angles (figure from [4])

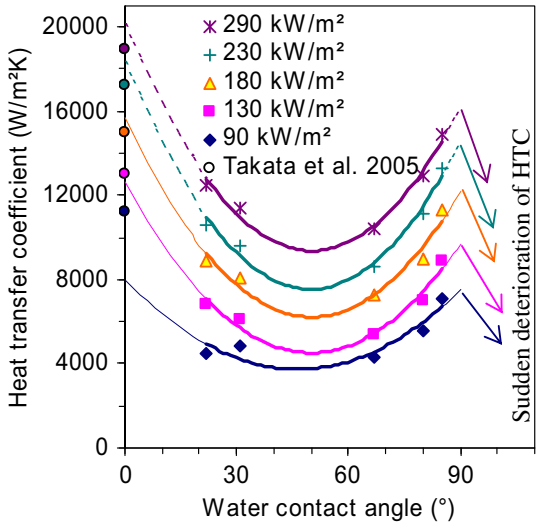

Figure 4: Heat transfer coefficient vs. water contact angle for different heat fluxes (figure from [4])

Kandlikar et al. [4] also investigated the dynamic of a single vapour bubble, growing and detaching. They showed that the dynamic of the contact angle and the triple line play a key role in the characterization of boiling heat transfer. First, as the vapour bubble starts growing (see Figure 5), the spreading of the vapour bubble over the surface is accompanied by a receding of the liquid

(receding contact angle), and a dry spot results from the evaporation of the liquid micro-layer close to the surface. Then, as the vapour bubble is lifted from the surface, the liquid advances (advancing contact angle).

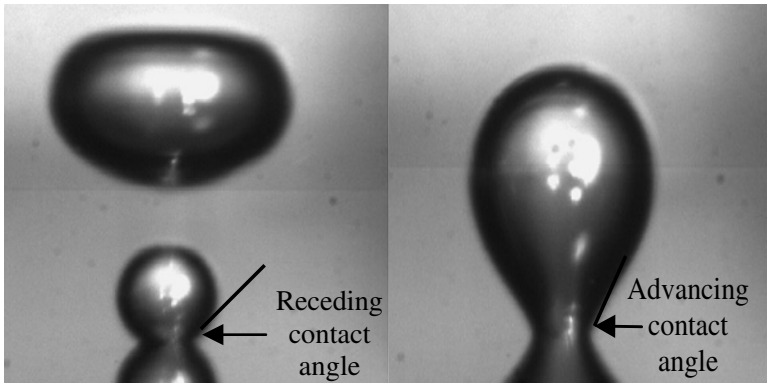

Figure 5: Receding and advancing contact angles

In this process, the dynamic of the contact angle is essential to determine the bubble detachment volume and the bubble detachment frequency, and consequently the effectiveness of the heat transfer mechanism. Sample results by Ramanujapu and Dhir [5] are reported in Figure 6. The dynamic contact angle during the bubble life is shown as a function of triple line velocity and wall superheat, on a copper surface.

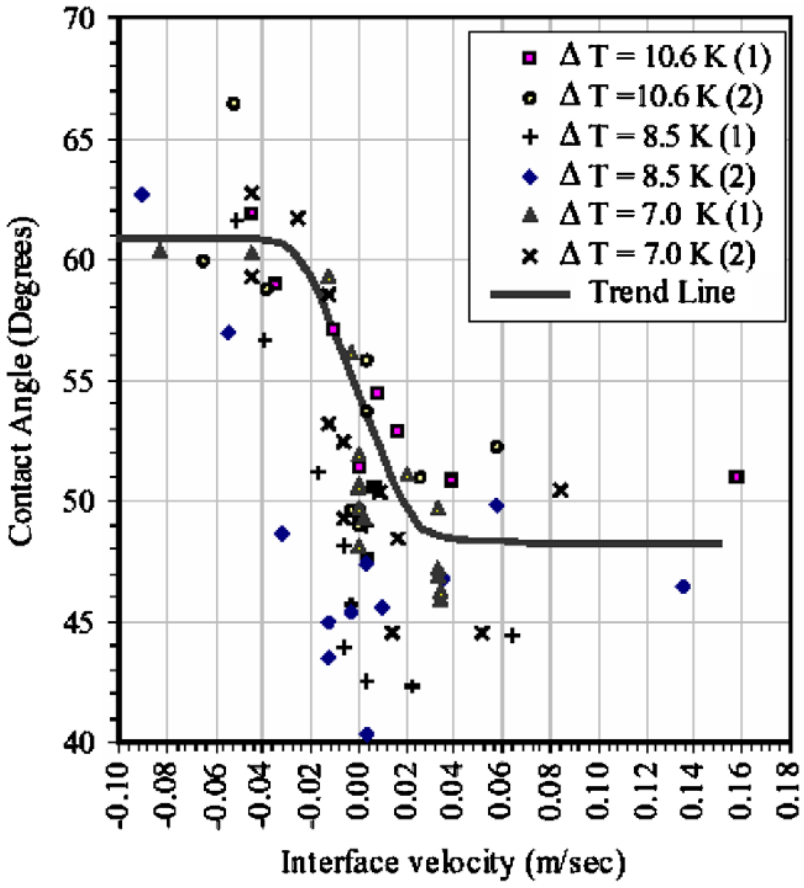

Figure 6: Dynamic contact angle vs. triple line velocity (figure from [5])

Aim of the present work

This work is aimed at improving the understanding of dynamic contact angles. This phenomenon is investigated experimentally by controlling the growth a liquid droplet on a surface. The correlation between contact angle and triple line velocity has been identified, with a particular insight into the effect of the injection flow rate.

A literature review on dynamic contact angles is presented in Chapter 2. Publications on the topic are divided in three categories, depending on the approach adopted to correlate contact angle and triple line velocity: completely empirical, semi-empirical or theoretical and numerical.
A detailed description of the experimental apparatus and operating procedures is reported in Chapter 3. Post-processing techniques are detailed in Chapter 4. Then, the analysis of experimental results is presented in the Part III:.

2 State of the art

A short introduction to wetting phenomena

When a drop of liquid is placed on a surface, its shape evolves until it reaches an equilibrium state. This process depends mostly on properties of the surface and on external conditions (temperature and humidity). The role of interfacial forces acting on the three-phase contact line is also very important.
The first study on wetting phenomena was probably reported by Young [16], giving the name to the well-known Young's equation; resulting from the well-known equation expressing equilibrium of contact line along the surface:

$$\gamma_{SV} = \gamma_{SL} + \gamma_{LV} \cos\theta \tag{3}$$

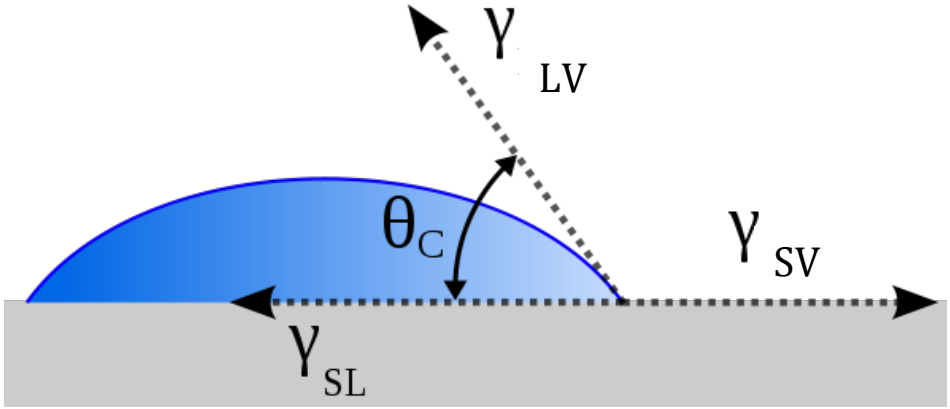

Figure 7: Sketch of a sessile droplet

Where the meaning of the different terms is clarified by Figure 7. We distinguish three phases: the liquid *L*, the solid surface *S* and the surrounding atmosphere *V*. θ is the equilibrium contact angle.
The contact angle can be between $\theta = 0$ e $\theta = 180°$ (See Figure 8). The former case corresponds to perfect wettability; the latter corresponds to perfect non-wettability. More often, as for the surfaces used in this study and for most metallic surfaces, partial wetting occurs.

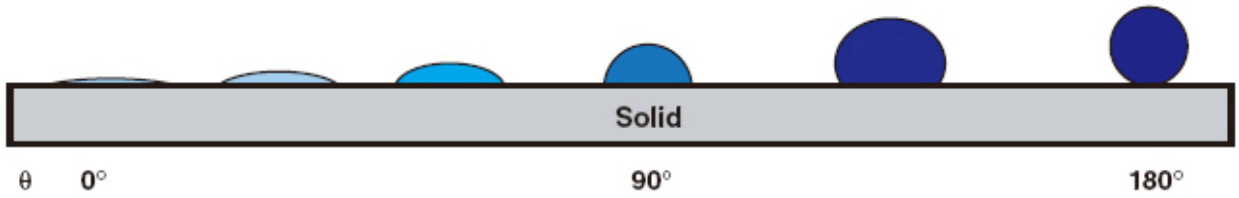

Figure 8: Behaviour of a sessile droplet on a surface, from hydrophilic (left) to hydrophobic (right)

Furthermore, it has to be noticed that real surfaces are neither perfectly smooth nor totally homogeneous. This difference with the ideal case is at least partly responsible of contact angle hysteresis. In reality, the static contact angle can be within the receding contact angle, θ_r, and the advancing contact angle, θ_a, defined as the ultimate contact angles for which the liquid droplet start to advance or recede on the surface, respectively.

Even more challenging is the characterization of contact angle when the triple line moves advancing or receding on the solid surface, as in the case of spreading liquid droplets or even boiling phenomena.

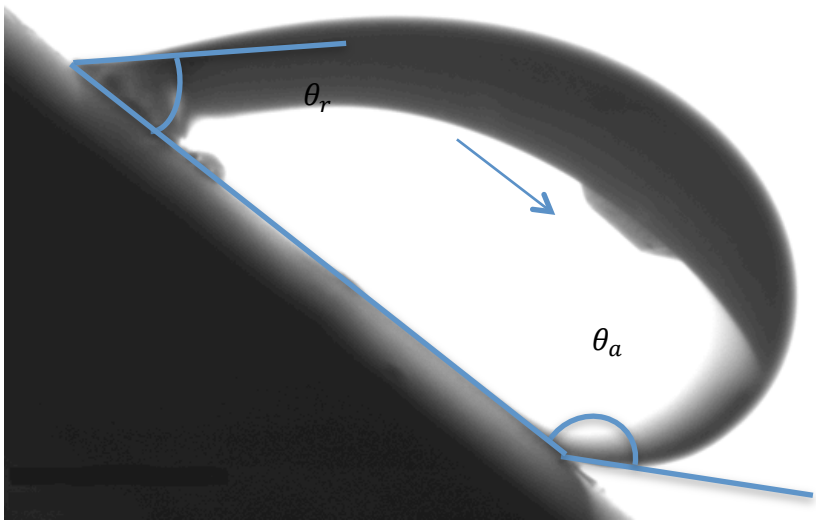

Figure 9: Advancing θ_a and receding θ_r contact angles on a tilted surface

Dynamic contact angles

The phenomena of droplets spreading upon a surface have been extensively studied since the end of 1960s. Despite its apparent simplicity, the problem of the accurate determination of the dynamic contact angle of a liquid droplet spreading upon a surface is very difficult to tackle. For this reason considerable efforts have been dedicated to it during the last forty years.
A considerable amount of correlations and models for droplet formation, spreading and triple line velocity are available nowadays. Most of them describe the phenomenon in terms of some dimensionless numbers:

- Eötvös number (also known as Bond number)

$$Eo = \frac{g\ D^2\ \Delta\rho}{\gamma} \tag{4}$$

- Weber number

$$We = \frac{\rho\ v^2 D}{\gamma} \tag{5}$$

- Capillary number

$$Ca = \frac{\mu\ v}{\gamma} \tag{6}$$

The Eötvös number is the ratio of gravity to interfacial forces. The Weber number is the ratio of inertial forces to interfacial forces at the liquid-gas interface. The Capillary number is the ratio of viscous forces to interfacial forces at the liquid-gas interface.
An accurate literature review has been carried out to determine the most significant correlations and theories, together with the experimental techniques and the methodology of analysis adopted in these studies, spanning over a period of 50 years. In fact, the approaches to the phenomenon have changed with time. In the past the most common approach was to correlate the contact angle with the triple line velocity. Hoffman [17], Jiang et al. [18], Seeberg and Berg [19], Bracke et al. [20], Gokhale et al. [21], Hocking [22],[23] and Tanner [24] adopted this strategy. All these authors developed correlations based on experimental measurements, using different experimental techniques: capillary tubes, but also evaporation and condensation, and eventually impinging droplets, which has been more and more used in the more recent years.
A summary of correlation and experimental techniques proposed by the different authors is reported in Table 1, where θ_d is the dynamic contact angle.

Author	**Type**		**Experimental Technique**
Tanner [24]	Theoretical	$\theta_d^2 - \theta^2 = K\ Ca$ (7)	Glass Capillary Tube
Jiang [18]	Empirical	$\frac{\cos\theta - \cos\theta_d}{\cos\theta + 1} = \tanh(4.95\ Ca^{0.702})$ (8)	Glass Capillary Tube
Seeberg [19]	Empirical	$\frac{\cos\theta - \cos\theta_d}{\cos\theta + 1} = 2\ Ca^{0.5}$ (9)	Wilhelmy Plate
Bracke [20]	Empirical	$\begin{cases} \frac{\cos\theta - \cos\theta_d}{\cos\theta + 1} = 2.24\ Ca^{0.54} \\ \frac{\cos\theta - \cos\theta_d}{\cos\theta + 1} = 4.47\ Ca^{0.42} \quad \text{if } Ca \leq 10^{-2} \end{cases}$ (10)	Wilhelmy Plate
Gokhale [21]	Empirical	$U_d = 0.0002\ \theta_d^3 - 0.0029\ \theta_d^2 + 0.0197\ \theta - 0.0463$ (11)	Condensation/Evaporation
Hocking [22]	Theoretical	$\theta_d^3 - \theta^3 = 9\ Ca \ln(1/\beta)$ (12)	Thin Drop Analysis
Hocking [23]	Empirical	$\theta_d^3 - \theta^3 = 72\ Ca$ (13)	Glass Capillary Tube

Table 1: Empirical correlation for dynamic contact angles

Other authors have tried to understand the mechanism of the moving wetting line. Blake and Haynes [25] proposed the Molecular Kinetic Theory (MKT), Tanner [24] gave an important contribution founding a general tendency in contact angle behaviour during spreading, Cox [26] and Voinov [27] proposed a Hydro Dynamic Theory (HDT), Hocking [23] made a study on drops achieving equilibrium. Thanks to the works made by Bayer and Megaridis [28] and Blake [29], a short insight in the two most important theories is proposed hereafter.

Hydrodynamic theory

When Navier-Stokes Equations are solved in the proximity of a moving contact line, there is a singularity in stress at the contact line, leading the drag force to non-finite values on the solid boundary [34], [35], [36]. The stress diverges as $1/r$ when $r \rightarrow 0$ (r represents the distance along the surface from the contact line). In order to avoid this singularity, slip has been postulated to occur between the liquid and the solid surface at small distances, L_S, from the contact line. Four types of slip conditions have been postulated by different researchers [37]:

- Zero tangential stress at the solid surface within a distance L_S from the contact line and no slip for distances greater than L_S.
- Difference in tangential velocity between liquid and solid (slip velocity) proportional to the local shear velocity gradient at the solid surface.
- Slip velocity algebraically dependent upon distance from the contact line.
- Slip velocity proportional to the power of the local shear velocity gradient.

Cox [26] considered the triple line motion for a general geometry in which one fluid displaces another. The main assumptions of Cox's viscous theory are that the triple line motion is steady, the flow is entirely viscous (satisfies the Stokes Equations with Re << 1), the liquid is advancing and the surface is ideally smooth. Cox defined the macroscopic contact angle in terms of the asymptotic angle that the interface makes with the solid surface as the contact line is approached at the macroscopic (experimental) length scale (L_H). Using the interface shape close to the contact line, Cox found an expression for the macroscopic contact angle in terms of the Triple Line Velocity (TLV) V_{CL} and the microscopic contact angle θ_m, which was defined as the angle the liquid interface forms with the solid surface at distances of the order of the slip length L_S from the triple line (see Figure 10).

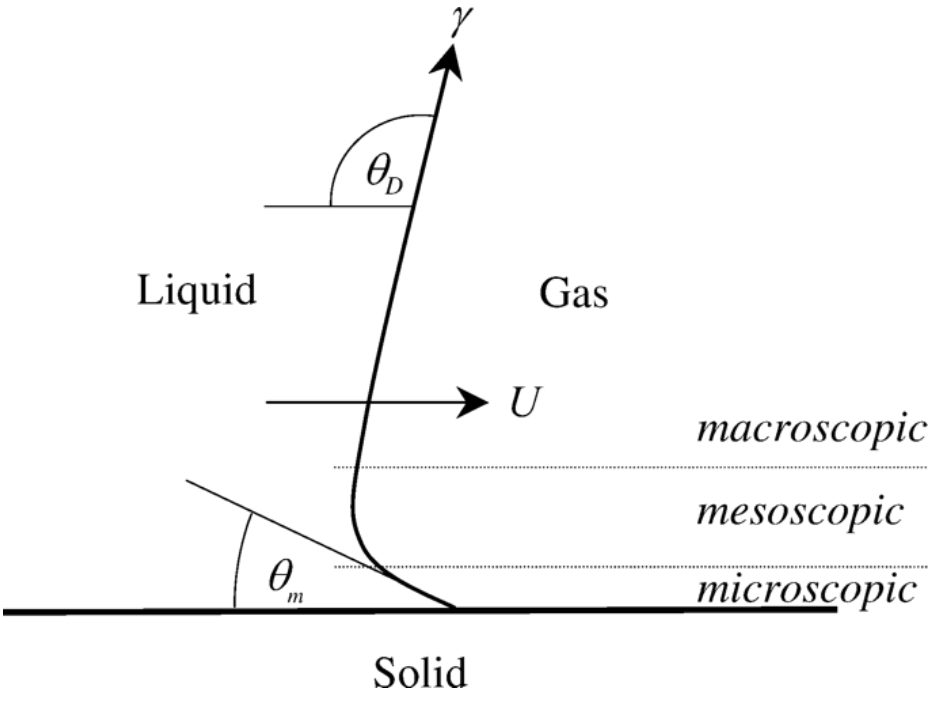

Figure 10: Dynamic and microscopic contact angles at the triple line (figure from [29])

In its simplest form, the resulting formula describing the change in the dynamic contact angle due to the viscous bending of the liquid–gas interface (Figure 10) may be written in terms of the capillary number as:

$$Ca = \frac{g_v(\theta) - g_v(\theta_d)}{\ln\left(\frac{L_H}{L_S}\right)} \tag{14}$$

where the function $g_v(\theta)$ is given by

$$g_v(\theta) = \int_0^{\theta} \frac{\phi - \sin\phi\cos\phi}{2\sin\phi} d\phi \tag{15}$$

For static or dynamics contact angles smaller than 3π/4, as in most metallic surfaces, the integrand may be approximated by $\theta^3/9$; hence Eq.14 becomes:

$$\theta_d^3 - \theta_m^3 = 9\,Ca\ln(L/L_m) \quad \text{with} \quad \theta_m = \theta \text{ and } \theta_d < 3\pi/4 \tag{16}$$

There is, as pointed out by Cox, some experimental evidence to suggest that for some systems at least, the microscopic contact angle is a constant, whose value depends only on the particular liquid and solid surface involved. However, for systems in which the microscopic contact angle could depend on the spreading velocity, owing perhaps to effects at the molecular scale, Cox's theory is still valid but with $\theta_m = f(V_{CL})$. This last assumption is supported by Voinov [27] and Ramé et al. [38]. Shikhmurzaev [39] also suggested that the contact angle is not only velocity dependent, but also sensitive to the entire flow field near the wetting line.

Molecular Kinetic Theory

Using the theory of absolute reaction rates and stating that the essential triple line motion takes place by molecules "jumping" along the solid surface from the liquid to the vapour side of the contact line [25], the macroscopic behaviour of the triple line depends on the general statistics of the molecular displacements. These displacements occur in the three-phase zone, as sketched in Figure 11.

The molecular-kinetic theory postulates that the entire energy dissipation occurs at the moving triple line. The wetting line moves with velocity V_{CL}, and the liquid shows a dynamic advancing contact angle θ_d such that $\theta_d > \theta$, where θ is the equilibrium contact angle.

According to this theory, the velocity of the triple line is determined by the frequency κ and length λ of each molecular displacement. These displacements take place at the adsorption sites on the solid surface. The length of the molecular displacement λ is influenced by the size of the liquid molecules and depends strongly on the spacing of successive adsorption sites on the target surface.

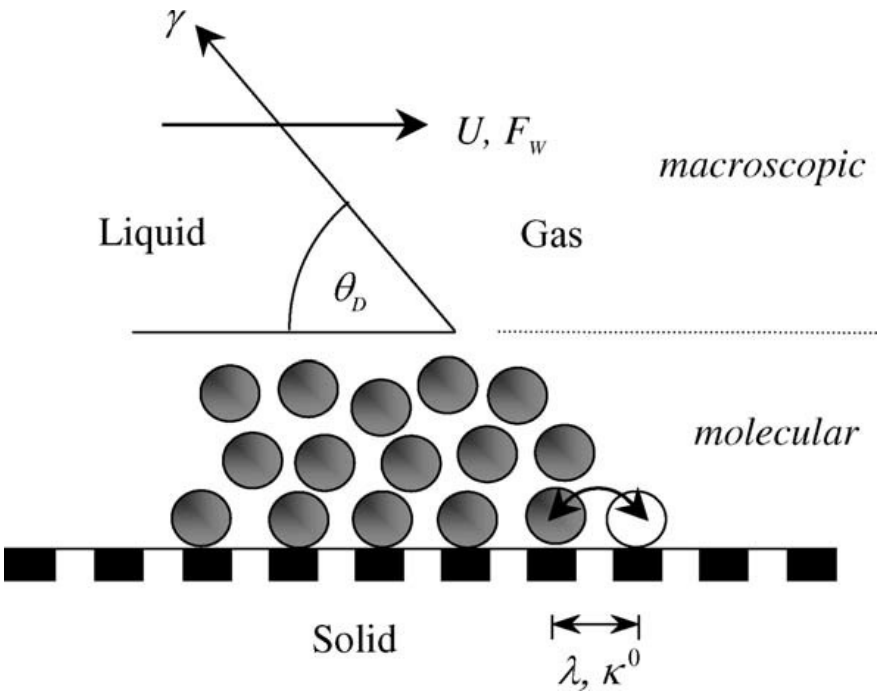

Figure 11: Motion of molecules at the contact line (figure from [29])

The triple line velocity is then given by $V_{CL} = \kappa\,\lambda$, where κ is the net frequency of molecular displacement (jump frequency). For the contact line to move, work must be done to overcome the energy barriers that prevent molecular displacement. This work is done by the surface tension force, which is:

$$\gamma[\cos\theta - \cos\theta_d] \tag{17}$$

expressed per unit length of the contact line. The work done by this force is entirely developed in the contact point zone.

Combining these ideas and using Frenkel–Eyring activated rate theory of transport in liquids, the following relationship between θ and V_{CL} was obtained by Blake & Haynes [25]:

$$V_{CL} = 2\,\kappa_w\,\lambda \sinh\left[\frac{\gamma\,\lambda^2}{2\,k\,T}(\cos\theta - \cos\theta_d)\right] \tag{18}$$

where k and T denote Boltzmann's constant and the absolute temperature respectively. The number of absorption sites per unit area on the surface (n) is related to λ by $\lambda \approx n^{-1/2}$. In addition, the equilibrium jump frequency κ_w is related to the effective molar activation energy of wetting ΔG_W by:

$$\kappa_w = \frac{k\,T}{h}\exp\left(\frac{-\Delta G_W}{N_A\,k\,T}\right) \tag{19}$$

where N_A is Avogadro's number and h stands for Planck's constant.
For viscous flow in simple liquids, ΔG_W is about 10 kJ mol^{-1}, as reported by Blake [40]. High or low values of ΔG_W imply, respectively, strong or weak dependence of the contact angle on triple line velocity.
As noted by Bayer and Megaridis [28], a limitation of κ_w expression is that it lacks of consideration for viscous losses at the triple line, although this property may have a strong influence on the dynamic contact angle. In fact, both solid-liquid interactions and viscous molecular interactions are expected to operate at the triple line while spreading over the solid surface.
A better approximation to the real mechanism of dissipation at the contact line is to combine viscous and liquid/solid interactions by writing $\Delta G_W = \Delta G_s + \Delta G_v$, where ΔG_s is the contribution arising from the influence of the surface, and ΔG_v is the contribution due to the influence of the liquid interactions at the molecular scale.
On the basis of those assumptions and with the help of the theory of absolute reaction rates [25], two new terms of interaction frequency can be identified: the first associated to fluid/molecules interaction and the other to solid/liquid interaction:

$$\mu = \frac{h}{v}\exp\left(\frac{\Delta G_v}{N_A\,k\,T}\right) \tag{20}$$

$$\kappa_s = \frac{k\,T}{h}\exp\left(\frac{-\Delta G_s}{N_A\,k\,T}\right) \tag{21}$$

$$\kappa_w = \kappa_s\frac{h}{\mu\,v} \tag{22}$$

where v is the specific volume of the fluid.
Consequently, Eq. 19 can be rewritten as:

$$V_{CL} = \frac{2\,\kappa_s\,h\,\lambda}{\mu\,v}\,\sinh\left[\frac{\gamma}{2\,n\,k\,T}(\cos\theta - \cos\theta_d)\right] \tag{23}$$

Molecular-kinetic parameters can be thus obtained by the use of this equation with nonlinear least-squares-fit analysis of the experimental data and subsequent use of Eqs. 20, 21 and 22.
According to the theory outlined above [28], if liquid molecular interactions are weak, i.e. ΔG_v is negligible, then $\kappa_w \approx \kappa_s$. If solid-liquid interactions are also weak, i.e. κ_s is large, then Eq. 23 predicts θ_d to be weakly dependent on the triple line velocity. Small equilibrium contact angles θ_e mean strong solid/liquid interactions, large equilibrium contact angles mean weak solid/liquid interactions. Furthermore, $\Delta G_s/\Delta G_v \gg 1$ means that the liquid is likely to interact strongly with the solid surface, as for example in the case of aqueous glycerol on glass. If $\Delta G_s/\Delta G_v \ll 1$, the solid-liquid interactions are instead relatively weak, as for example in the case of silicon oils on glass.
The values of $\Delta G_s/\Delta G_v$ given in Table 2 indicate that under the conditions investigated by Bayer and Megaridis [28], both liquid/liquid and liquid/solid interaction forces at the molecular level jointly retard liquid front advancement.

Despite their different hypotheses, both the hydrodynamic and molecular kinetic models have been proven to be reasonably accurate in describing the behaviour of dynamic contact angle. A hypothesis that is having more and more consideration is the possibility that both wetting-line friction and viscous dissipation play a significant role in determining the dynamics of contact angle [27][42][43]. It is clear that the microscopic contact angle will be disturbed by movement of the contact line, as well as viscous flow in the small wedge of liquid near the contact line is likely to modify the meniscus profile in this region. The real question concerns the relative importance of the two effects and how they can best be described.
Petrov et al. [42] have formulated an integrated theory by the simple expedient of combining Eq. 16 and Eq. 18, using Eq. 18 to provide the value of θ_m in Eq. 16. This has yield to an equation with three adjustable parameters, λ, κ_0 and $ln(L/L_m)$.
Not surprisingly, curve-fitting with this equation were very successful, giving in general a better agreement with experimental data than either Eq. 16 or Eq. 18 alone, especially for receding wetting lines and small contact angles. In addition, the values of the parameters obtained from the analyses appeared reasonable. Similar results have been obtained also by other scientists [44],[45]. By combining the molecular kinetic and conventional hydrodynamic models in this way, these authors have helped us to appreciate that the real physics of the moving wetting line is probably more complex than single models would suggest.
Differently from both those approaches, recent studies (usually after the years 2000) focused their efforts in simulating numerically impinging droplets [46],[47], droplets sliding down an inclined wall [48] and capillary tubes behaviour [49],[50].

Liquid - Solid System	V_0 (m/s)	θ_s (°)	λ (nm)	k_w (s^{-1}) $\times 10^6$	k_s (s^{-1}) $\times 10^{11}$	ΔG_w (kJ/mol) ($\Delta G_S + \Delta G_V$)	$\Delta G_S/\Delta G_V$
H_2O – partially wettable surf. (1st test)	0.77	73	1	3	1.3	18.6	0.7
H_2O – partially wettable surf. (2st test)	0.77	73	1.1	1.1	0.5	16.2	1.6
H_2O – partially wettable surf. (1st test)	0.45	73	1.1	1.2	54	27.8	0.6
H_2O – partially wettable surf. (2st test)	0.45	73	1.1	0.87	37	26.9	0.7

Table 2: MKT parameters by Bayer & Megaridis' study of impacting water droplets on partially wettable surfaces [28]

Liquid - Solid System	*We*	θ_m (°)	L_m (m)
H_2O – partially wettable surf. (1st test)	0.3	96	2.27×10^{-12}
H_2O – partially wettable surf. (2st test)	0.16	110	1.61×10^{-11}
H_2O – partially wettable surf. (1st test)	0.90	93	4.73×10^{-13}
H_2O – partially wettable surf. (2st test)	1.80	101	1.65×10^{-15}

Table 3: HDT parameters by Bayer & Megaridis' study of impacting water droplets on partially wettable surfaces [28]

Liquid - Solid System	μ (Pa s)	γ (mN m^{-1})	θ_s (°)	λ (nm)	k_w (s^{-1})	*Ref.*
H_2O - Polyethylene terephthalate tape (PET)	0.001	72.4	82	1.1	2.5×10^5	[32]
H_2O - PET – high velocity	0.001	72.4	82	0.36	8.6×10^9	[32]
16% glycerol/ H_2O - PET	0.0015	69.7	72.5	2.1	6.2×10^2	[29]
86% glycerol/H_2O - Polyethylene coated paper	0.104	65.8	88	0.67	6.3×10^6	[29]
H_2O - PET	0.001	72.4	82	1	2.7×10^5	[32]
H_2O - PET	0.001	72.4	82	1	2.0×10^5	[31]
H_2O - PET	0.001	72.4	82	0.99	9.2×10^6	[33]

Table 4: MKT parameters by different advancing contact angle studies

Liquid - Solid System	μ (Pa s)	γ (mN m^{-1})	θ_s (°)	θ_m (°)	$ln(L/L_m)$	*Ref.*
16% glycerol/water on PET	0.0015	69.7	72.5	84	97	[29]
86% glycerol/H_2O - Polyethylene coated paper	0.104	65.8	88	91	11.3	[29]

Table 5: HDT parameters by advancing contact angle studies

Part II: Experimental activity

3 Experimental Apparatus, Operating Procedures and Test Matrix

Dynamic contact angles have been studied by analysing growth and decrease of liquid droplets on selected surfaces. The apparatus consists of a test sample, with the test surface, which is connected to a glass syringe activated by a syringe pump. A digital camera equipped with a telecentric lens is used for the acquisition droplet images. To achieve the desired light contrast, a led light is used to light the drop up from the back.

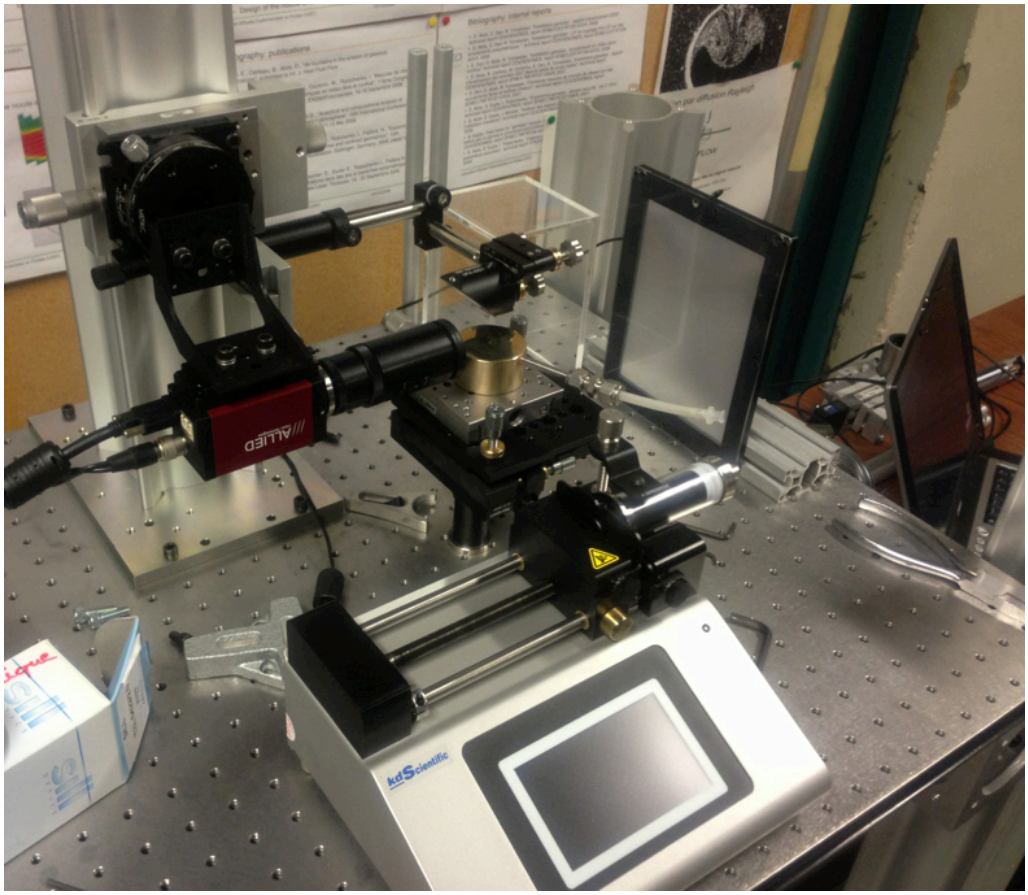

Figure 12: Experimental apparatus

Test sample

Different test samples have been adopted, made out of different materials (plexiglas, aluminium, copper, brass, stainless steel, see Fig. 9) and with different surface roughness (only for stainless steel, see Fig. 10) of the test surface. A hole (0.5 mm of diameter) is drilled on the test surface (top of the cylinder), through which injection or suction of deionized (DI) water is realized. DI water is supplied by a stainless steel pipe connected to the lateral surface of the test sample.
To obtain mirror polished surfaces, the test surface has been polished manually with small grain papers and diamond paste with a grain size of 3 microns. The roughness R_a (arithmetic average of the absolute values of the vertical distances from the mean line to the data points) obtained by this process is around 0.01 μm.

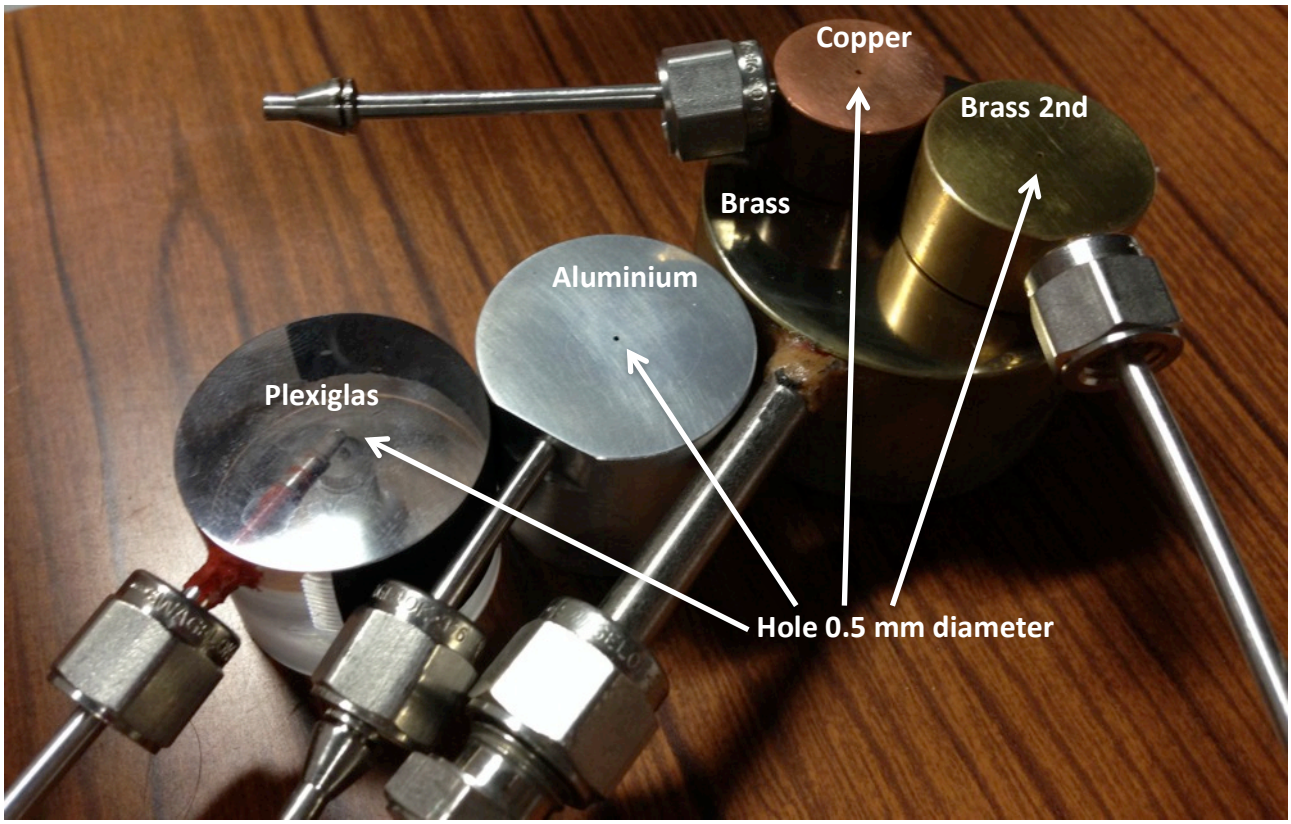

Figure 13: Test samples made out of different materials

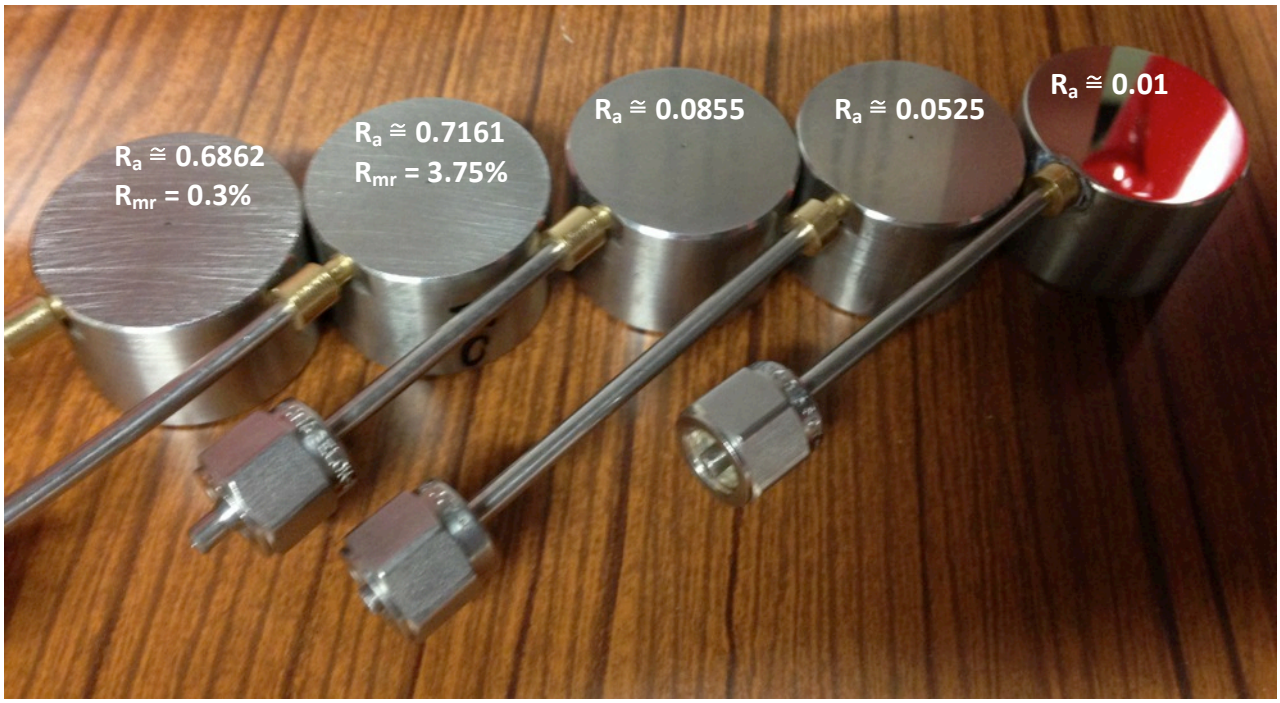

Figure 14: Stainless steel samples with different roughness

Injection system

A two-way syringe pump is used to inject and suction DI water. The syringe used is a SGE1 glass syringe with a volume of 25 mL, an outer diameter of 27 mm. The pump is a KD Scientific Legato 1102. It can deliver constant volumetric flow rate spacing from an order of magnitude of pL/min up to mL/min with a calculated accuracy of ±30%. We will verify this value later (Part III, Section 1).
To minimize compressibility issues, the syringe is connected to the stainless steel pipe of the test sample by a hard Plexiglas tube 3 mm in the external diameter.

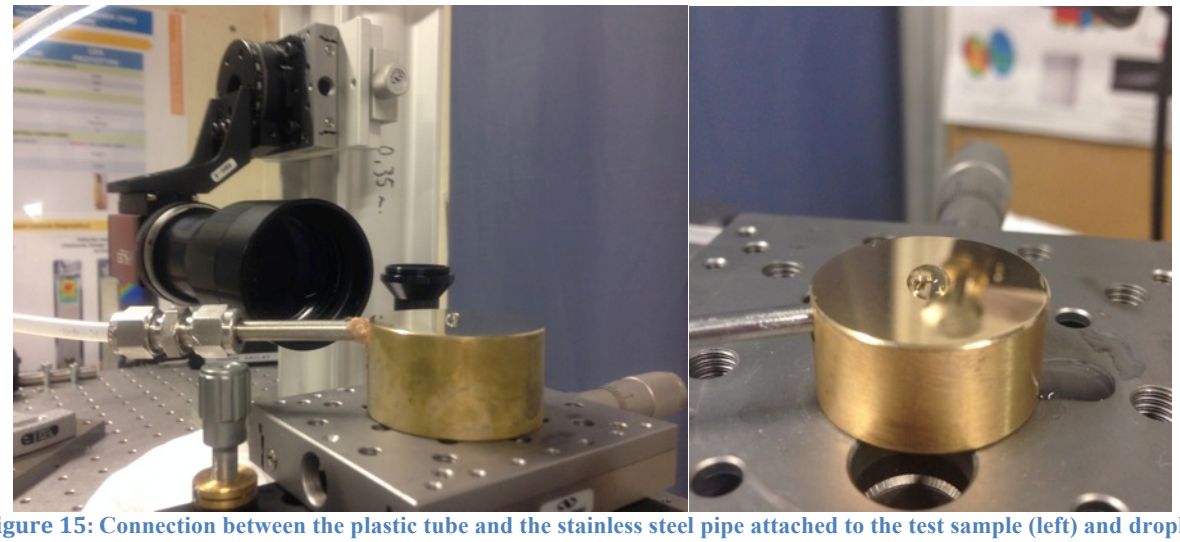

Figure 15: Connection between the plastic tube and the stainless steel pipe attached to the test sample (left) and droplet growing on a copper mirror-polished surface (right)

Camera and light

The digital camera used for image acquisition is a PIKE F-421B with a resolution of 2048x2048 pixels, equipped with telecentric lens. It is a mounted on micrometric translation and rotation stages in order to regulate the focal distance and the focal plane and is connected to the PC trough Ethernet connection. The maximum frame rate achieved by the camera is 15.58 frames per second. A spatial resolution of 340 pixel/mm was usually adopted.

Operating procedure

At the beginning of each experiment the test surface is levelled with the gravity plane and cleaned with ethanol and dried air. After this "dry-cleaning", a "wet cleaning" is performed with the same fluid of the injection (DI water). The "wet cleaning" is also necessary for repeatability purpose, since metallic surfaces abnormally behaved as hydrophobic surfaces during the first wetting, as also observed by Bayer and Megaridis [28].
Tests are thus realized by injecting (for advancing contact angles) and sucking (for receding contact angles) DI water. A triple line is thus realized at the air/water/solid interface. Water and air properties at ambient conditions are reported in Table 6.

	Surface Tension [N/m]	Density [kg/m^3]	Dynamic Viscosity [Pa s]
DI Water	0.0718	997	1.002×10^{-3}
Air		1.18	18.6×10^{-6}

Table 6: Fluid properties at the operating conditions

Different initial conditions have been investigated for our injection transients: from initial volume of 0 mm^3 and from a static drop of finite volume. It will be shown later that this will lead to different contact angle behaviours.

Test Matrix

The test matrix is reported in
Table 7. Five different mirror-polished surfaces have been investigated (in green): aluminium, brass, copper, plexiglas and stainless steel. All the tests have been realized with a resolution of 150 mm/pixel. Brass was investigated with two different optical setups (150 and 340 mm/pixel). Surface roughness effects were investigated on stainless steel surfaces (in red). These tests are labelled with the grain size of the paper used to polish the surface. Further details on the characterization of these surfaces can be found in appendix. Different volumetric flow rates have been realized (in blue). To check the repeatability of the measurement, each experimental condition has been repeated several times, as reported in
Table 7.

Test Matrix												
		Q nom (ml/min)										
	# of tests	-0.005	-0.01	-0.05	-0.1	-0.5	0.005	0.05	0.1	0.5	1	2
Material	Aluminum*	12	2	4	/	/	5	6	3	3	3	/
	Brass*	/	/	16	15	12	5	5	5	/	5	5
	Brass 2nd*	10	9	8	/	/	8	5	6	/	/	/
	Copper*	11	9	5	/	/	5	5	5	/	5	/
	Plexiglass	10	13	1	/	/	4	8	3	/	/	/
	Stainless Steel**	31	28	21	/	/	28	27	28	27	/	/
Roughness	SS*	8	7	5	/	/	7	5	6	5	/	/
	SS - P40	6	5	4	/	/	6	5	5	5	/	/
	SS - P80	7	5	5	/	/	5	7	6	6	/	/
	SS - P180 (Ra = 0.855 µm)	5	5	4	/	/	5	5	6	5	/	/
	SS - P320 (Ra = 0.525 µm)	5	6	3	/	/	5	5	5	6	/	/

150 mm/pixel

340 mm/pixel

Table 7: Test matrix

* = roughness ≤ 0.01 µm (mirror polishing)

** = sum of al Stainless Steel tests with different roughness (reported above one by one)

Part III: Analysis of experimental results

4 Post-processing techniques

This section describes how, from raw images recorded by the camera, we obtain relevant quantities, such as:

- curvature radius at top of the droplet and at every point of the interface;
- wet diameter;
- contact angle;
- height;
- volume;
- droplet profile.

In this aim, two different MATLAB codes have been used (detailed in appendices):

- a code based solely on geometrical considerations, developed at DESTEC Department in Pisa University;
- a more physical code, developed by Konduru [53] and also used by Fighera [54].

Two important requirements for the recorded images are: focus and high resolution.
Resolution, or scale factor, is the relation between the sensor size (in pixels) and the target size (in millimetres). The usual scale factor achieved in this study is about 340 pixel/mm (see Figure 16). High resolution refers to a high scale factor. As a matter of fact, there is a compromise between the length scale of the phenomenon that we are investigating and the accuracy that we want to achieve with the image processing.

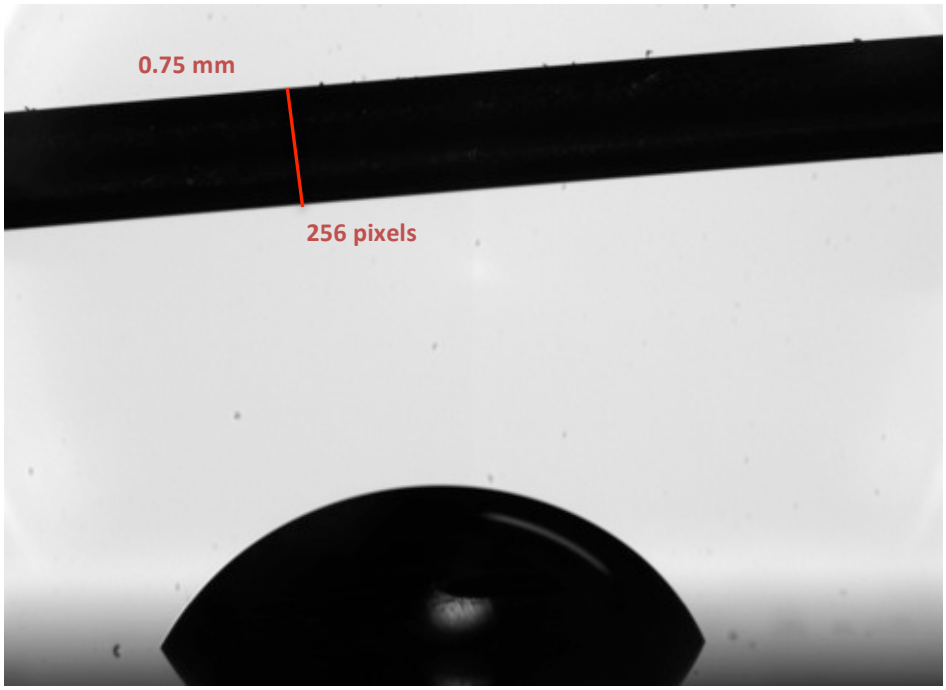

Figure 16: Determination of the pixel size

Focus means “how” sharp is the gradient of the colour at the interface. As a matter of fact, there is always light diffusion at the interface between the drop (almost black) and the background (almost white), leading to a less sharp definition of the droplet shape (see Figure 17).

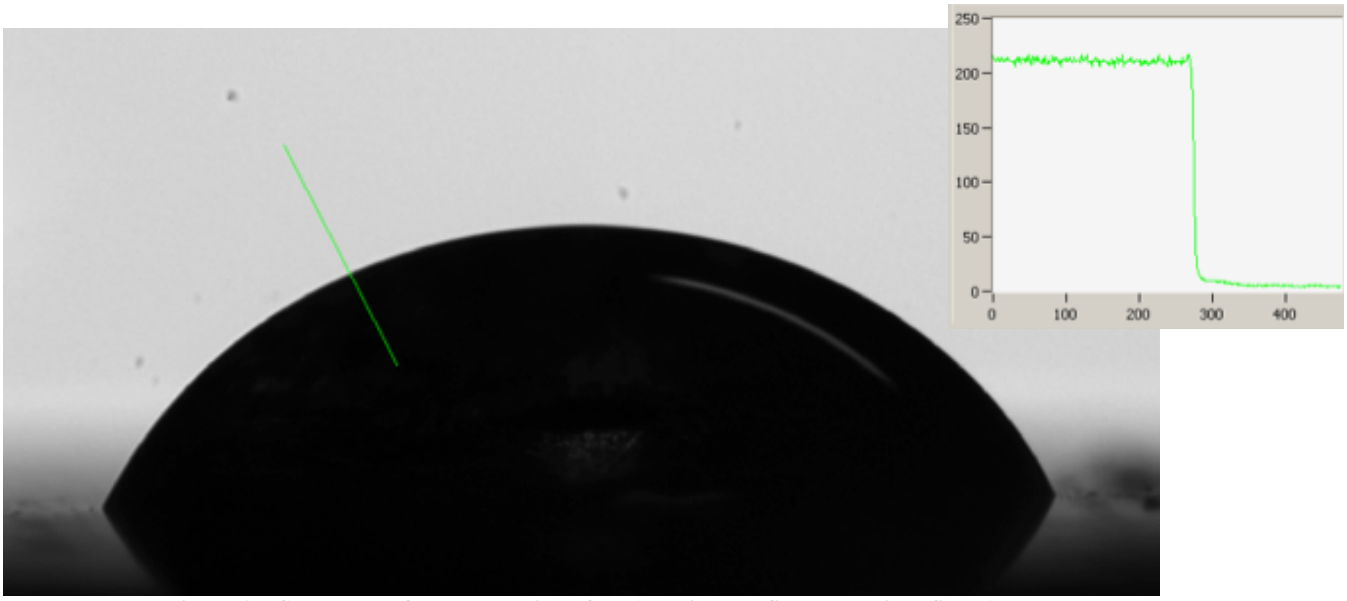

Figure 17: Sharpness of the droplet interface (cut view profile on the right figure)

Common features of the post-processing codes

The first steps of the post-processing techniques are essentially the same for both codes. As a first step, the raw image of the drop (see Figure 18) is subtracted from the background and bad pixels are fixed (see Figure 19).

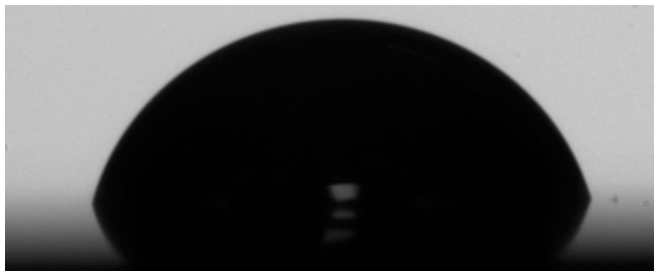

Figure 18: Initial image

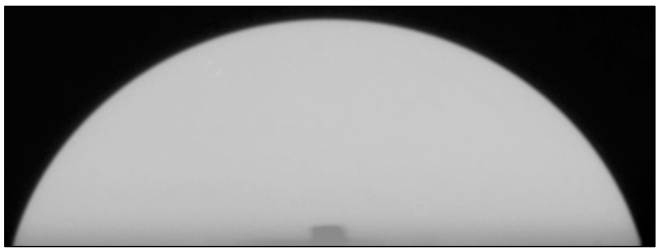

Figure 19: Initial image subtracted to background

Then, the image is converted into grey-scale (see Figure 20) and then into black and white (see Figure 21). The conversion into black and white is achieved with the use of a threshold. This threshold is a normalized intensity and lies in the range [0,1]. This range is relative to the signal levels possible for the image class. Its influence is less important if the image is clearly in focus and the interface can be well distinguished (the gradient of colour at the interface is sharp).

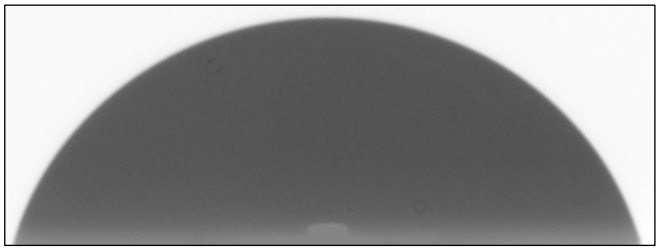

Figure 20: Image converted to gray-scale

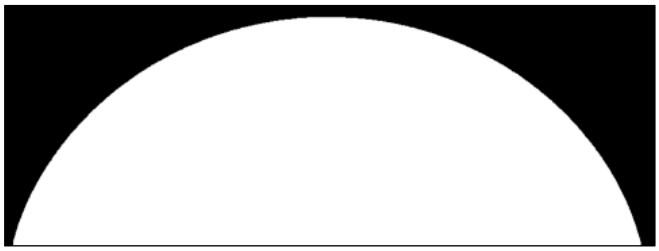

Figure 21: Image after the application of the threshold filter

The Canny method is then used to find edges by seeking local maxima of the gradient of the image. Thus, if the image is just black and white, it will detect the interface created by the threshold filter (see Figure 22). The image is then converted from pixels to millimeters trough the scale factor (see Figure 23).

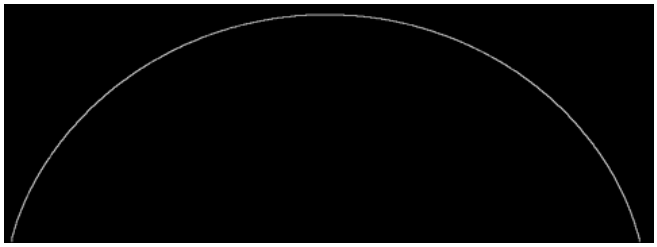

Figure 22: Droplet interface detected by the Canny method

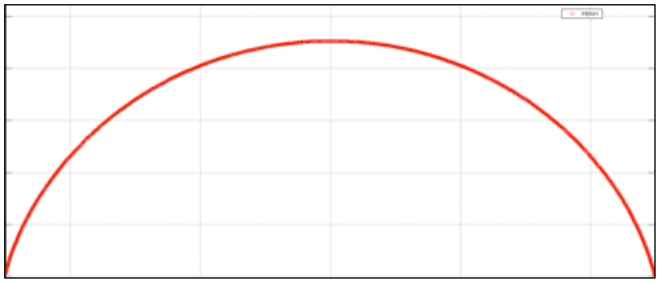

Figure 23: Droplet profile in millimetres

The Geometrical Code by DESTEC

The DESTEC code is able to identify the perimeter of the droplet in a matrix used by the routine *regionprops* of the MATLAB's Image Processing Toolbox (IPT) to extract the relevant quantities of the droplet. Some quantities are straightforward once the droplet profile is known (droplet height, wet diameter), some other quantities require specific developments.
In particular, the droplet volume has been evaluated by the *Papp-Guldin Theorem*: the volume of a solid of revolution Ω obtained by rotating by an angle $\phi \in [0{:}2\pi]$, around the axis z, a plane area dA is

$$V = \phi \cdot r \cdot dA \tag{24}$$

Where r is the radial coordinate of the barycentre of the Area dA. This relation has been applied to every pixel of the drop, considered as an axisymmetric body.

For what concerns the contact angle, a least square regression with a parabolic function on drop lower points close to the triple line has been used (see Figure 24)

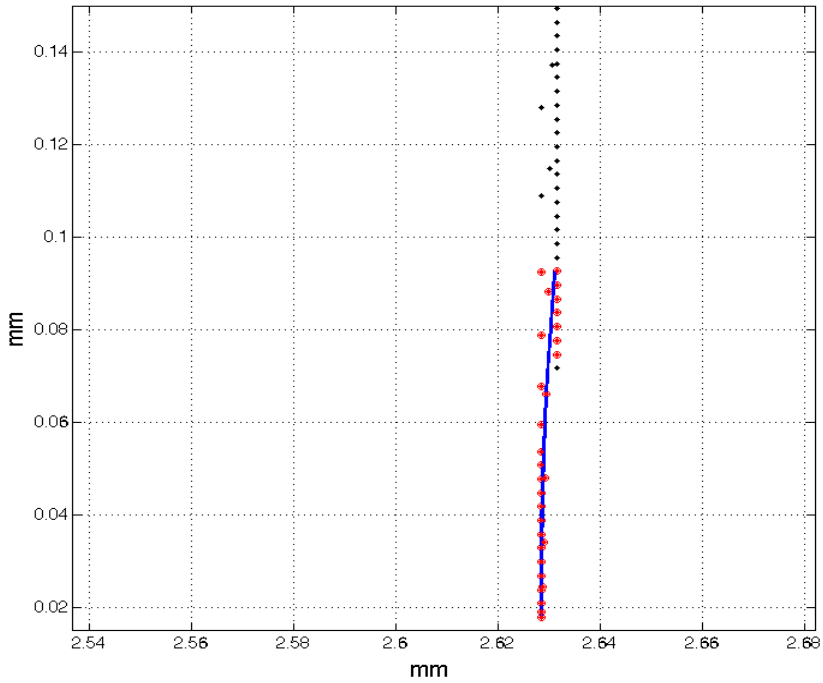

Figure 24: Profile of the drop in black (red points are the points used for regression process and blue curve is the regression curve used in the estimation of contact angle)

A similar approach has been used to evaluate the local curvature: for every point of the interface, the 5 leftmost and the 5 rightmost points before have been used to find the interpolating 2nd order polynomial (see Figure 25) and obtain the two principal curvatures of the drop profile $y(r)$ by classical mathematical formulae for a solid of revolution [55]:

$$K_1 = -\frac{{}^{d^2y}/_{dr^2}}{\left[1 + \left({}^{dy}/_{dr}\right)^2\right]^{3/2}} \tag{25}$$

$$K_2 = \frac{\sin\left[\tan^{-1}\left({}^{dy}/_{dr}\right)\right]}{y} \tag{26}$$

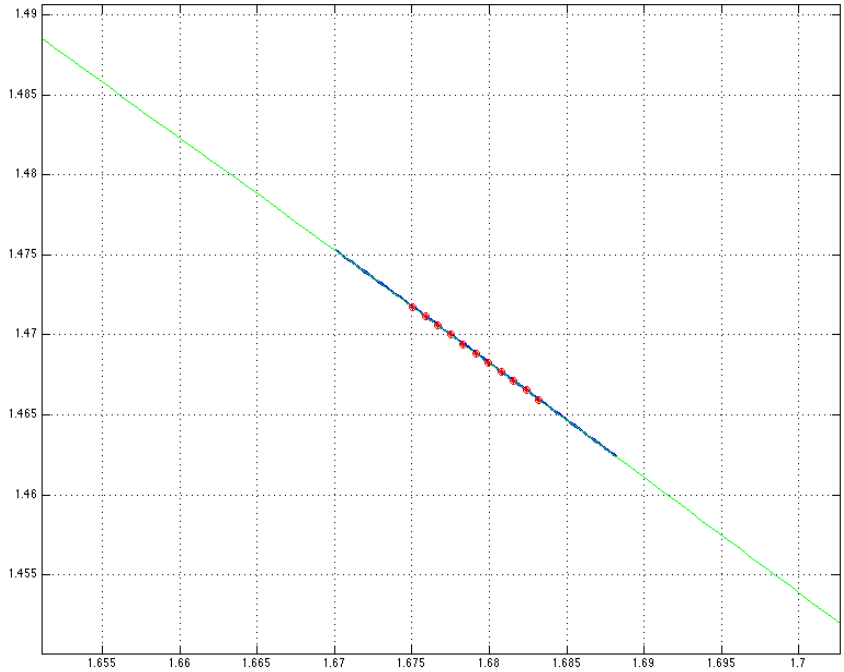

Figure 25: Profile of the drop in green line (red points are the points used for regression process and blue curve is the regression curve used in the evaluation of curvature). Measures in mm.

Konduru's code

The most well established methodology is the Axisymmetric Drop Shape Analysis Profile (ADSAP) developed by Neumann et al. ([56], [57]). This methodology addresses static conditions and uses a Laplace-Young fitting of the droplet profile instead of polynomial fittings. It consists of an iterative procedure to find the best fit between the experimental drop profile, described by a finite number of points, and the numerical solution for an axisymmetric profile derived by the Young-Laplace Equation:

$$p_f - p_g = 2\,\gamma\,K \tag{27}$$

Which, applying the Stevino's law becomes:

$$\left(\rho_f - \rho_g\right) g\, y + 2\,\gamma/R_0 = \gamma\,\left(\frac{1}{R_1} + \frac{1}{R_2}\right) \tag{28}$$

Substituting the two curvature radii:

$$\frac{1}{R_1} = \frac{d\vartheta}{ds} \tag{29}$$

$$\frac{1}{R_2} = \frac{\sin\vartheta}{r} \tag{30}$$

We obtain:

$$\frac{dr}{ds} = \cos\vartheta \tag{31}$$

$$\frac{dy}{ds} = \sin\vartheta \tag{32}$$

$$\frac{d\vartheta}{ds} = \frac{2}{R_0} + \frac{\Delta\rho g y}{\gamma} - \frac{\sin\vartheta}{r} \tag{33}$$

The Equation above is a second order differential equation, which can be solved numerically by optimization of two parameters: the curvature radius at drop top R_0 and the capillary length c through changes in surface tension γ:

$$c = \frac{\gamma}{\Delta\rho\, g} \tag{34}$$

The function to minimize is the sum of the square distances between the experimental profile (20 points) and the Laplace Young equation.
The contact angle is an output of this optimization process, since the code founds the slope of the profile at every point of the interface, triple line included.
Therefore, a very accurate evaluation of the contact angle is expected.

For what concerns the volume calculation, Konduru's code is slightly different from DESTEC code, but their results are very close one each other. Thus they validate each other.

What has to be noticed is that the nominal flow rates has an error of the order of 30%, as can be assessed in the Figure 26.

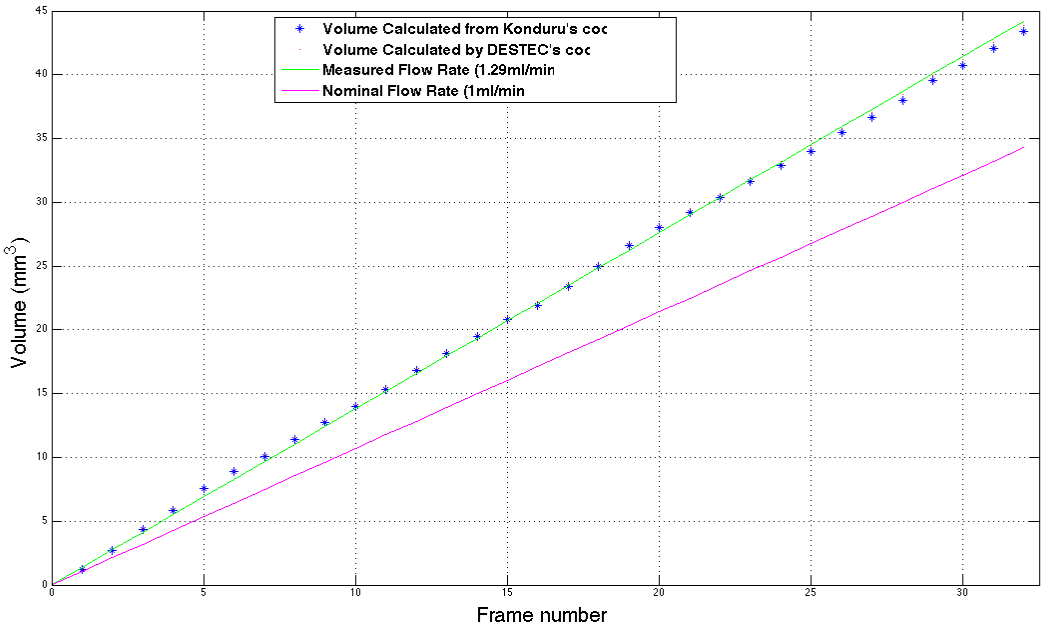

Figure 26: Volume comparison; result of the method adopted by DESTEC's code, result of the method adopted by Konduru and flow rates (nominal and calculated)

5 Momentum balance and dynamics of a spreading droplet

In this section the dynamic of a liquid drop is studied. Consider a drop sitting on a flat solid surface, as shown in Figure 27.

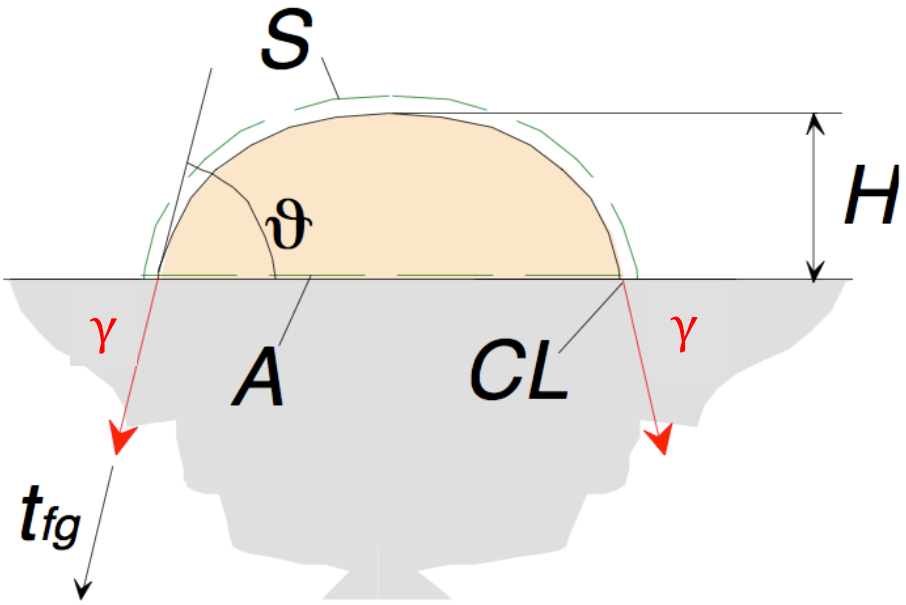

Figure 27: Control volume for the momentum balance

As shown by Cattide et al. [58] for bubbles, the momentum balance for a droplet reads:

$$\frac{d}{dt}\int_V \rho_f \mathbf{v} dV = \int_V \rho_f \mathbf{g} dV + \int_S \left(\underline{\underline{\mathbf{T}}}_{v,g} - p_g \underline{\underline{\mathbf{I}}} + \rho_g \mathbf{v}_g(\mathbf{v}_g - \mathbf{v}_s)\right)\cdot \mathbf{n}\, ds + \int_A \left(\underline{\underline{\mathbf{T}}}_{v,f} - p_f \underline{\underline{\mathbf{I}}} + \rho_f \mathbf{v}_f(\mathbf{v}_f - \mathbf{v}_s)\right)\cdot \mathbf{n}\, ds + \int_{CL} \gamma_{fg}\, \mathbf{t}_{fg}\, dL \tag{35}$$

where the different terms are: variation of momentum, volumetric force acting in the volume (only gravity in our case), viscous stress and mass transfer (evaporation or condensation) integrated all over the drop interface and all over the contact area, and surface tension forces on the contact line.
If evaporation of liquid and gas absorption are neglected, since the injection flow rate is constant, the drop volume grows linearly with time. Furthermore, if the variation of temperature and pressure are also negligible, the mass of the drop will also grow linearly with time.
The balance for a drop of liquid, in quasi-static growing, can be therefore conveniently simplified as

$$\int_{CL} \gamma_{fg}\, \mathbf{t}_{fg}\, dL + \int_V \rho_f \mathbf{g} dV - \int_S p_g \underline{\underline{\mathbf{I}}}\cdot \mathbf{n}\, ds - \int_A p_f \underline{\underline{\mathbf{I}}}\cdot \mathbf{n}\, ds = 0 \tag{36}$$

That in the vertical direction becomes

$$F_p + F_\gamma + F_b = 0 \tag{37}$$

Where

$$F_p = \frac{\pi D_b^2}{4}\left(\frac{2\gamma}{R_0} + \rho_f g H - \rho_g g H\right) \tag{38}$$

$$F_\sigma = -\pi D_b \gamma \sin\theta \tag{39}$$

$$F_b = Vg\left(\rho_g - \rho_f\right) \tag{40}$$

This force balance has been verified experimentally for bubbles by Di Marco and Saccone [[59],[60]), but since passages from Eq. 35 to Eq. 37 involved the Laplace-Young equation that is generally valid for low Bond Number, bigger drops will not follow this momentum balance.
Momentum balance (Eq. 37) is applied to different injection flow rate, as shown in Figure 28 through
Figure 31.

Solid lines are obtained by numerical integration of Eq.31, 32 and 33, as proposed by Pitts [62]. Dots represent experimental data and are obtained by calculating the terms expressed by Eq. 38, 39 and 40, using measured quantities. In both cases, two boundary conditions have to be set: the first one is the curvature radius at drop top, which varies cyclically; the second one is the contact angle. For contact angle in particular, two approaches can be adopted: to put in the numerical resolution the static contact angle (measured on a sessile droplet), or to use the dynamic contact angle obtained from the images of spreading droplet.
Both options have been evaluated, but we think that the second one is more interesting: with this second approach we are using the Laplace-Young equation to determine the shape of the drop, including the effect of overpressure induced buy the flow field.
This MATLAB routine has been created with the intent to predict bubble shapes and profiles by Di Marco, Forgione and Grassi [61], and has been modified in the present study to predict droplet shapes and profiles.

The proposed momentum balances show that, whatever is the injection flow rate tested, the droplet evolution seems to be quasi-static. As it can clearly be seen, the overall balance (Eq. 37) is satisfied with a small discrepancy, usually below 5%. An exception is experienced during the latest stage of droplet grow for high flow rates, since the Bond number might become too large for the Laplace-Young equation to be appropriate.

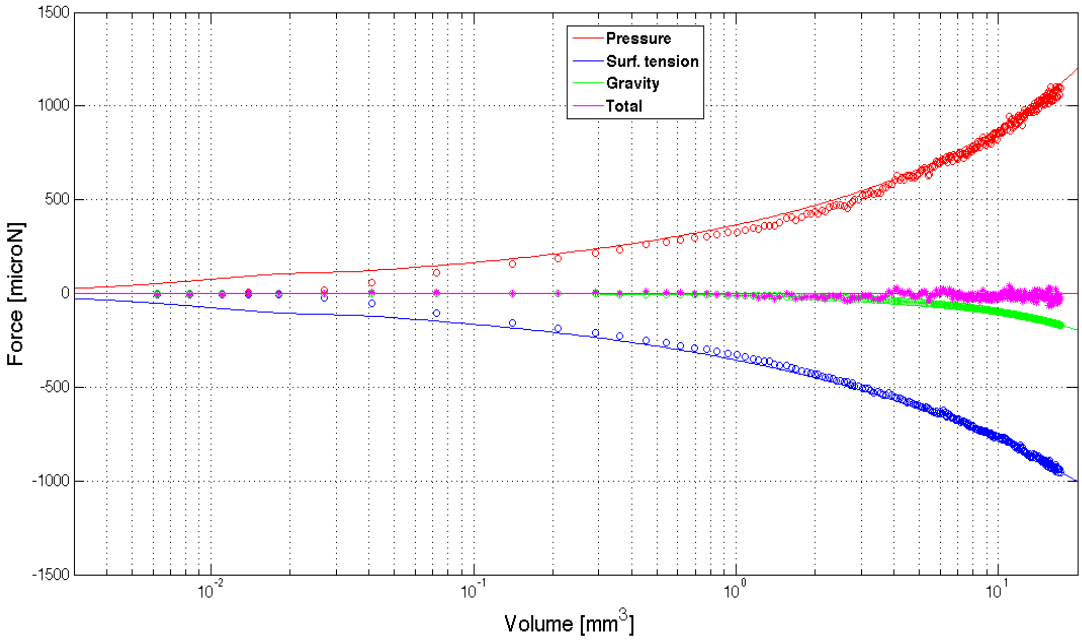

Figure 28: Force balance for Q=0.005 ml/min

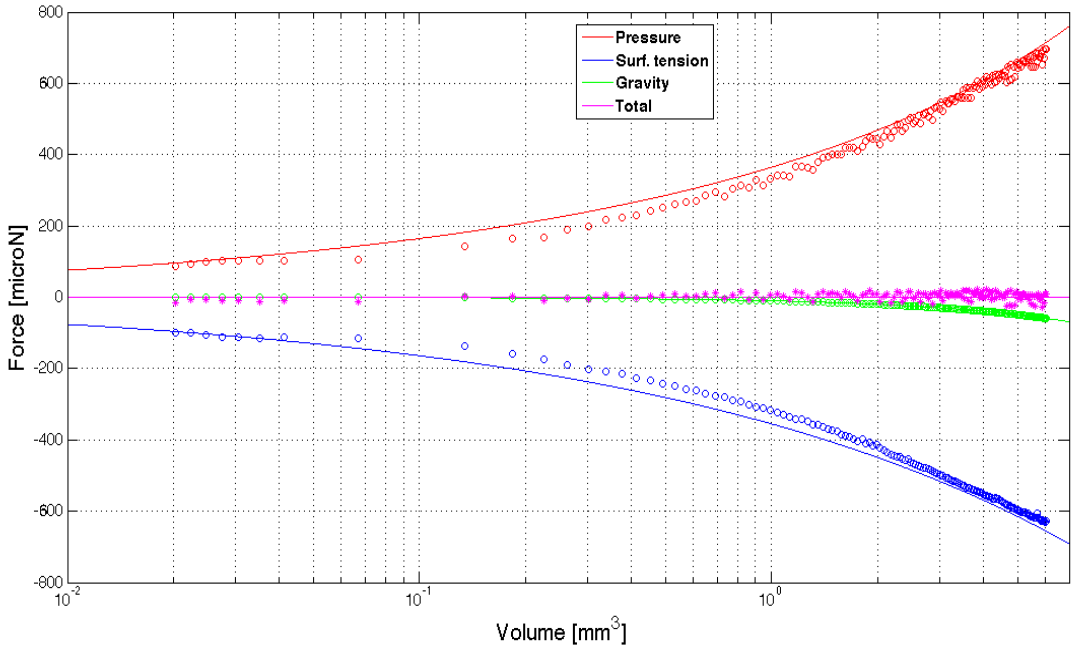

Figure 29: Force balance for Q=0.05 ml/min

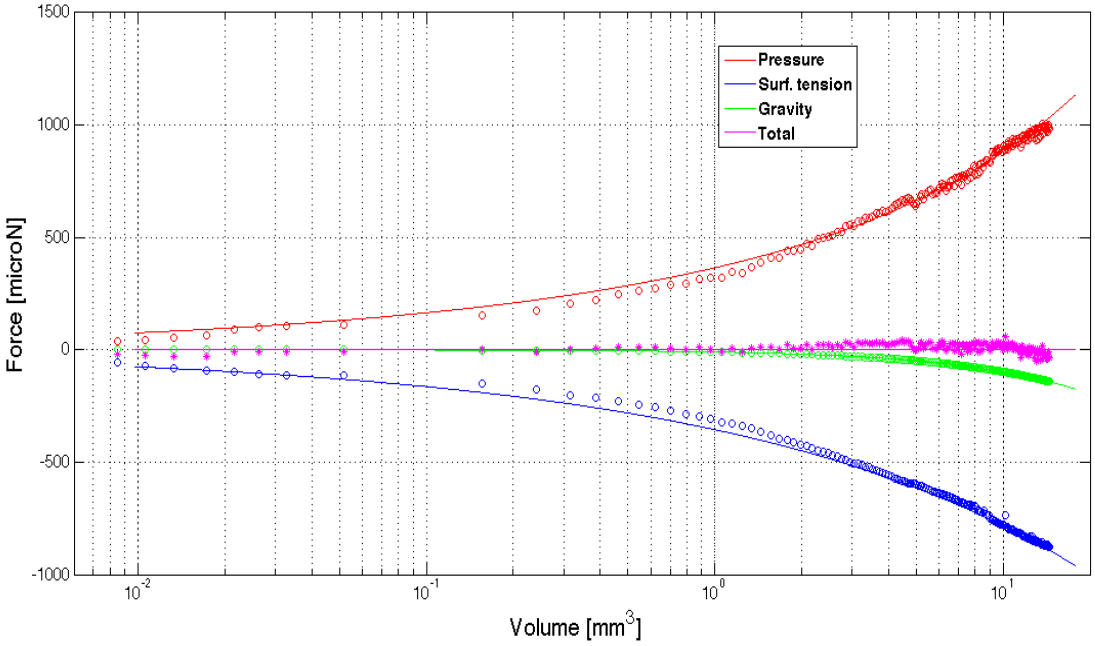

Figure 30: Force balance for Q = 0.1 ml/min

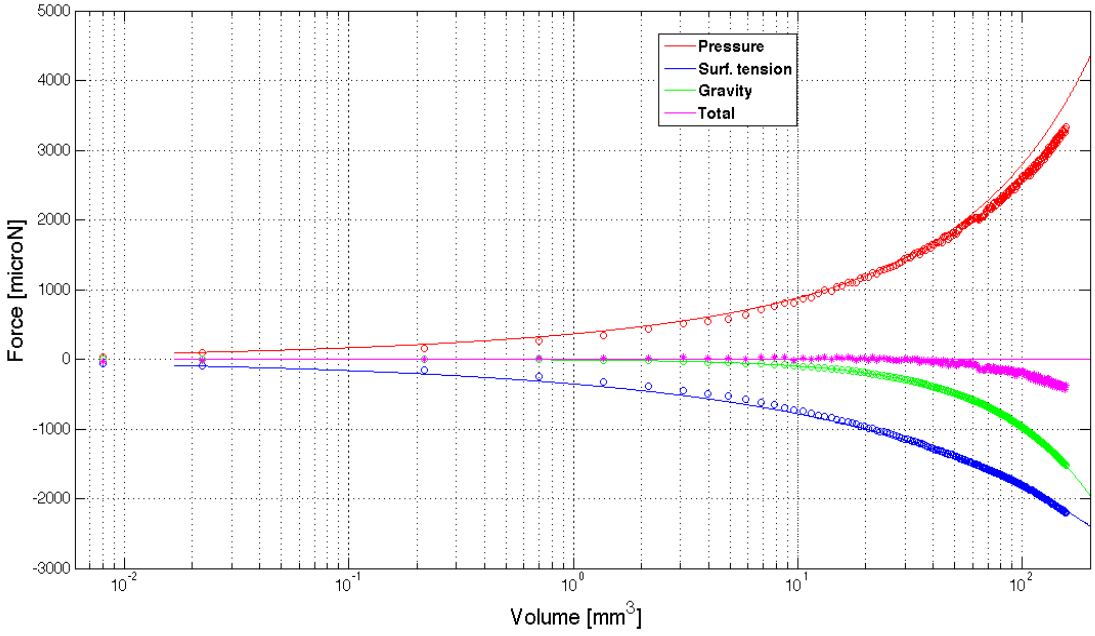

Figure 31: Force balance for Q=1 ml/min

Our choice to plot the balance with the dynamic contact angle instead of the static contact angle (a sample comparison is shown in Figure 32) is also due to the difficulty of catching the static contact angle, since hysteresis gave us a quite wide range of choice, as can be seen in Figure 33, where static contact angles for sessile droplets correspond to the first frame.

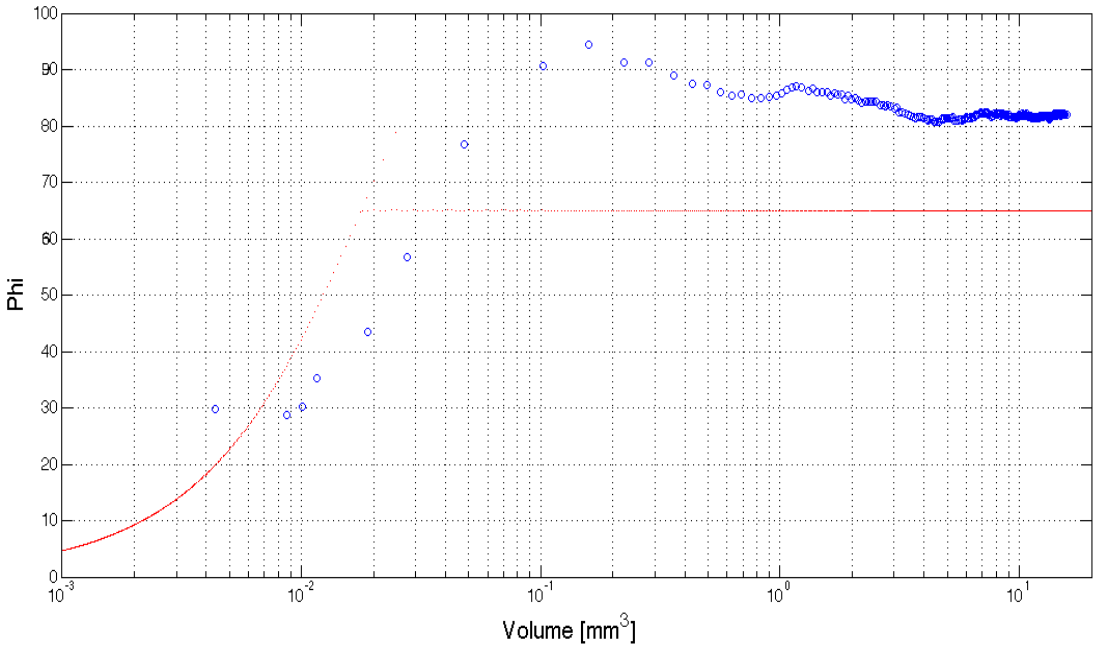

Figure 32: Contact angle vs. droplet volume for Q=0.005 ml/min.
Red line is the static contact angle. Blue spots are dynamic angles measured.

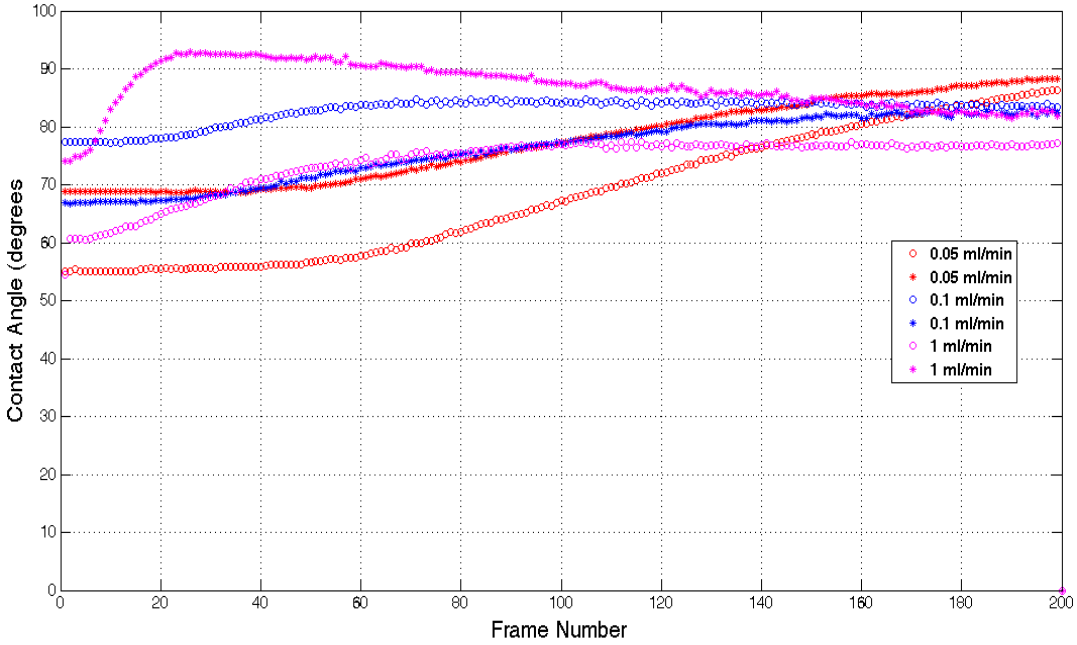

Figure 33: Evolution of the contact angle for different flow rates, starting from a sessile droplet

So, with respect to the static equilibrium condition of sessile droplets (obtained by computing the static contact angle as the second boundary condition in the numerical solution) a new equilibrium is achieved (Momentum Balance is still satisfied), with a different droplet shape. A comparison between spreading and sessile droplets is shown in Figure 35 through Figure 37. The solid line represents the theoretical value for sessile droplet (a static contact angle of 65° is assumed), whereas blue dots are experimental values for spreading droplets.

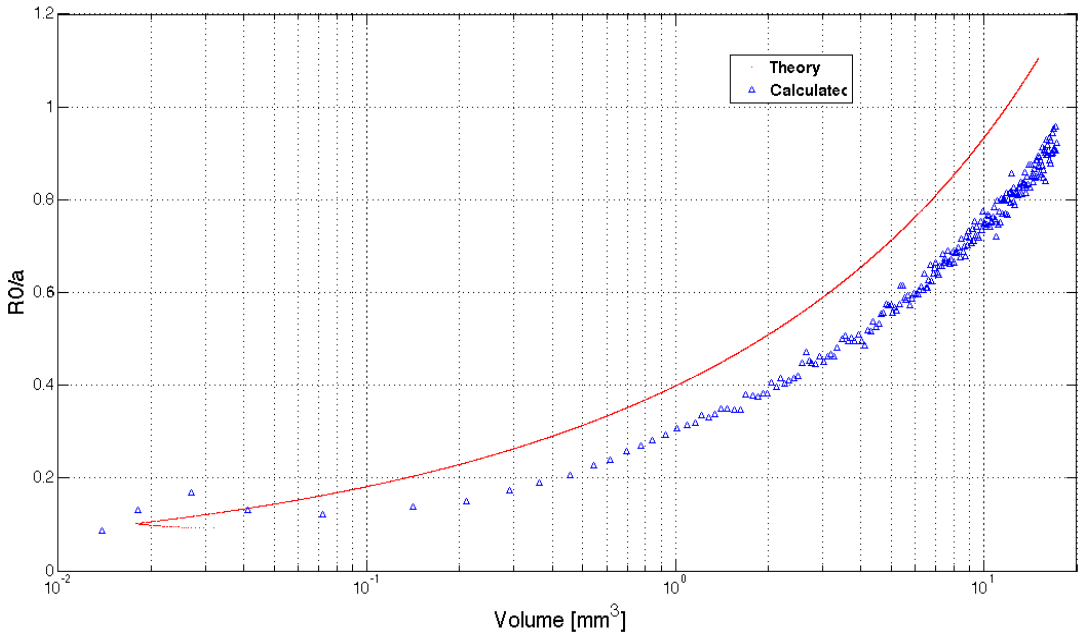

Figure 34: Non-dimensional curvature radius at the top of the droplet (Q=0.005 ml/min)

As shown in Figure 34, the curvature radius is usually lower than the theoretical one for a sessile droplet of the same volume. Moreover, spreading droplets are usually higher than sessile droplets with the same volume (see Figure 35). Both effects tend to make the pressure appearing in the term F_p (Eq.38) to increase. However, the wet radius is smaller (see Figure 36) and this effect prevails, making the pressure force to decrease, as shown in Figure 37. *In summa*, with an imposed flow rate, we expect an enhancement of pressure inside the droplet, but a decrease of pressure force F_p, because of the reduction of the wet area. The same reasoning applies to surface tension forces: the contact angle is closer to 90° than for the sessile droplet, and thus its sine is closer to 1, but the decrease of the wet diameter prevails, and the surface tension force decreases.

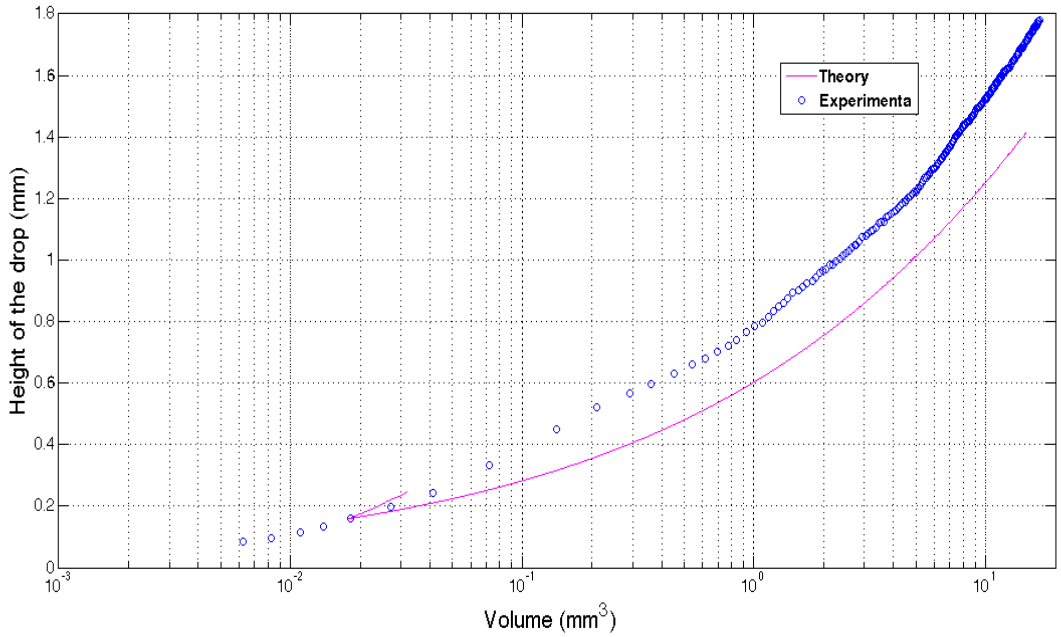

Figure 35: Height of the droplet (Q=0.005 ml/min)

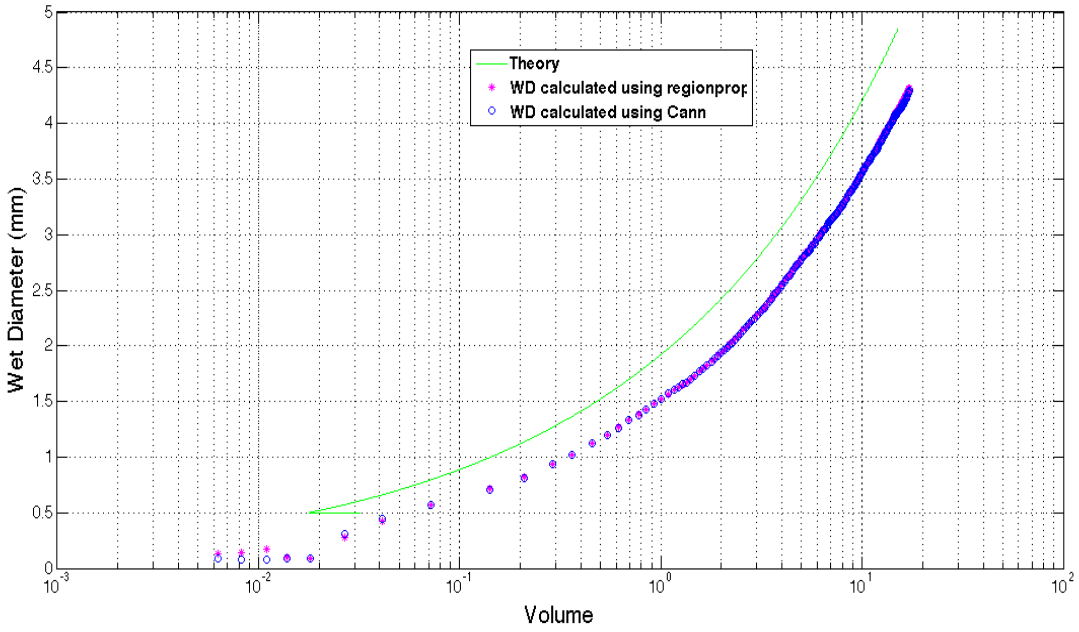

Figure 36: Wet diameter of the droplet (Q=0.005 ml/min)

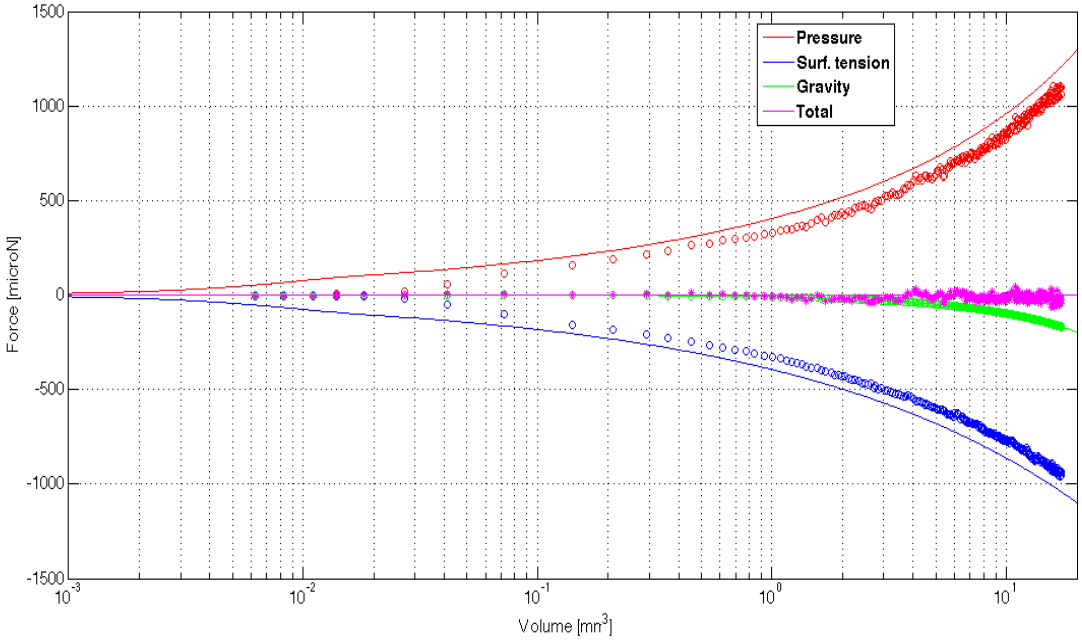

Figure 37: Force balance for Q=0.005 ml/min (static contact angle 65°)

This reasoning is also confirmed by the behaviour of curvature radius at the apex, height and diameter as a function of the flow rate. As expected, the curvature at the apex and the wet diameter decrease with increasing flow rates, whereas the droplet height increases (see Figure 38 through Figure 42). For a given volume, although static momentum balances might be satisfied, the flow rate still influences the behaviour of triple line and the contact angle itself, since it determines the shape of the spreading droplet (see Figure 42).

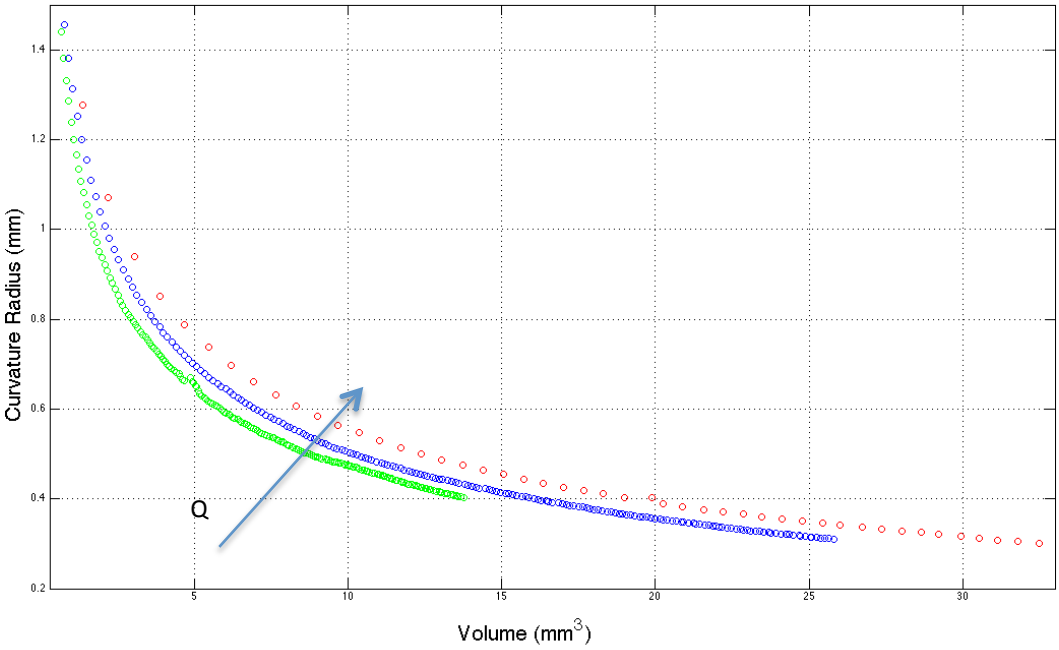

Figure 38: Curvature at the droplet apex for different flow rates

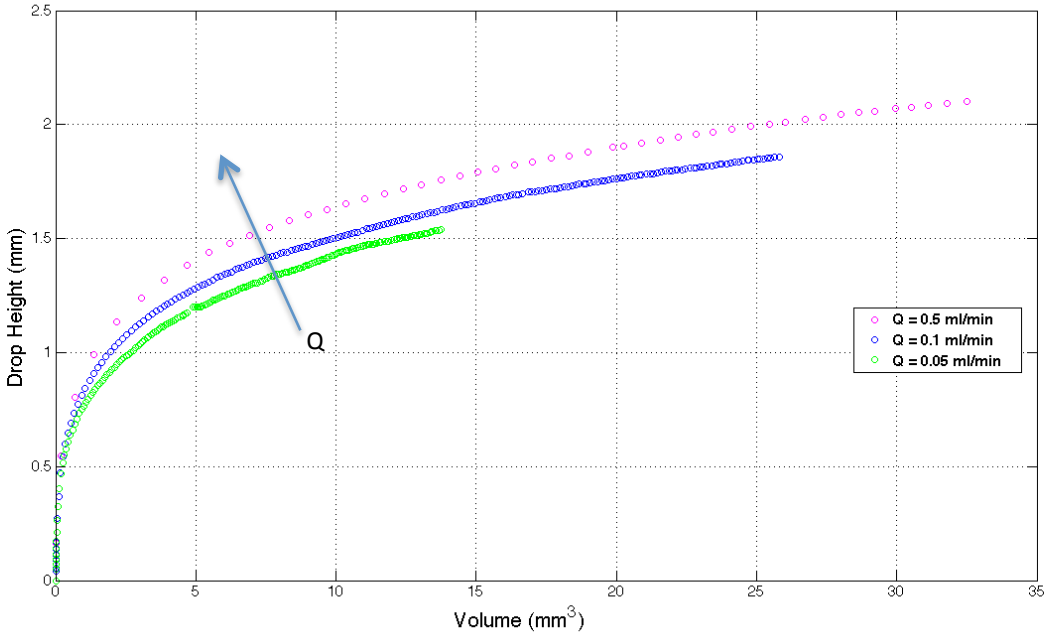

Figure 39: Droplet height for different flow rates

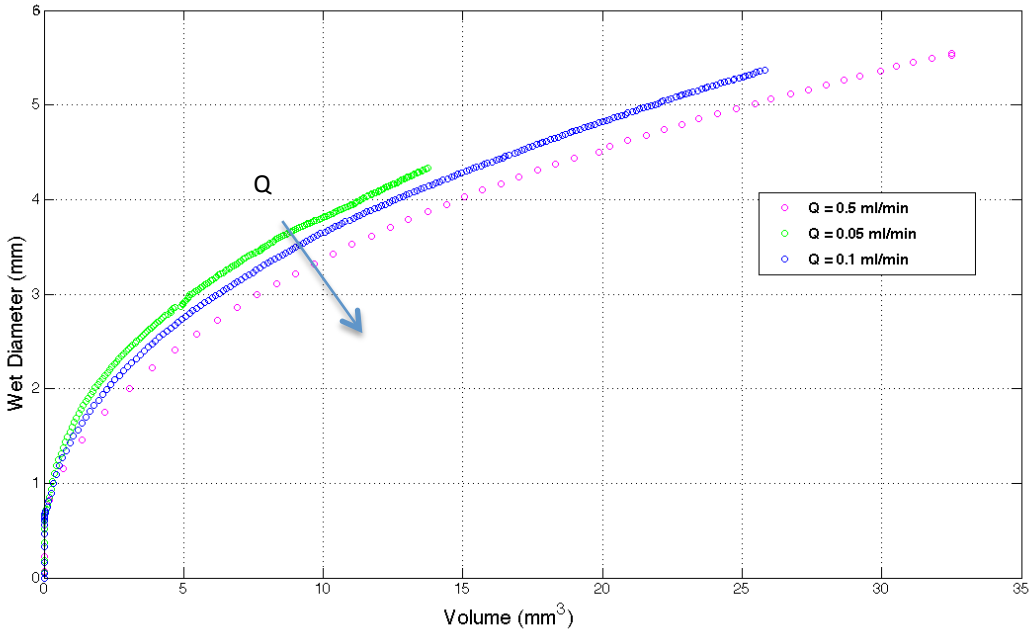

Figure 40: Droplet wet diameter for different flow rates

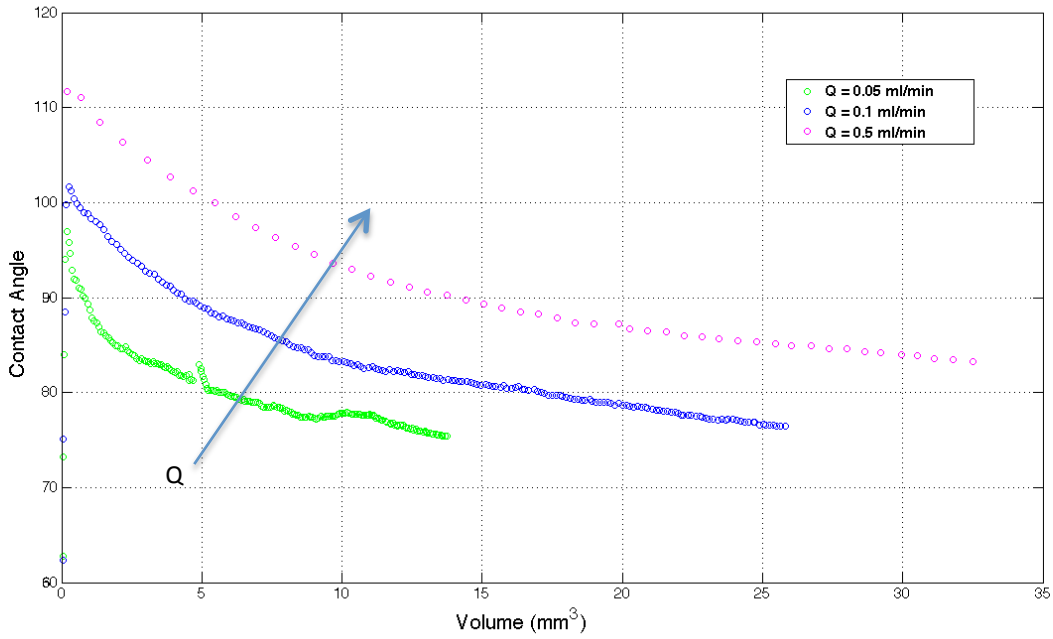

Figure 41: Droplet contact angle for different flow rates

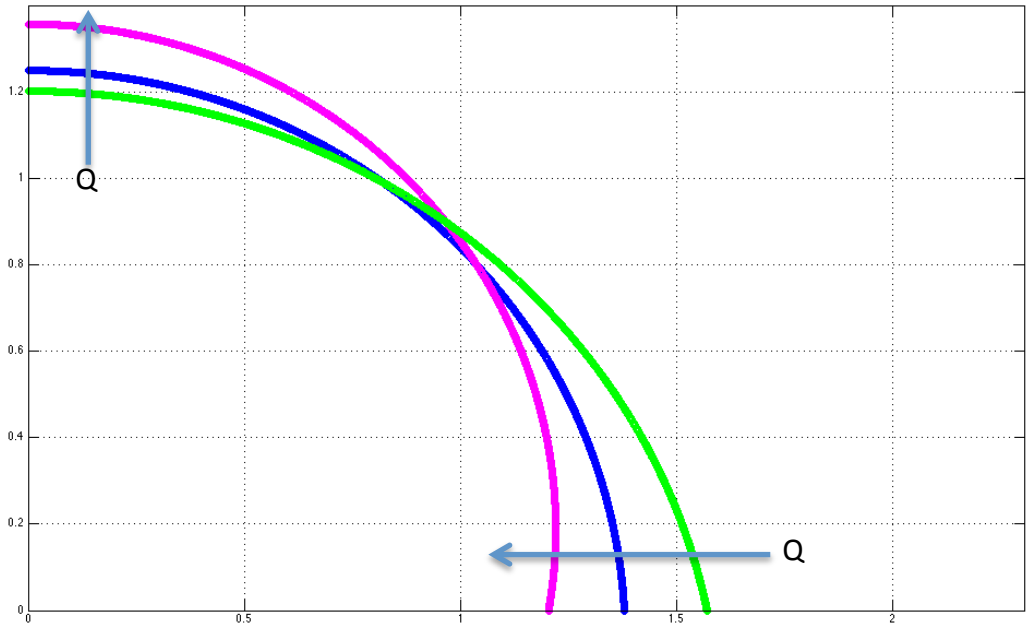

Figure 42: Profiles of droplets with the same volume and different injection flow rates (V=5 mm³, volumes difference ΔV/V<1%)

6 Non-dimensional vertical momentum balance and contact angle verification

To obtain a non-dimensional form of the vertical momentum balance, we have to simplify Eq.35 and integrate it in the vertical direction.

$$\begin{cases} \mathrm{dV}/dt = Q \\ -Va - Qv + \dfrac{\pi D_b^2}{4}\left(\dfrac{2\gamma}{\rho_f R_0} + \dfrac{\Delta\rho}{\rho_f} gH\right) + v_{in}^2 \dfrac{\pi D_{or}^2}{4} - Vg\dfrac{\Delta\rho}{\rho_f} - \dfrac{D_b \pi\gamma}{\rho_f}\sin\theta = 0 \end{cases} \tag{41}$$

We adimensionalised the set of Equations 41 and we get two dimensionless numbers: the Weber number We, the Eötvös number Eo (also known as Bond number). The choice of parameters to obtain the non-dimensional form is essential. We choose the following measured quantities: the wet diameter, D_b, as length scale, and the triple line velocity, V_{CL}, as velocity scale.
It is worth mentioning that different scales have been used e.g. by Gerlach et al. [63] and by Padday [64]. The choice adopted in this paper is due to the fact that both D_b and V_{CL} varies with volume and we are not interested in testing different liquids. Furthermore, we used the velocity and acceleration of the centre of gravity in the first two terms. Making appropriate substitutions:

$$\begin{cases} t = \dfrac{D_b}{v_{CL}} t^* \\ R_0 = D_b R_0^* \\ \dfrac{d}{dt}\circ = \dfrac{v_{CL}}{D_b}\dfrac{d}{dt^*}\circ \\ v = v_{CL} v^* \\ Q = v_{in} A_{or} = v_{CL} v_{in}^* A_{or}^* {D_b}^2 \\ a = \dfrac{{v_{CL}}^2}{D_b} a^* \end{cases} \tag{42}$$

We get

$$-V_{CL}^2 D_b^2\, V^* a_{yg}^* - V_{CL}^2 D_b^2\, v_{in}^*\, v_{yg}^* A_{or}^* + \frac{\pi D_b^2}{4}\left(\frac{2\gamma}{\rho_f\, D_b\, R_0^*} + \frac{\Delta\rho}{\rho_f} g D_b\, H^*\right) + V_{CL}^2\, D_b^2\, v_{in}^{*,2}\, A_{or}^* - g\frac{\Delta\rho}{\rho_f} D_b^3 V^* - \frac{D_b \pi\gamma}{\rho_f}\sin\theta = 0 \tag{43}$$

Following these rules we obtain a complete non-dimensional form of the vertical momentum balance, which can be used to verify the sine of the contact angle and the contact angle itself:

$$\sin\theta = -\underbrace{We\frac{V^* a_{yg}^*}{\pi}}_{\text{acceleration}} - \underbrace{We\frac{v_{in}^{*,2}\, v_{yg}^* A_{or}^*}{\pi}}_{\text{mass increase}} + \underbrace{\frac{1}{2R_0^*} + Eo\frac{H^*}{4}}_{\text{overpressure}} + \underbrace{We\frac{v_{in}^{*,2}\, A_{or}^*}{\pi}}_{\text{injection}} - \underbrace{Eo\frac{V^*}{\pi}}_{\text{gravity}} \tag{44}$$

Where:

$We = \frac{\rho V_{CL} D_b}{\gamma}$	(45)
$Eo = \frac{g \Delta \rho D_b^2}{\gamma}$	(46)

The first two terms in right hand side of Eq. 43 represent the variation of the droplet overall momentum, due to acceleration and mass increase. The third and fourth terms account for overpressure due to curvature and bubble height. The third term, in particular, evidences that overpressure is the driving term, mainly at first instants of droplet formation. The fifth term is associated with injection and the sixth with gravity forces. The weight of the different terms is shown in Figure 43, for the lowest mass flow rate (0.005 ml/min).
It can be seen that the most relevant are:

$$\begin{cases} term\ 3 = \dfrac{1}{2R_0^*} \\ term\ 4 = Eo\dfrac{H^*}{4} \\ term\ 6 = -Eo\dfrac{V^*}{\pi} \end{cases}$$

Which are the only non-including dynamic variables (velocities and acceleration).

In Figure 44, a comparison between measured and calculated contact angle sinus is reported for low mass flow rates. The different terms in Eq.43 are estimated by the post-processing of digital videos. Figure 45 shows the discrepancy between measured and calculated contact angles, always below 1% for the selected boundary conditions. Similar results for higher mass flow rates (0.05 and 0.1 ml/min) are shown in Figure 46 through Figure 49.

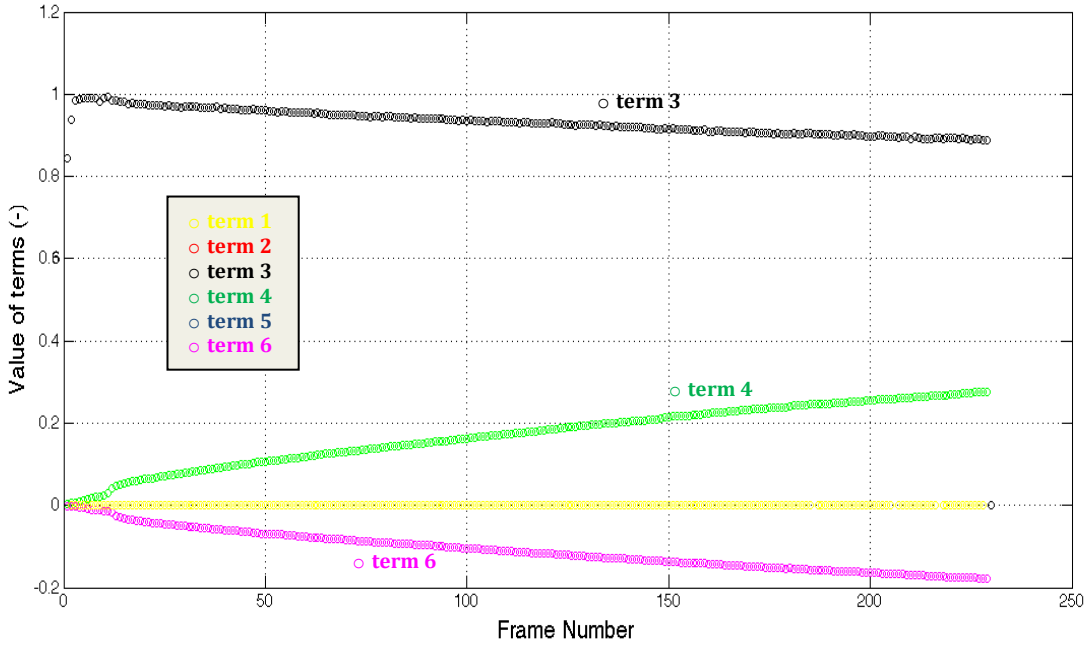

Figure 43: Weight of different terms in Eq. 43 (Q = 0.005 ml/min)

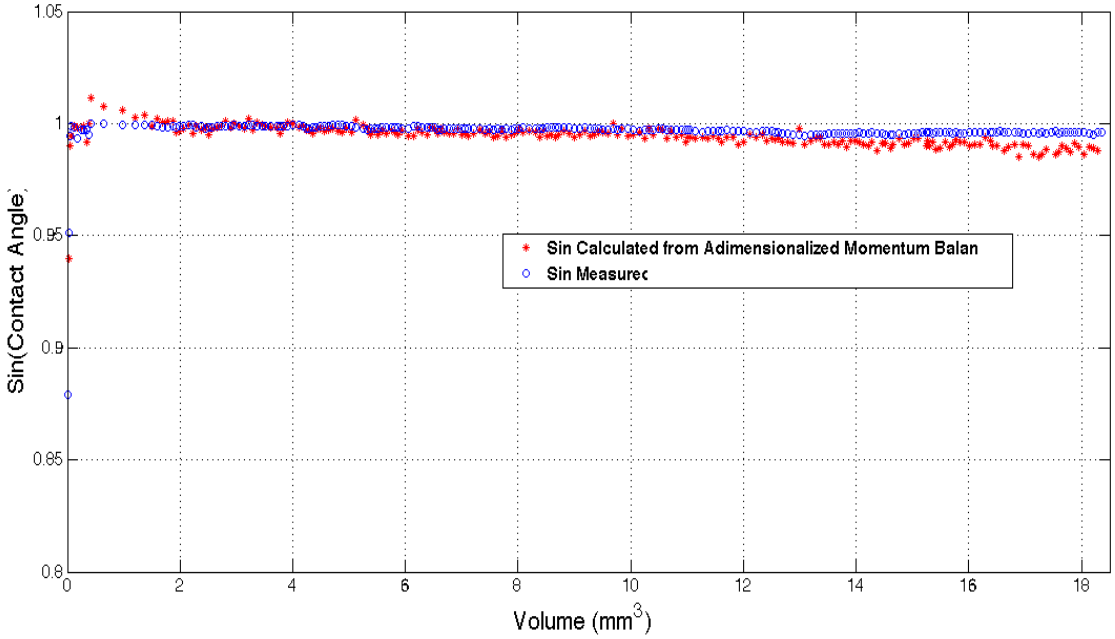

Figure 44: Comparison between predicted (Eq.43) and theoretical contact angle sinus (Q = 0.005 ml/min)

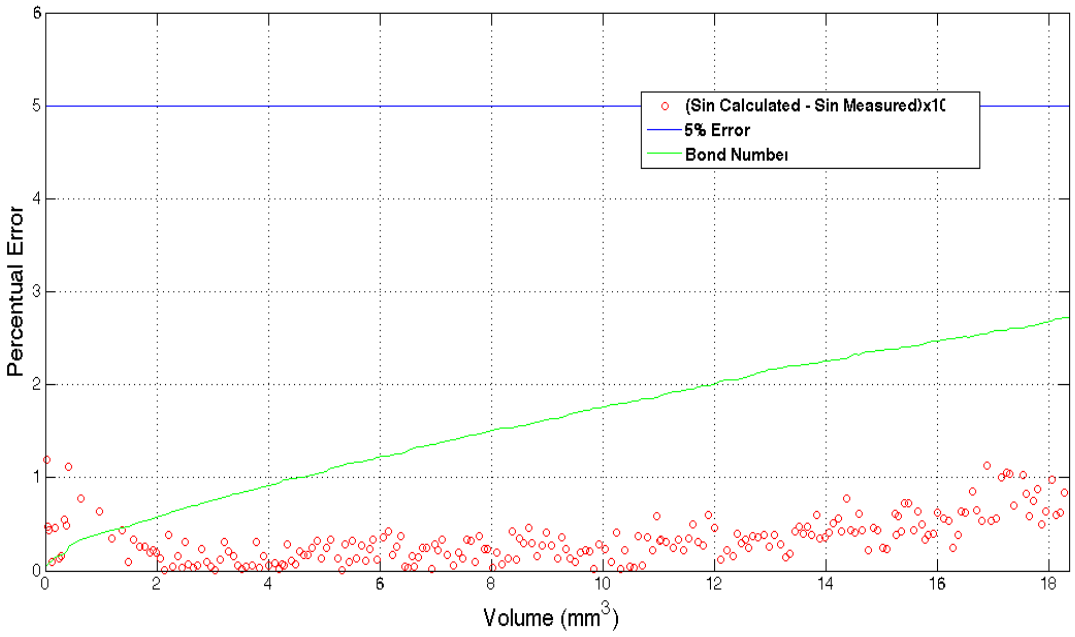

Figure 45: Discrepancy between calculated and theoretical contact angle sinus (Q = 0.005 ml/min)

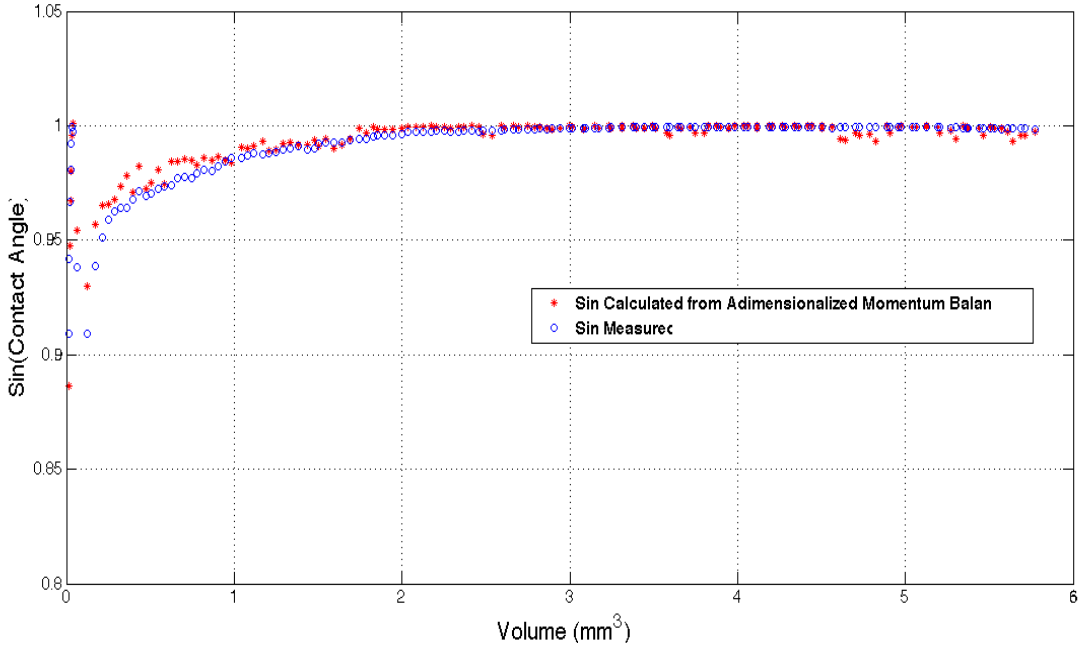

Figure 46: Comparison between predicted (Eq.43) and theoretical contact angle sinus (Q = 0.05 ml/min)

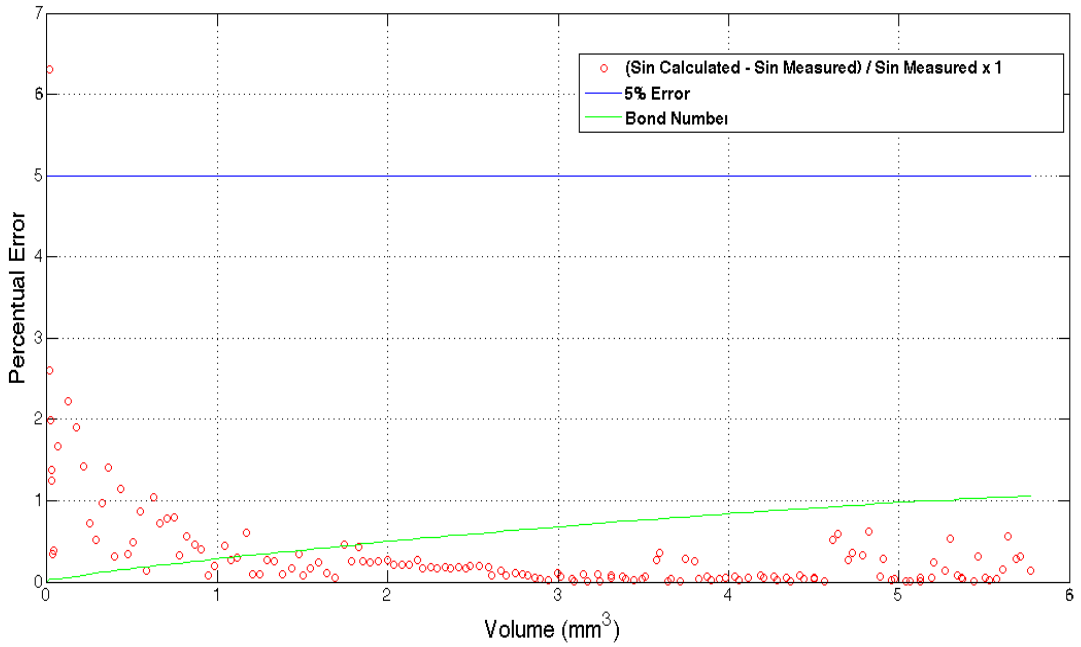

Figure 47: Discrepancy between calculated and theoretical contact angle sinus (Q = 0.05 ml/min)

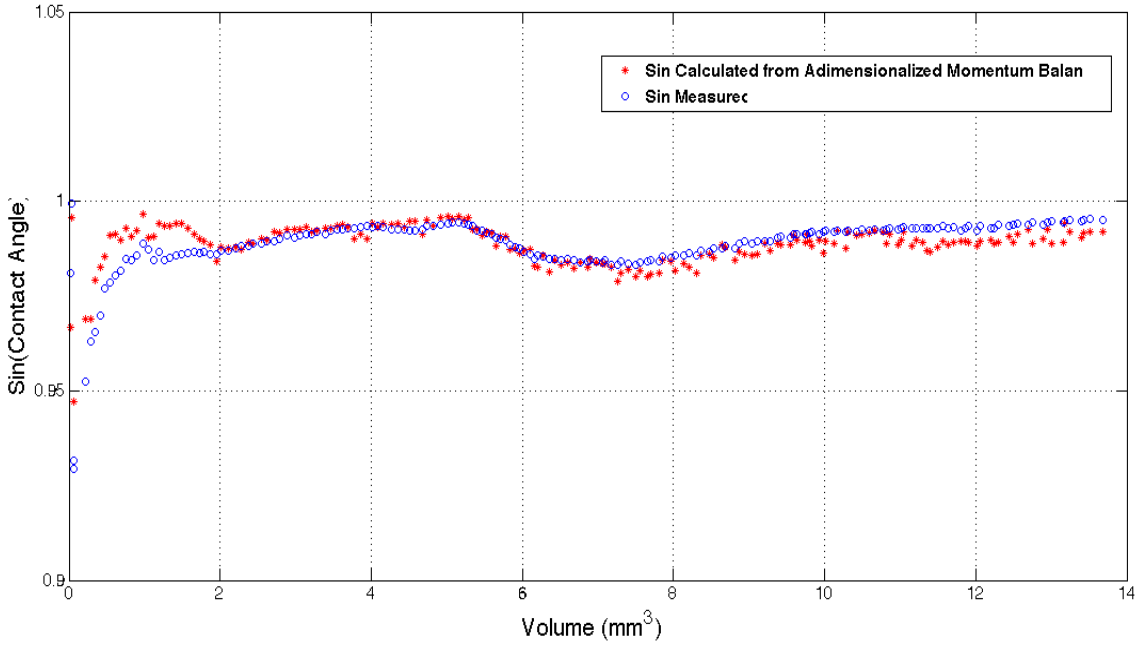

Figure 48: Comparison between predicted (Eq.43) and theoretical contact angles sinus (Q = 0.1 ml/min)

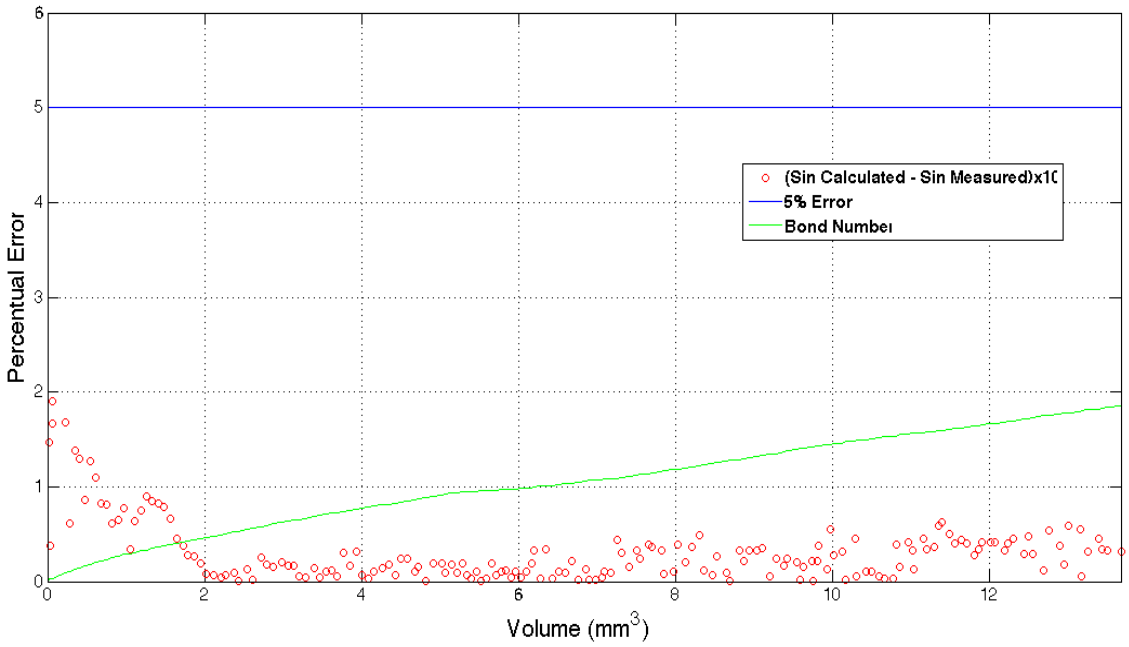

Figure 49: Discrepancy between calculated and theoretical contact angle sinus (Q = 0.1 ml/min)

Very large mass flow rates (Q = 1 ml/min) deserves a separate discussion since very high Bond number can be attained. As mentioned earlier, the Eötvös (or Bond, Bo) number is very influent in determining the drop shape:

- For very low Bo (typically < 0.1), the shape follows a very simple law: constant curvature (like spherical cap). Gravity effects are small compared to surface tension effects.

- For intermediate Bo ($0.1 < Bo < 3 \div 5$) the shape is no more spherical, but can be still reconstructed by the Laplace-Young Equation (with the modified routine developed for bubbles by Di Marco et al. [61], see Figure 50).

- For high Bo (typically > 3), the Laplace-Young Equation fails close to the droplet tip, but can still give a reasonable estimation close to the triple line. Reconstructing the bubble shape basing on the Konduru's method leads to a different droplet shape (see Figure 51). In particular, the wet radius is slightly higher (the difference is only 3%), the height of the drop is 7.4% lower, and the curvature radius is 28.7% lower. This disagreement is due to the relevance of gravity, which now seems to be dominating.

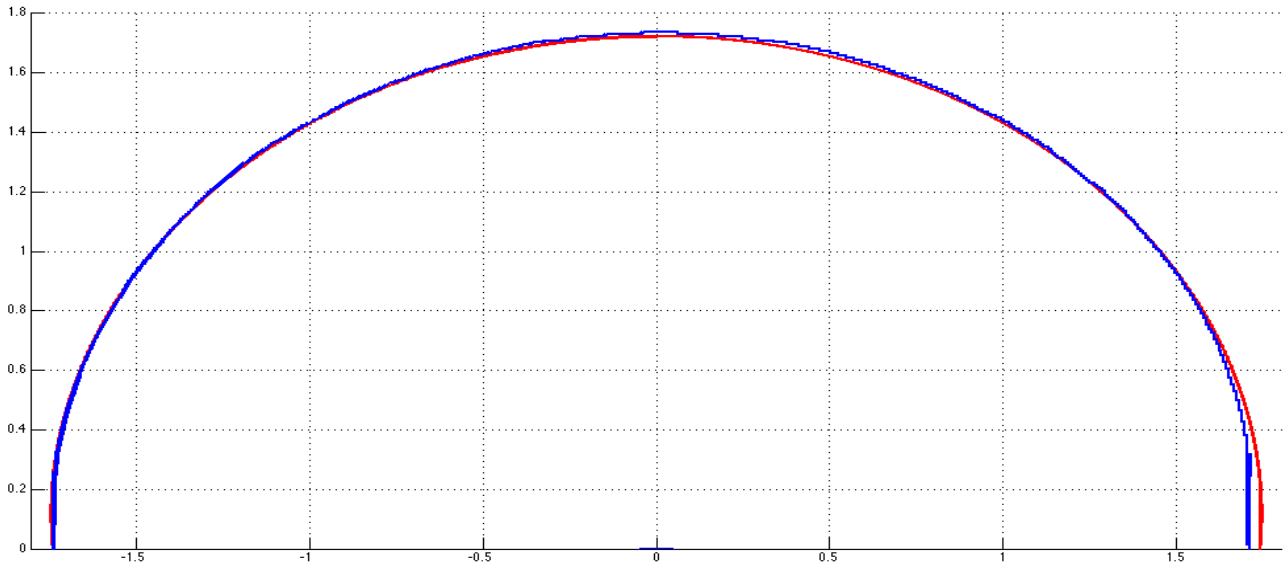

Figure 50: Comparison between calculated (red) and detected (blue) droplet profile (Bo = 1.6, Q = 1 ml/min, V=11.2 mm³)

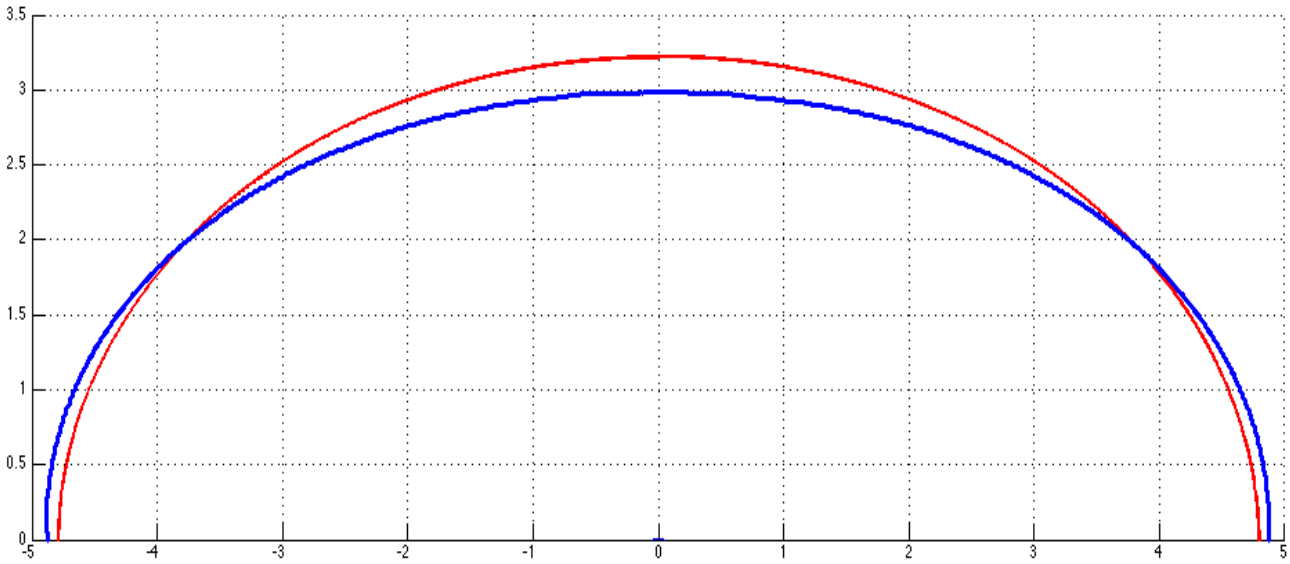

Figure 51: Comparison between calculated (red) and detected (blue) droplet profile (Bo = 12, Q = 1 ml/min, V=155.5 mm³)

In Figure 52 and Figure 53, we can appreciate how the Bond number influences the prediction of the contact angle sinus. For $Bo < 3 \div 5$, calculated and measured contact angles are in good agreement. However, for higher Bond numbers, they can be much different.

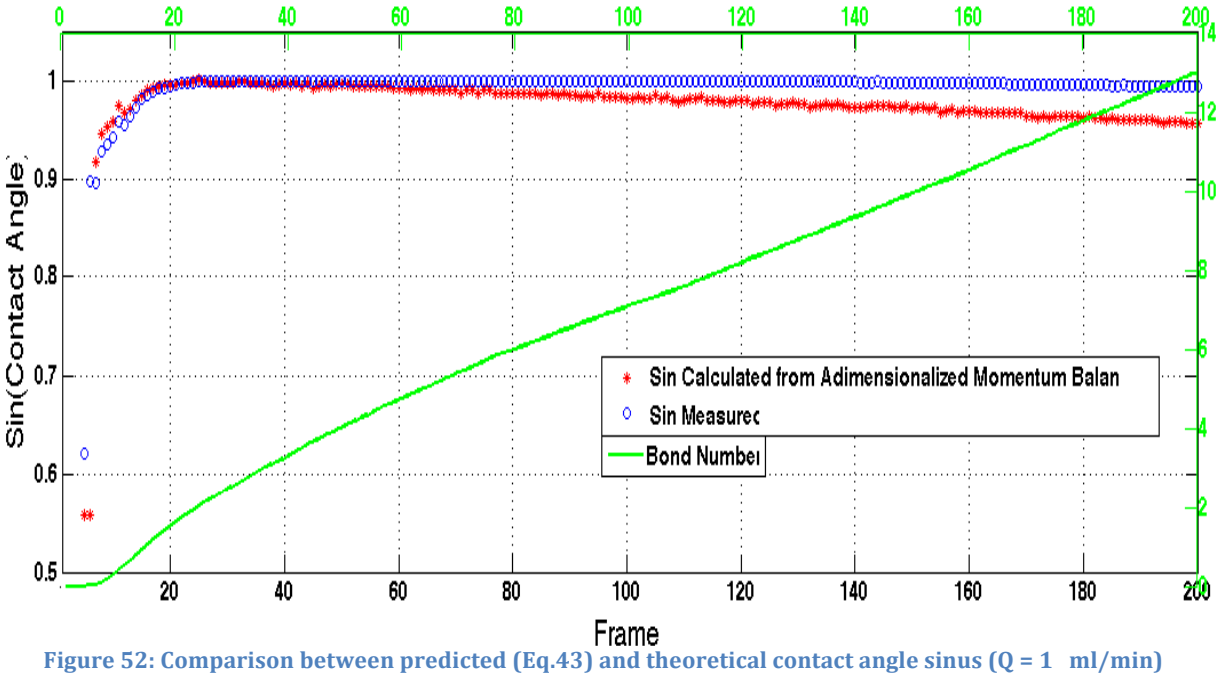

Figure 52: Comparison between predicted (Eq.43) and theoretical contact angle sinus (Q = 1 ml/min)

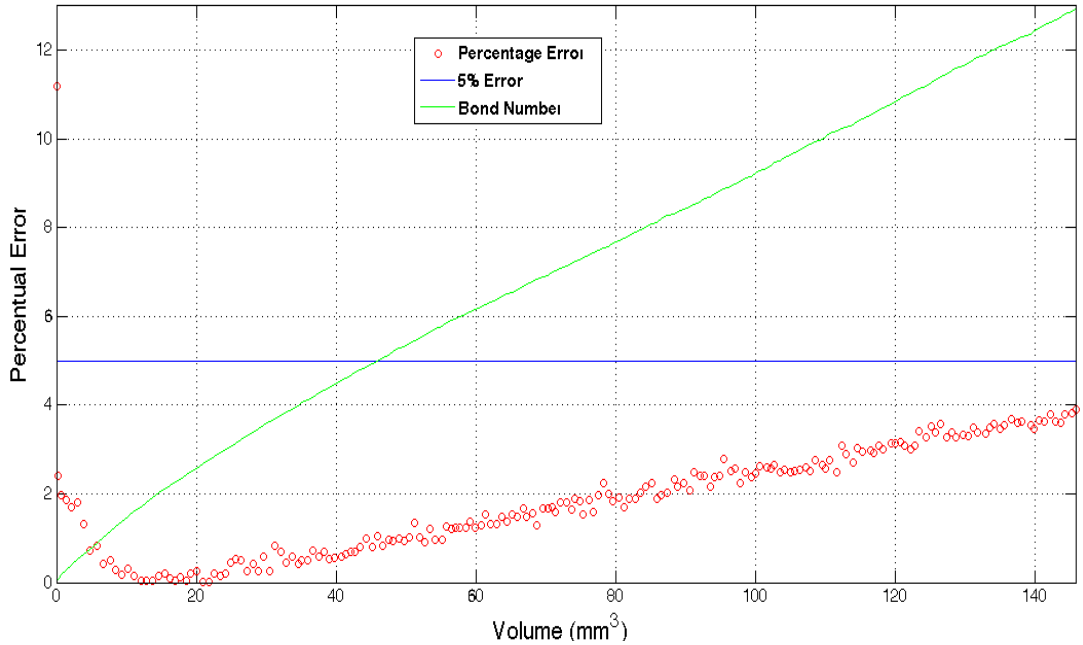

Figure 53: Discrepancy between calculated and theoretical contact angle sinus (Q = 1 ml/min)

Eventually, in Figure 54 through Figure 57, the contact angle as a function of the volume is shown for the four mass flow rates. The results confirm that the agreement between theoretical and measured contact angles is very good for relatively small Bond numbers (<5). For higher Bond numbers, measured contact angles tend to be higher than those expected in absence of body forces.

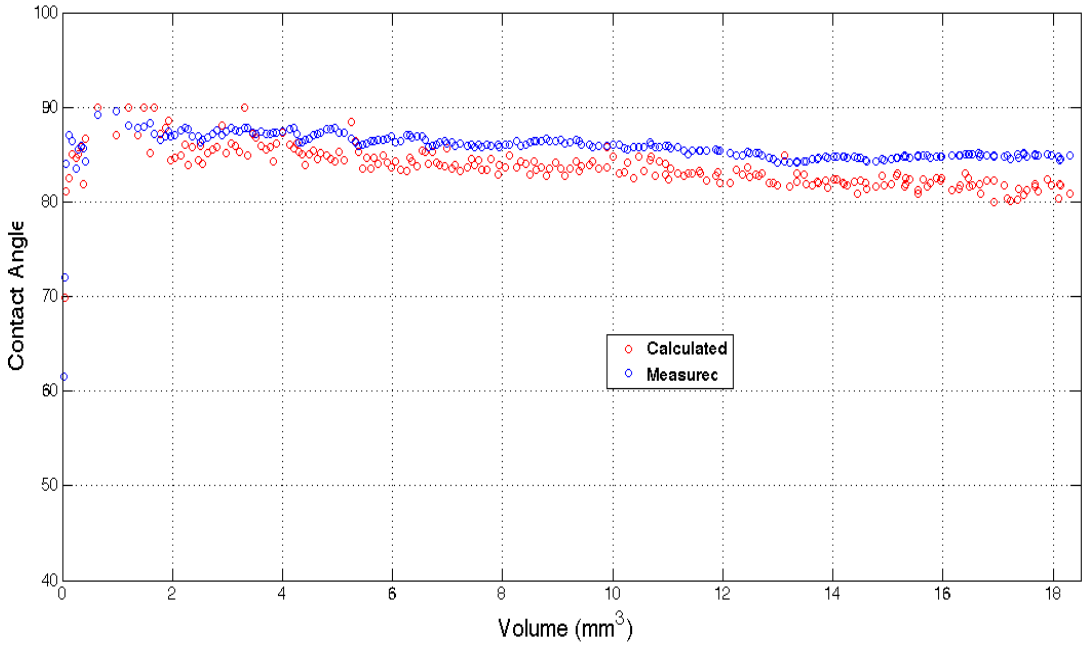

Figure 54: Comparison between predicted and theoretical contact angles (Q = 0.005 ml/min)

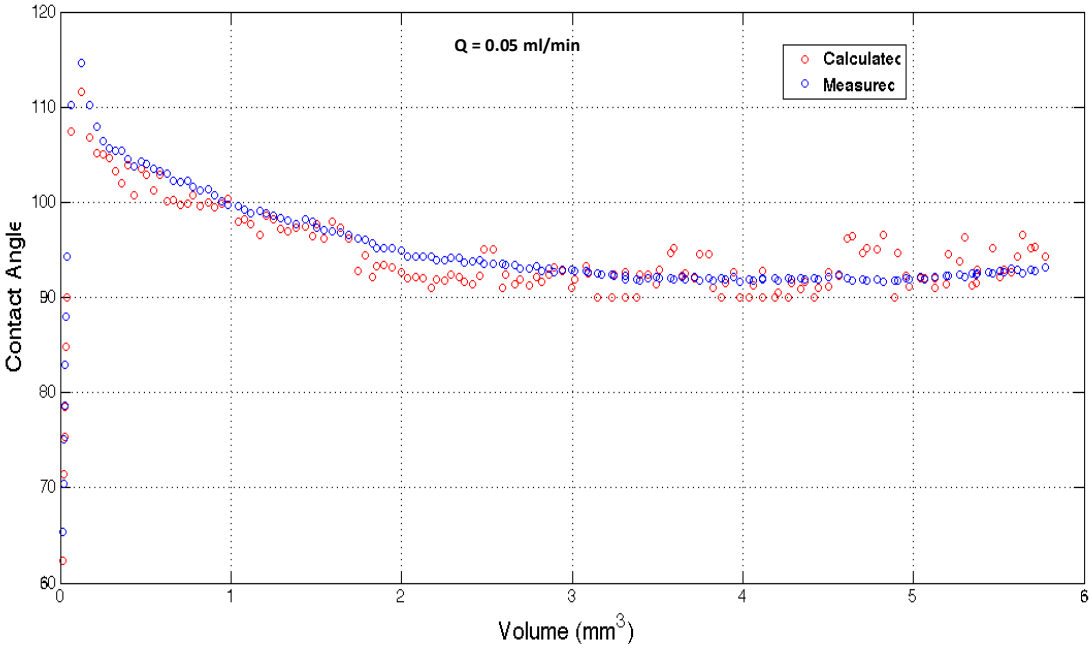

Figure 55: Comparison between predicted and theoretical contact angles (Q = 0.05 ml/min)

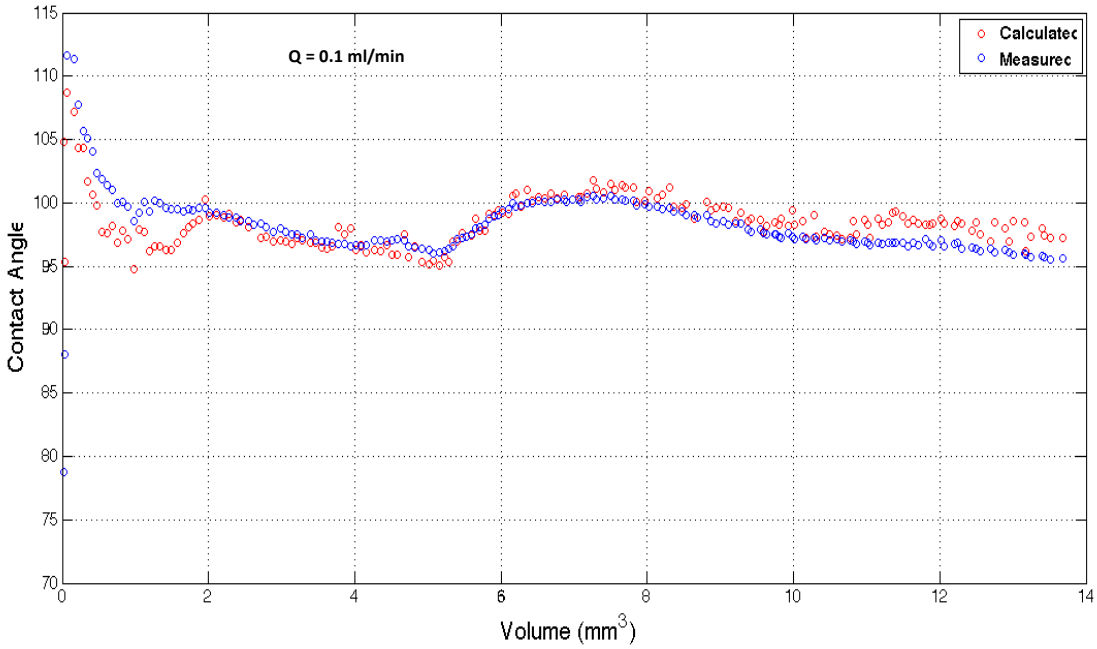

Figure 56: Comparison between predicted and theoretical contact angles (Q = 0.1 ml/min)

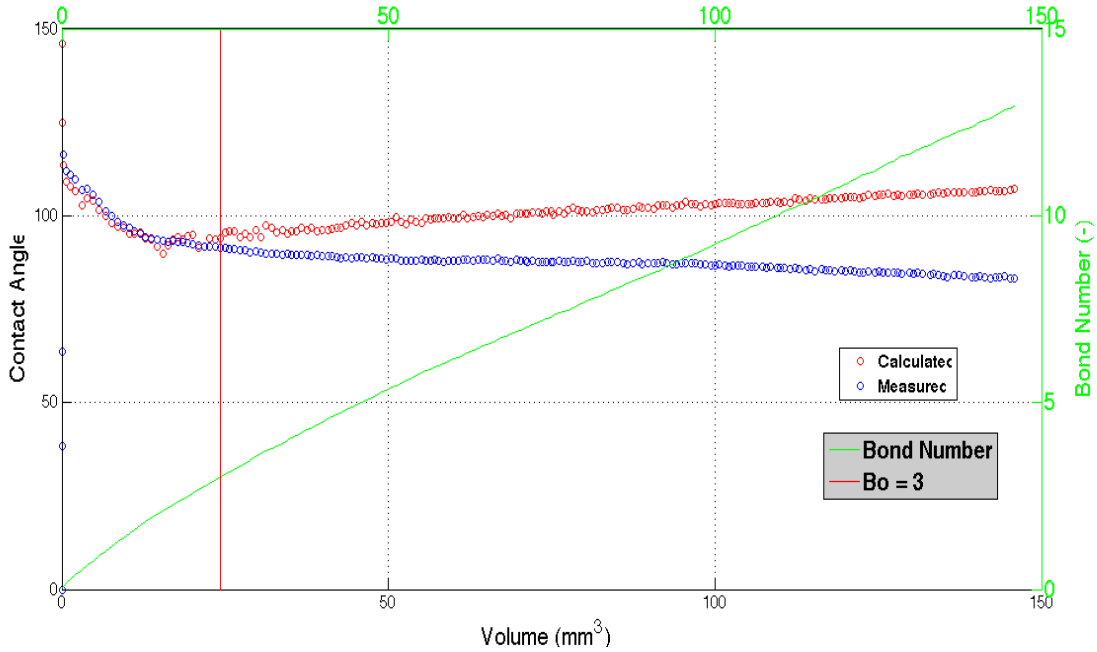

Figure 57: Comparison between predicted and theoretical contact angles (Q = 1.0 ml/min)

The importance of choosing appropriate scales is emphasized by the evaluation of the Weber and the Eötvös numbers. The result shown in Figure 58 for the Weber number suggests that, even if the We is very small (around 10^{-6}) for all the flow rates, it decreases with increasing volume. Therefore, the triple line velocity, V_{CL}, is the dominant quantity in the range of small volumes, and this is not straightforward since, as shown by Eq. 44, there is also the wet diameter, D_b to multiply the triple line velocity.

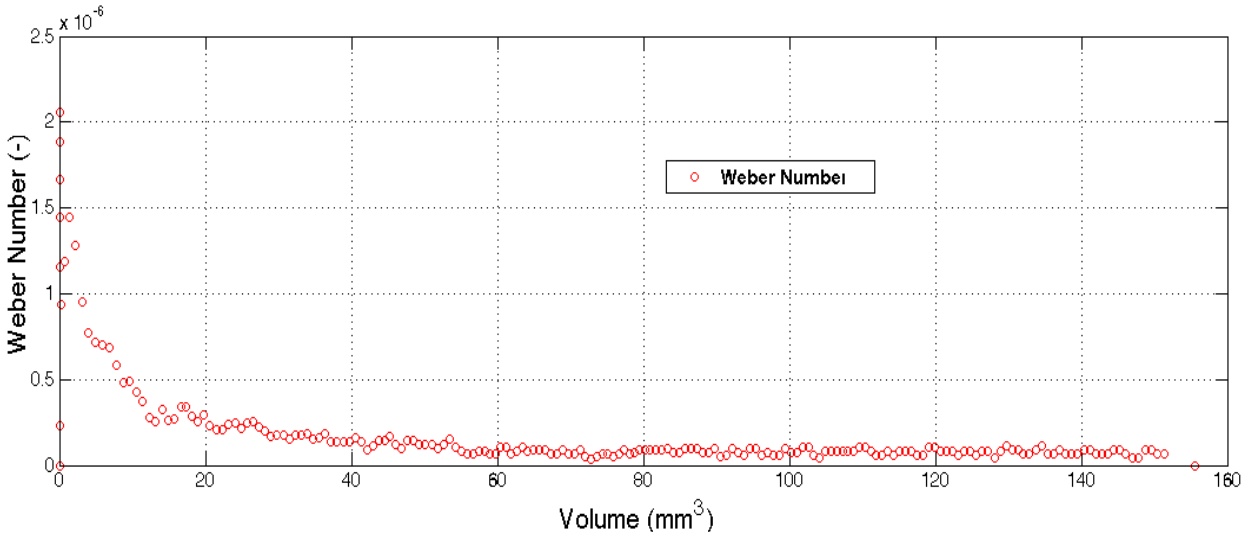

Figure 58: Weber number vs. droplet volume (Q= 1 ml/min)

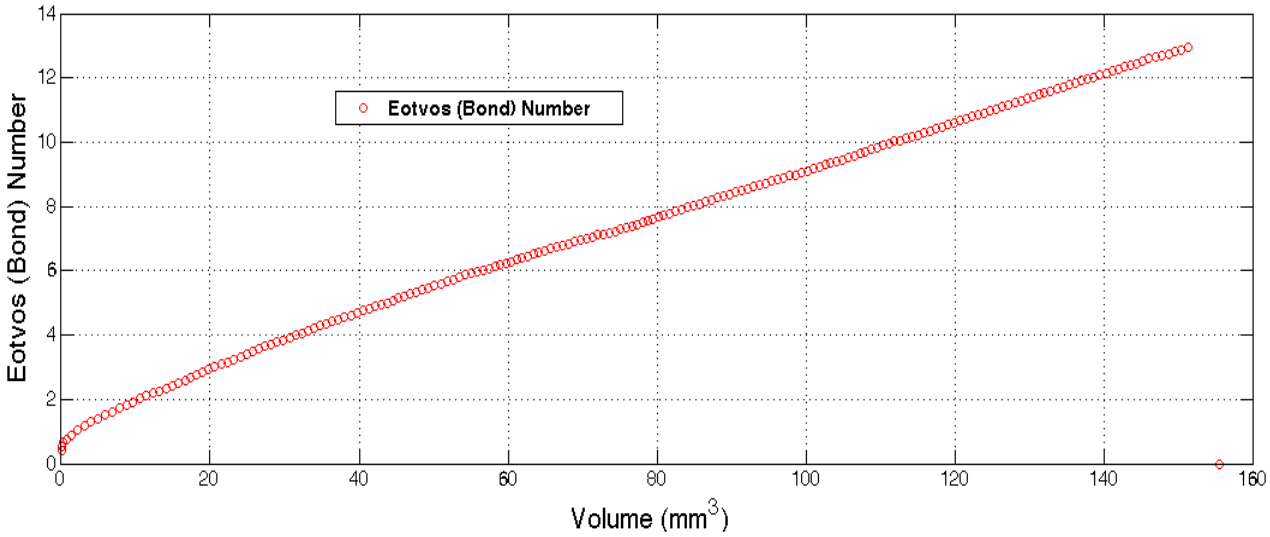

Figure 59: Eotvos number vs. droplet volume (Q=1 ml/min)

7 Experimental technique to estimate surface tension

Surface tension is one of the unknowns in the Konduru's method to analyse droplet or bubble profiles. Therefore, the shape of a sessile droplet can be used to estimate the surface tension between the liquid and the surrounding atmosphere. In order to evaluate this physical property, we should satisfy two conditions, according to Hansen [65] Woodward [66]:

- The drop has to be axisymmetric;
- The drop is not in motion, to avoid viscous or inertia effect in determining the droplet shape.

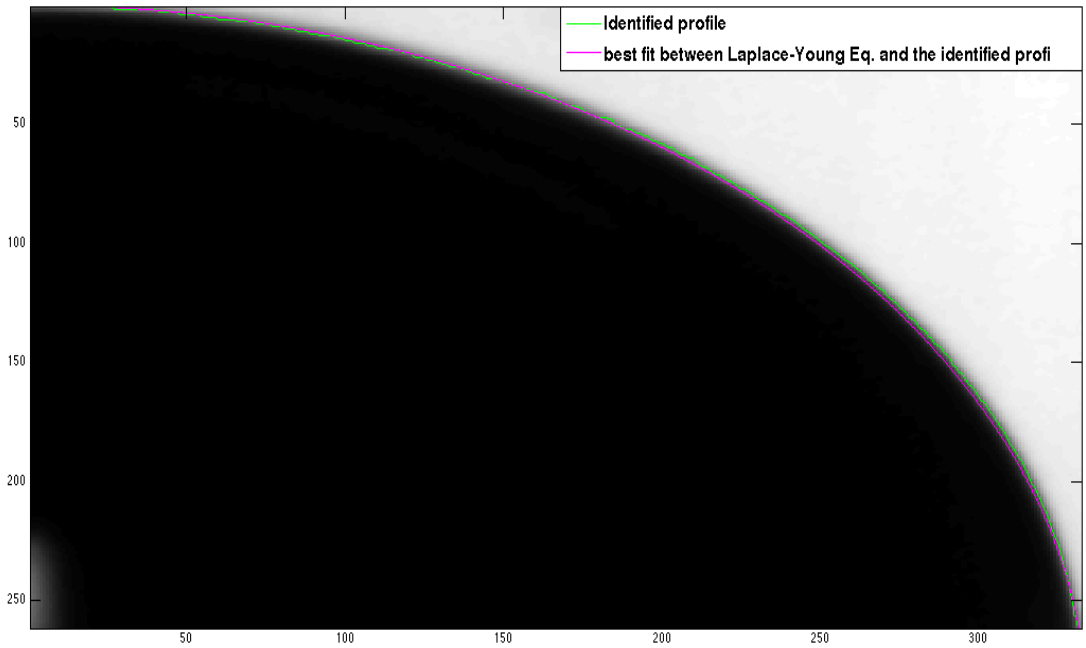

Figure 60: Comparison between the actual droplet profile and the one obtained by the Konduru's method

In this study, we made different measurements: for drop at rest and for dynamic droplets, pushed by the inlet flow rate. For what concerns drop at rest, experimental data are largely available in literature and confirmation tests for our apparatus have also been performed (see Figure 62).

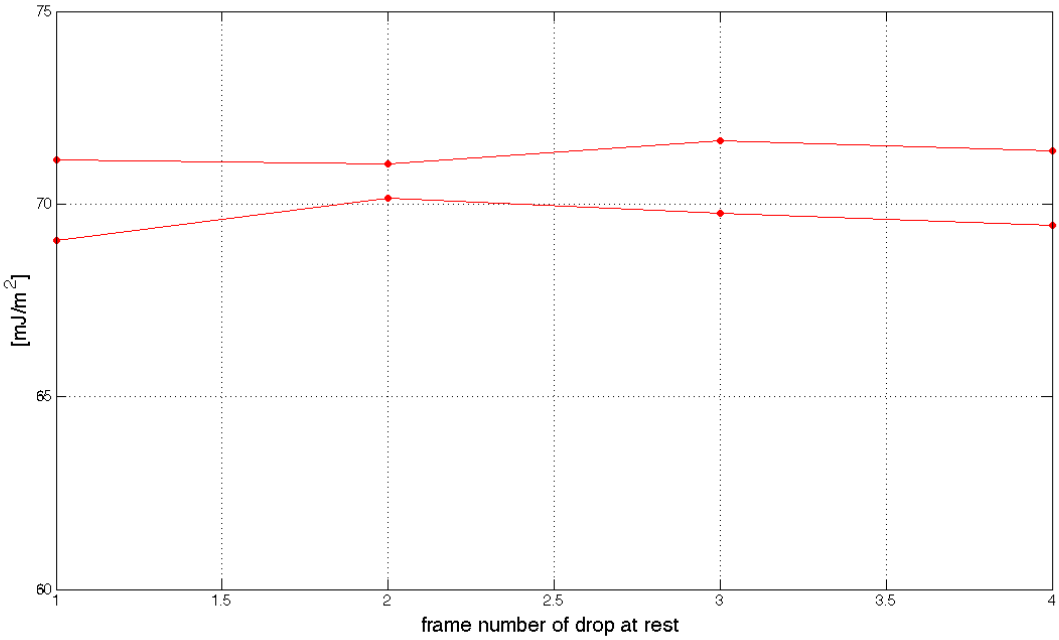

Figure 61: Surface tension for different drops at rest

However, since we are dealing with dynamic droplets, we wanted to understand how dynamic conditions affect the surface tension prediction. Actually, the one we calculate from the shape of dynamic drop is not the actual surface tension, which is a physical property. What we are now finding is a sort of *dynamic* surface tension: it is the surface tension that our liquid should have to satisfy completely the Laplace-Young Equation. These results are shown in Figure 62.

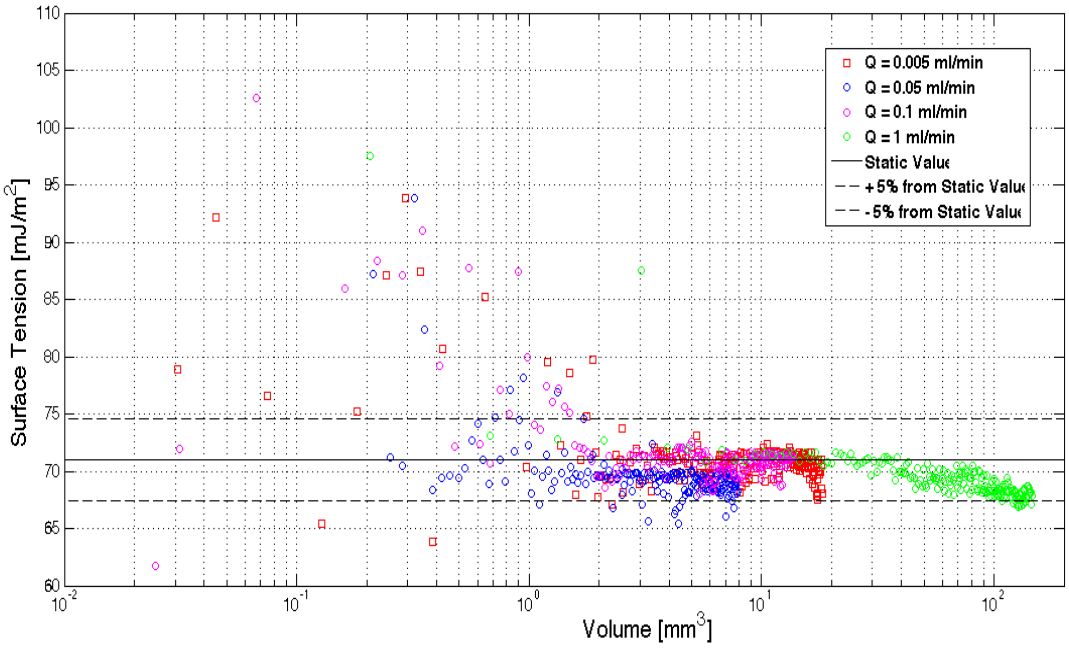

Figure 62: Surface tension vs. volume for different mass flow rates

As expected, the higher is the volume, the less important is the inlet flow rate contribution to the shape; thus, for higher volumes, dynamic surface tensions match better with the physical value. However, for too large volumes, the Bond number will be too high and the shape won't follow

Laplace-Young Equation, leading to an error in the evaluation of Surface Tension. After Figure 62, a general trend can be therefore inferred: the smaller is the volume, the higher is the *dynamic* surface tension calculated from the profile. Obviously, for smaller volume we have fewer pixels for Laplace-Young curve fitting, so the error itself is higher. However, for smaller volumes we also have a higher triple line velocity, so a stronger dynamic regime. This is valid for all the flow rates analysed.

8 Contact angle

The dynamic contact angle is a key parameter for this work. In the past, it has been correlated only with the triple line velocity ([18], [19], [20], [21], [22], [23] & [24]]. Actually, it seems to depend from several additional parameters: volume of the drop, thermodynamic surface tension and, most of all, from the conditions of the flow inside the drop in the proximity of the triple line [39], [29], [28].

"This result means that ϑ_D is not just speed-dependent, but dependent on the details of the flow. This result also implies that all theories and empirical correlations that lead to a single relationship between ϑ_D and U for a given system must, at best, be incomplete".

Blake [29].

Even if the value of the contact angle might differ for the different flow rates, a general tendency during the spreading process, from the first time where the droplet is emerging from the orifice to the late stage of spreading, can be seen in Figure 65, and can be summarized as follows:

- A first "strongly disequilibrium phase" characterises the first instants: typical value of the contact angle is between 120° and 100°. During this phase, we observe the highest velocity of the triple line.

- A second "transition phase" where the contact angle changes quickly from the values of the first phase (over 100°) to values closer to the static contact angle, but still a little larger. During this period, also the velocity changes sharply from the initial phase and start to decrease

- The third and last phase is a "quasi-static phase", where the contact angle is slightly over the static contact angle and the velocity of the droplet is very low.

The change from one phase to another and the duration of each phase depends only on the flow rate. As obviously expected, the smaller is the droplet and higher is the velocity of the triple line. See Figure 64.

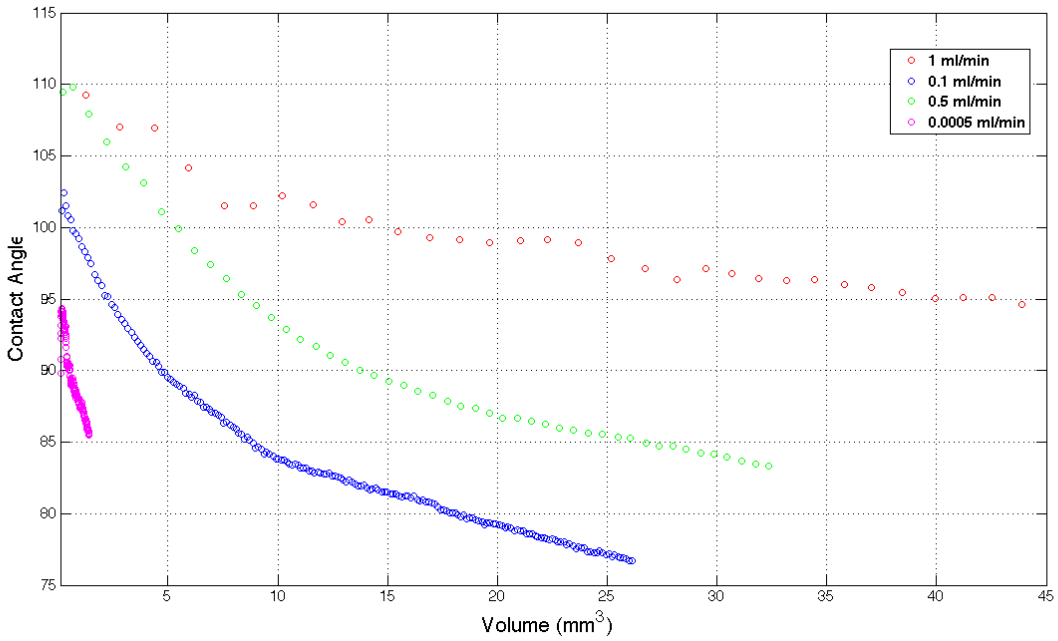

Figure 63: Contact angle vs. volume of the droplet for different flow rates

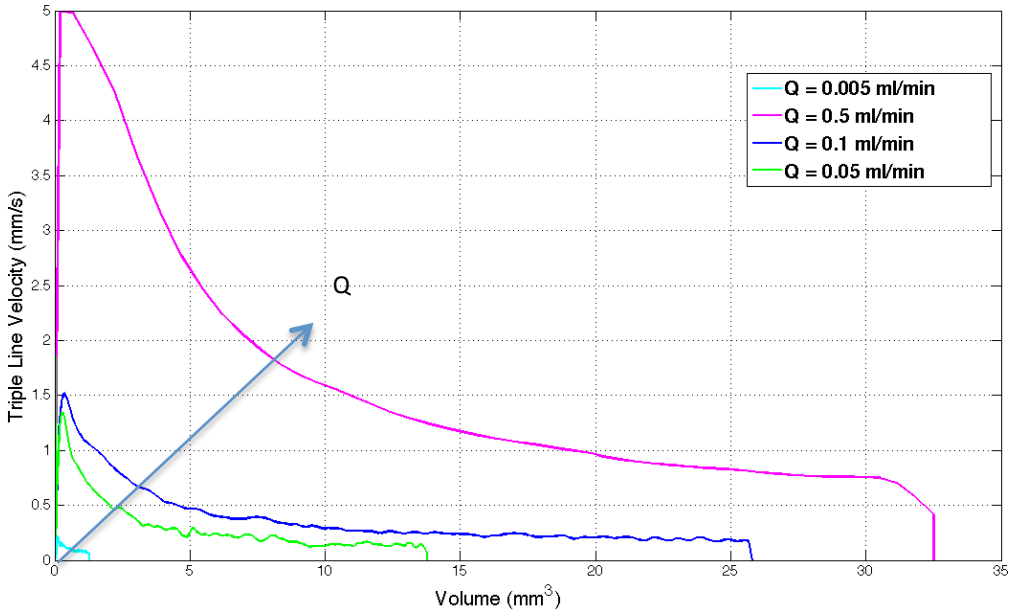

Figure 64: Triple line velocity vs. volume for different flow rates

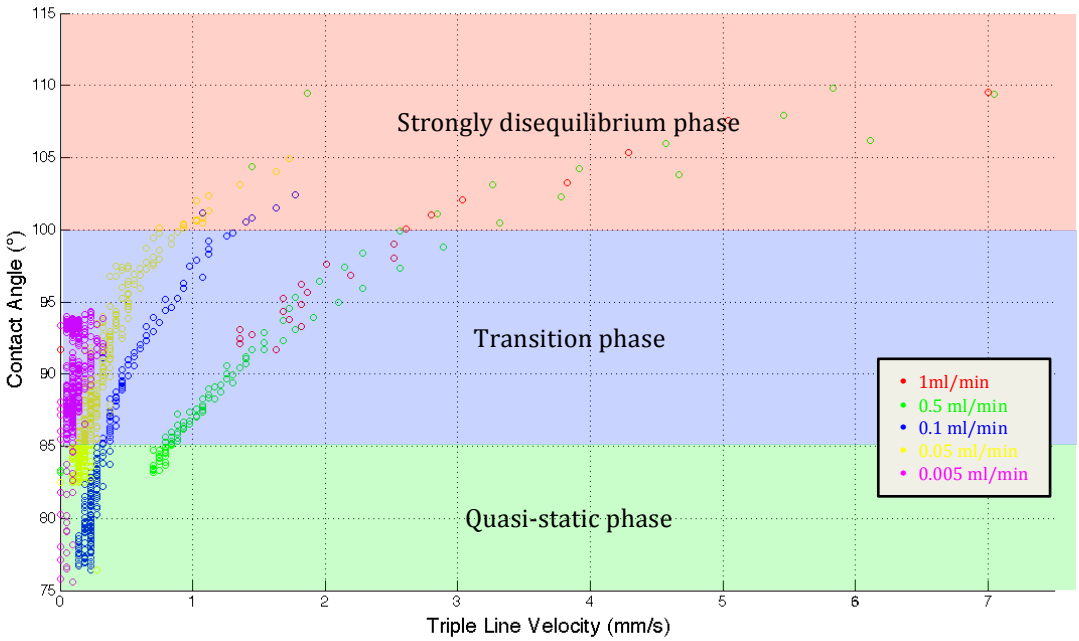

Figure 65: Contact angle vs. triple line velocity

Plots shown in this paragraph are the results of the Aluminium series data processing.
It is important to point out that the static contact angle measured for the couple water-aluminium is between 65° to 75°, approaching the region of "quasi-static phase".

A note on reproducibility has to be said to underline the fact that most of the results of tests taken in the same conditions are comprised in a small gap. The worst reproducibility condition concerns the contact angle, that's the reason why it is important to show its behaviour with respect to volume. There seems to be difference in contact angle behaviour with respect to the history of the droplet: if it comes out from the orifice ($Volume = 0$) and if it comes from a relaxing condition, usually hysteresis driven.

For tests carried on with the same history, the reproducibility is well established, as can be assessed from Figure 66.
But, if the history differs, it can happen that the initial behaviours are a little bit different. In any case, equilibrium is then established and the same contact angle history is finally found. Depending just on the flow rate. See Figure 67.

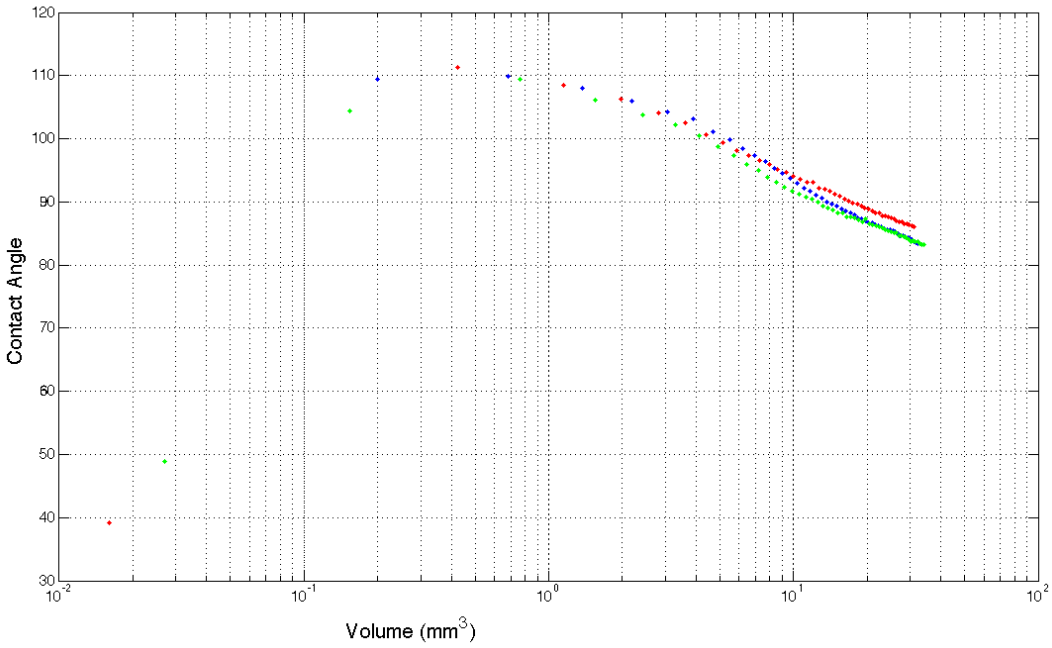

Figure 66: Reproducibility behaviour of droplets with the same flow rate (0.585 ml/min) coming out from the orifice

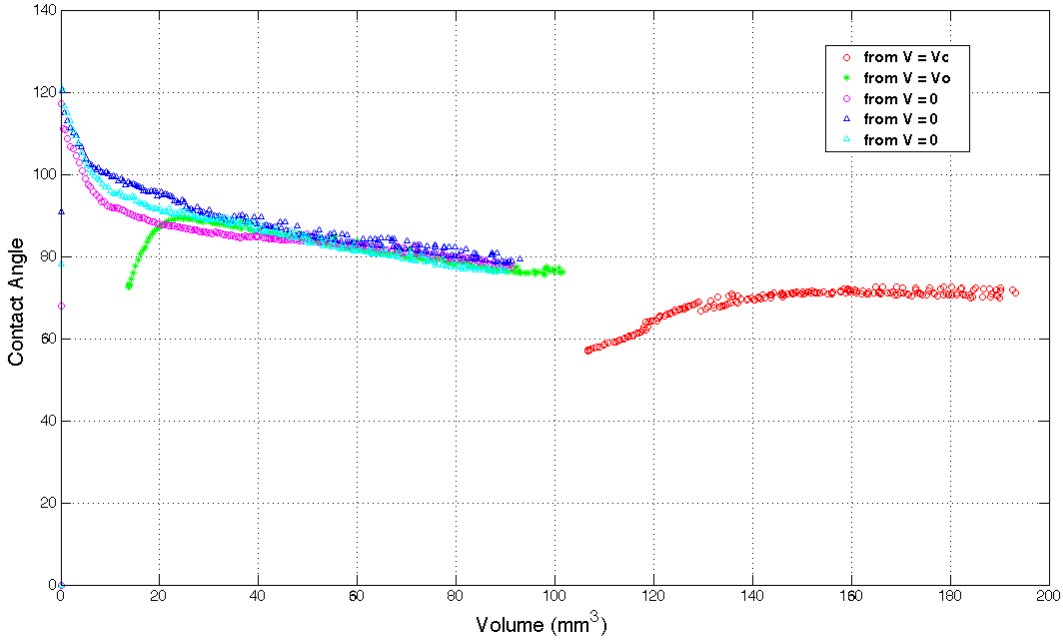

Figure 67: Reproducibility behaviour of droplets with the same flow rate (0.422 ml/min) with different histories

9 Momentum balance within radial approach

Since in the present study we are interested in droplet spreading, the radial dynamics has to be investigated. In this aim, we addressed the problem in two different ways.

This deepening arises from considerations carried out in Section 7 on surface tension.
As we saw, the calculated surface tension (that we called dynamic surface tension) is higher than the actual surface tension, for droplets spreading with large triple line velocities.
It can be explained according to Panton [67]:

$$\vec{n}\cdot\left(p_f - p_g\right) = m''\left(v_f - v_g\right) - \vec{n}\cdot\left(\overline{\overline{T_{v,f}}} - \overline{\overline{T_{v,g}}}\right) + 2\gamma\vec{n}K \tag{47}$$

Clearly, when the viscous stresses $(\overline{\overline{T_{v,f}}}; \overline{\overline{T_{v,g}}})$ are negligible and liquid phase and gas phase moves with the same velocities $(v_f = v_g)$, the equation reduces to the Laplace-Young.
But if we use the Laplace-Young equation "as is" to fit and analyse spreading droplets, we will obtain a value of surface tension, different from the actual one, which, to some extent, embeds viscous effects.

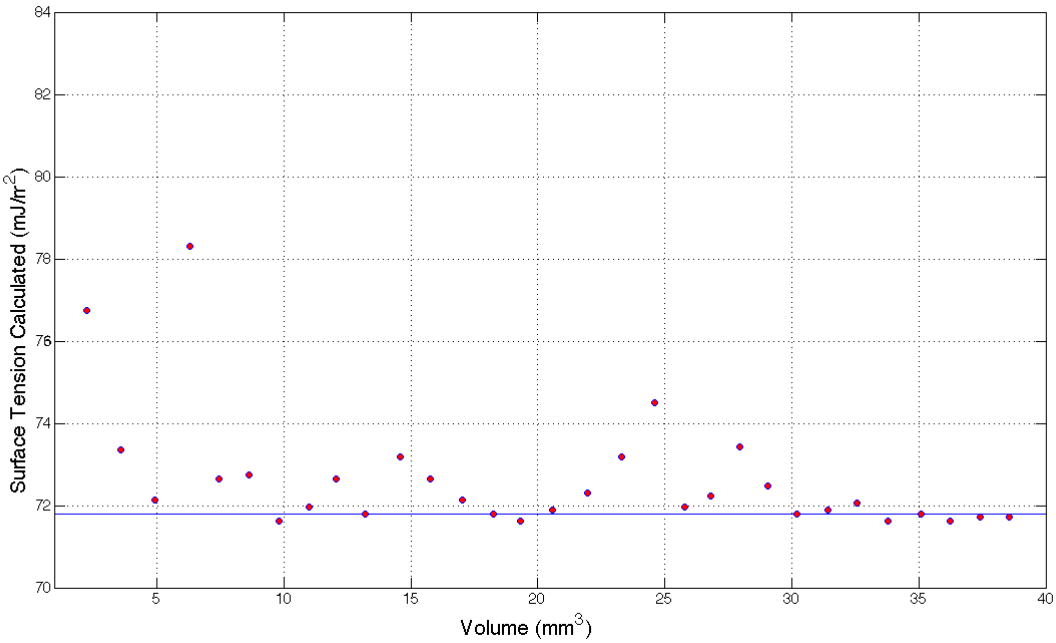

Figure 68: Calculated surface tension vs. volume.
Note that smaller drops are also characterized by highest velocities.

Percentage difference between the thermodynamic and the artificial dynamic surface tension is at most of the order of 25%. It means that there is a difference between the actual curvature and the curvature imposed by static-equilibrium:

$$\left(\frac{1}{R_1} + \frac{1}{R_2}\right) = \frac{2}{R_0} + \frac{\left(\rho_f - \rho_g\right)gy}{\gamma} \tag{48}$$

Difference in curvature means difference in stresses across the surface of the droplet, as shown by Eq. 27 and 28.

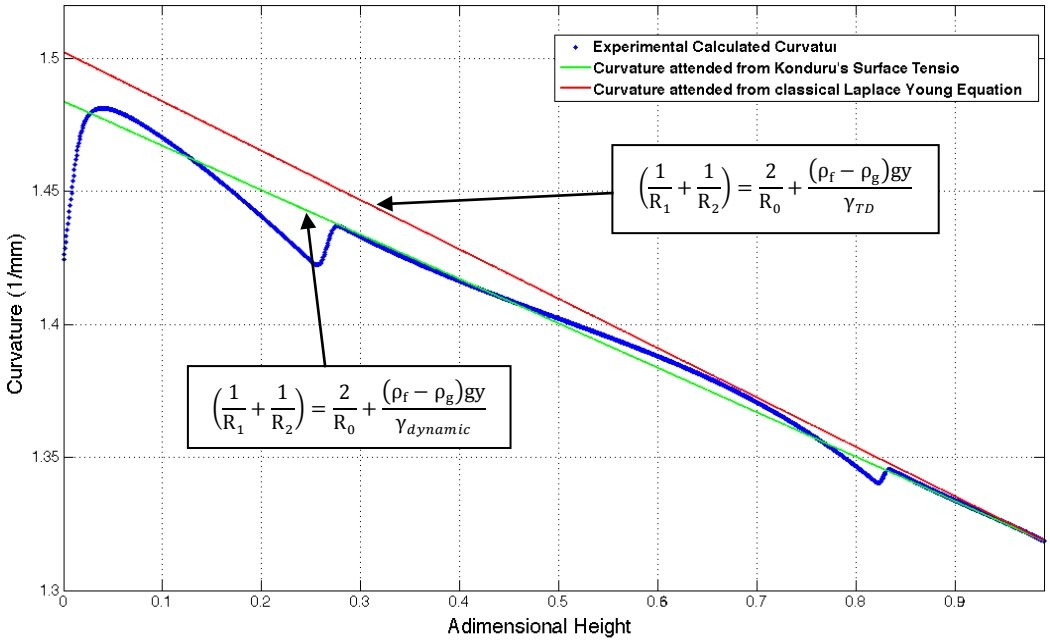

Figure 69: Curvature vs. height; red line represents the static curvature of a droplet with the same curvature radius at drop top, green line represents the average curvature evaluated during spreading (blue points).

The first method to calculate a radial force balance is to integrate this pressure difference all over the droplet interface and projecting it in the radial direction in a cylindrical coordinate system (*r*,*z*). Unlikely, this curvature difference is usually of the order of some %, with a maximum of 10% for smaller droplets.

At drop top, using Eq. 47:

$$\left(p_{f,top}-p_{g,top}\right)=\frac{2\gamma_{dynamic}}{R_{top}} \tag{49}$$

Mathematically speaking, we are just integrating Laplace-Young equation, to catch the difference due to spreading/motion:

$$\int_S \left(p_f-p_g\right)\ (\vec{n}\cdot\vec{r})\,dS=\int_S \gamma_{TD}\ \kappa\ (\vec{n}\cdot\vec{r})\ dS \tag{50}$$

Numerically speaking, we have just to project all surface elements *dS* in the radial direction and integrate them, after having multiplied them for the local value of pressure in the first integral, for the value of thermodynamic surface tension and local curvature in the second integral.

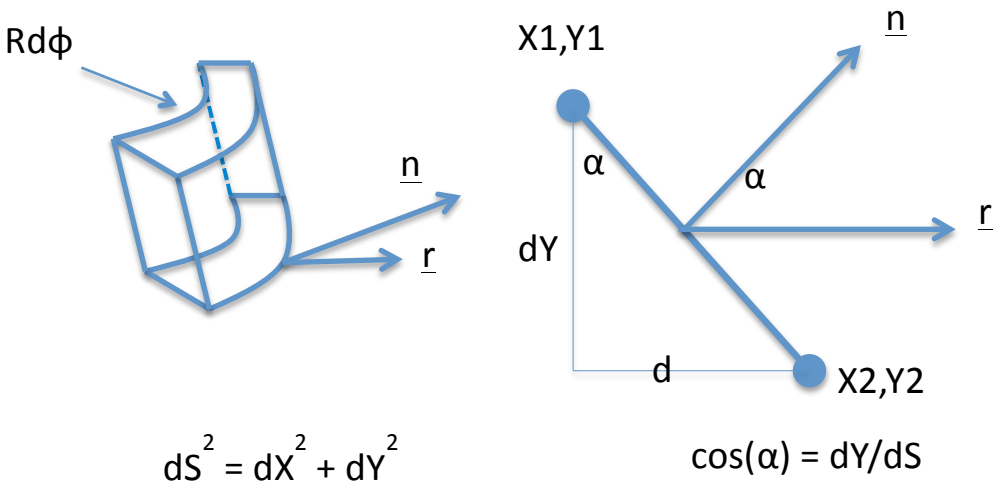

Figure 70: explanation of the numerical

- The value of local pressure is (assuming y=0 at drop top, positive direction downward):

$$(p_f - p_g) = \frac{2\gamma_{dynamic}}{R_0} + (\rho_f - \rho_g)gy \qquad (51)$$

- The value of local "curvature response" has been found point by point using a second order polynomial regression, as pointed out in Paragraph 4 (Post processing techniques). The value of local curvature is then multiplied for the thermodynamic surface tension.

In subsequent figures, this methodology to calculate the radial surface tension force will be called "mode-1".

The reason of this different use of surface tension (*dynamic* one in calculating the pressure term (51), *thermodynamic* one in calculating the curvature response) is due to the fact that the dynamic surface tension is the tension needed by the droplet to achieve a complete fulfilment of Laplace-Young Equation, whereas the thermodynamic surface tension is a property of the liquid and varies only with temperature. Since we get the actual value of pressure at each point of the interface with the Laplace-Young relation, we have to consider the dynamic value of surface tension.
Since the restraint force is the force containing the fluid in its shape, and is thermodynamic in nature, we have to use the thermodynamic value of surface tension.

A second way to approach the radial force balance is to take a control volume and study the equilibrium. Our control volume is a slice of the drop and we have to make balance considerations over its boundaries, as follows:

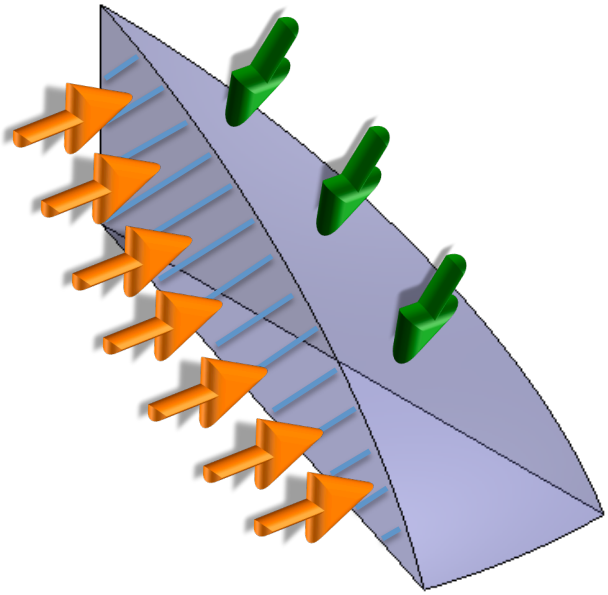

Figure 71: Force acting over the control volume. Pressure of the liquid in orange, pressure of air in green

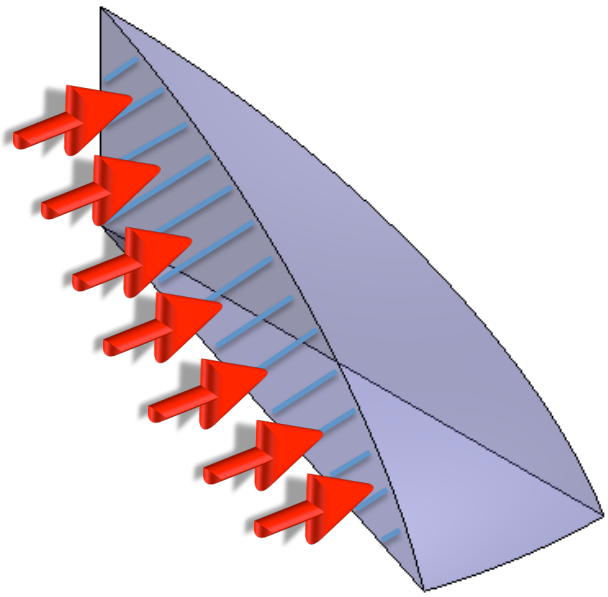

Figure 72: Resultant of pressure forces acting over the control volume

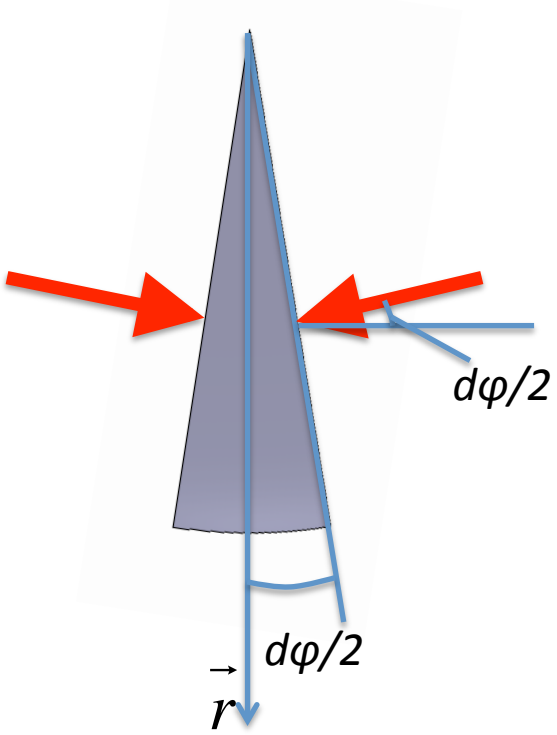

Figure 73: Decomposition of the resultant pressure force along the radial direction

In formulae, pressure force over the boundary shown in Figure 71, Figure 72 and Figure 73 comes as:

$$2\iint \left(p_f(z) - p_g(z)\right)(\vec{n}\cdot\vec{r})\,dr\,dz = \int_0^H \int_0^{r(z)} \left(p_f(z) - p_g(z)\right) d\phi\,dr\,dz \tag{52}$$

$$(\vec{n}\cdot\vec{r}) = \sin\left({}^{d\phi}/_{2}\right) \cong {}^{d\phi}/_{2}$$

With $d\phi$ ranging from 0 to 2π.
The expression is calculated with the aid of a MATLAB routine considering every point of the interface and came out to be just the same as before (Figure 70 and first integral of Eq. 49).

What now is different is the way we are taking into account restraining forces. As depicted in Figure 74, Figure 75.

Note that pressure force is multiplied for the patterned area (Figure 72), while surface tension is multiplied for the blue line (Figure 74), thus leading to a term dependent from the contact angle, which can contribute to spreading (positive contribution along radial direction) or can resists to it (negative contribution along radial direction).
The behaviour of this contribution will be underlined later on.

Note that force arrows are plotted just on half the control volume: the value of integral (52) and of first term in integral (53) are multiplied by 2 for this reason.

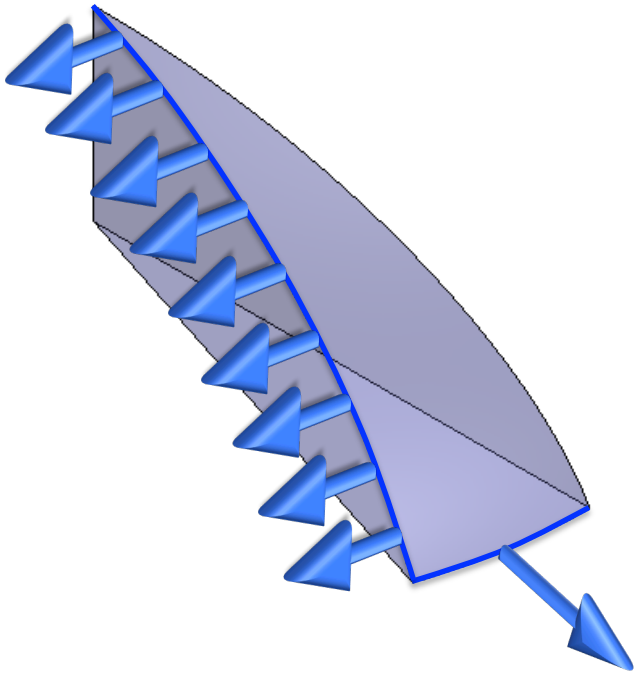

Figure 74: Surface tension force acting over the control volume

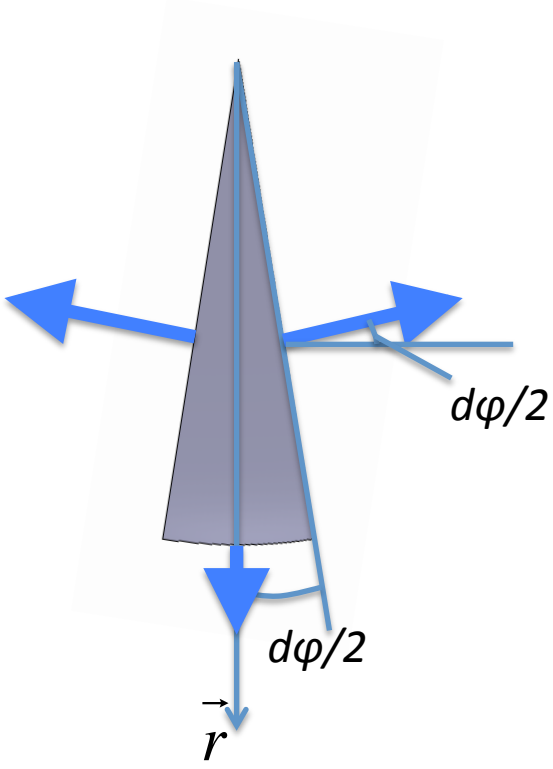

Figure 75: Decomposition of surface tension force along the radial direction

So, following Figure 74 and Figure 75, we get to the expression of surface tension force in radial direction:

$$\int_0^{2\pi} \left[2\,\gamma\,L\,\sin\left({}^{d\phi}/_{2}\right) + \gamma\,\cos\vartheta\;r\,d\phi\right] = \int_0^{2\pi} \left[\gamma\,L\,d\phi + \gamma\,\cos\vartheta\;r\,d\phi\right] \tag{53}$$

$$F_{\gamma,r} = 2\pi\gamma L + 2\pi r\gamma\cos\vartheta \tag{54}$$

Projecting the contribution of surface tension along radial direction, we get a negative contribution (restraining the shape) for what concerns the internal profile of the droplet; and a variable contribution for the contact line. The variability of this contribution depends on the contact angle:

- For $\vartheta < 90°$, the contribution is positive (this is the case of the Figure 74).
- For $\vartheta = 90°$, the contribution is zero.
- For $\vartheta > 90°$, the contribution is negative.

Using the MATLAB routine [61] already introduced, we tested those radial balances using the theoretical values obtained from Laplace-Young equation (27).
See Figure 76.

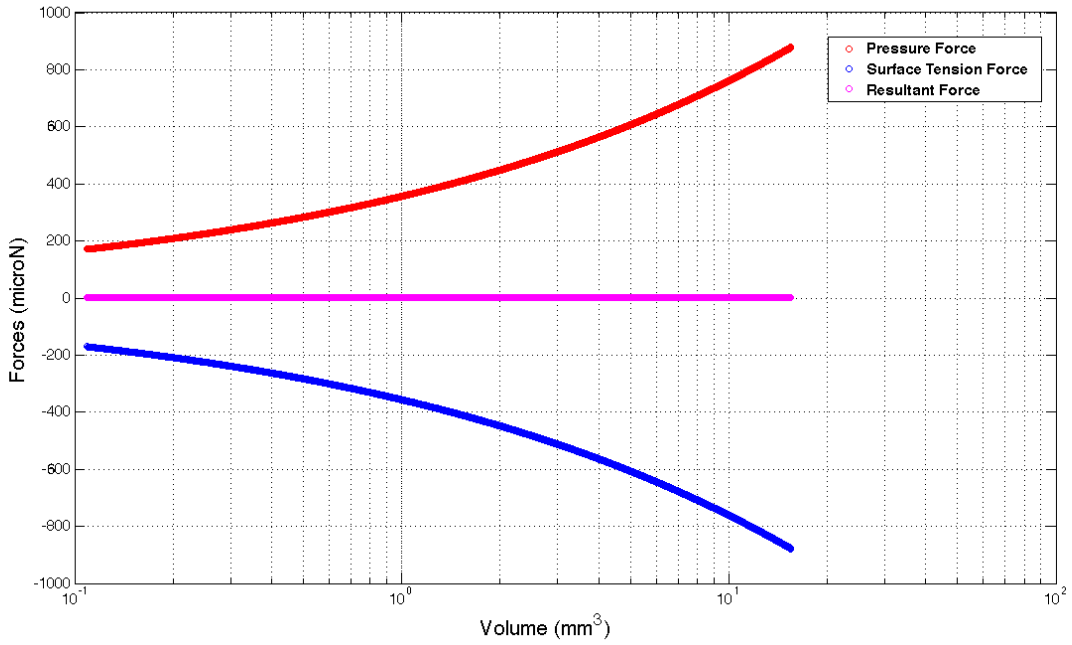

Figure 76: 1st and 2nd way radial balance verification using the profile derived by Laplace Young numerical integration [61]

For what concerns the balance during spreading, the case of 0.5 ml/min on Aluminium surface is shown in Figure 77.

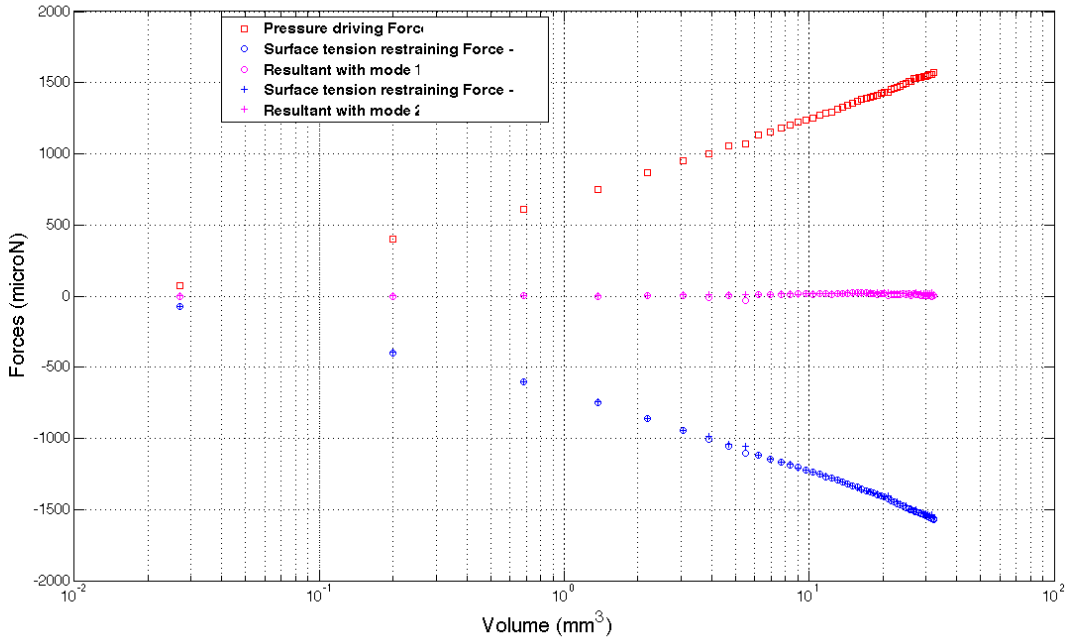

Figure 77: radial force balance application for the case of spreading droplet with calculated imposed flow rate of 0.585 ml/min. Aluminium data series.

Analysing this result, it looks as though the resultant force is balanced. This result is confirmed at the higher flow rate investigated for aluminium, see Figure 78.

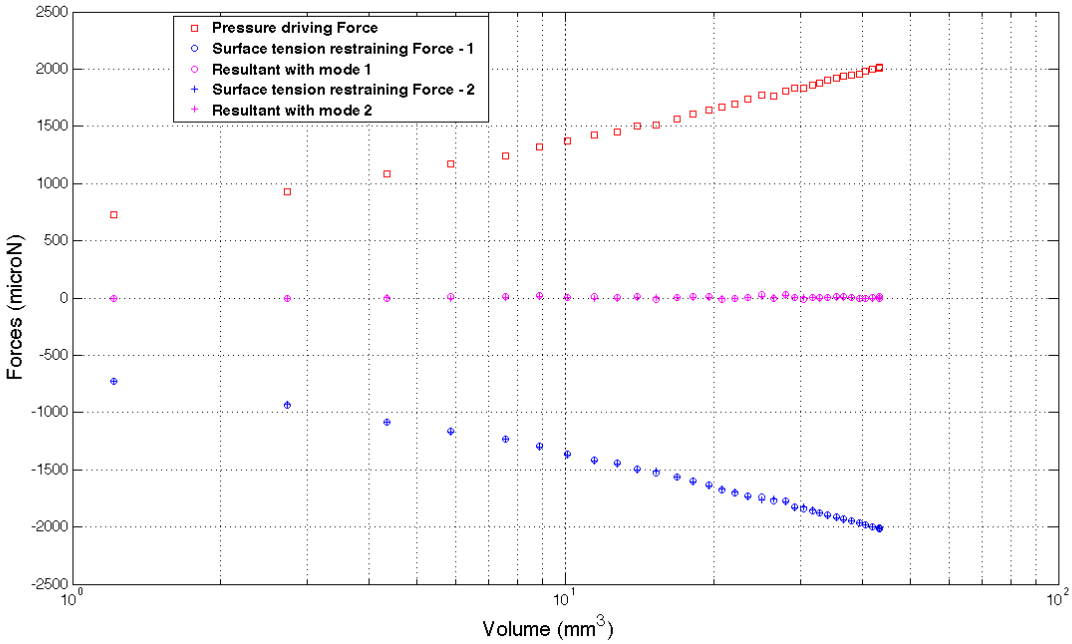

Figure 78: radial force balance application for the case of spreading droplet with calculated imposed flow rate of 1.3 ml/min. Aluminium data series.

Also in this case, the resultant radial force appears to be negligible.

However, if we further increase the volume, the resultant force appears to be no longer negligible, as shown in Figure 79.

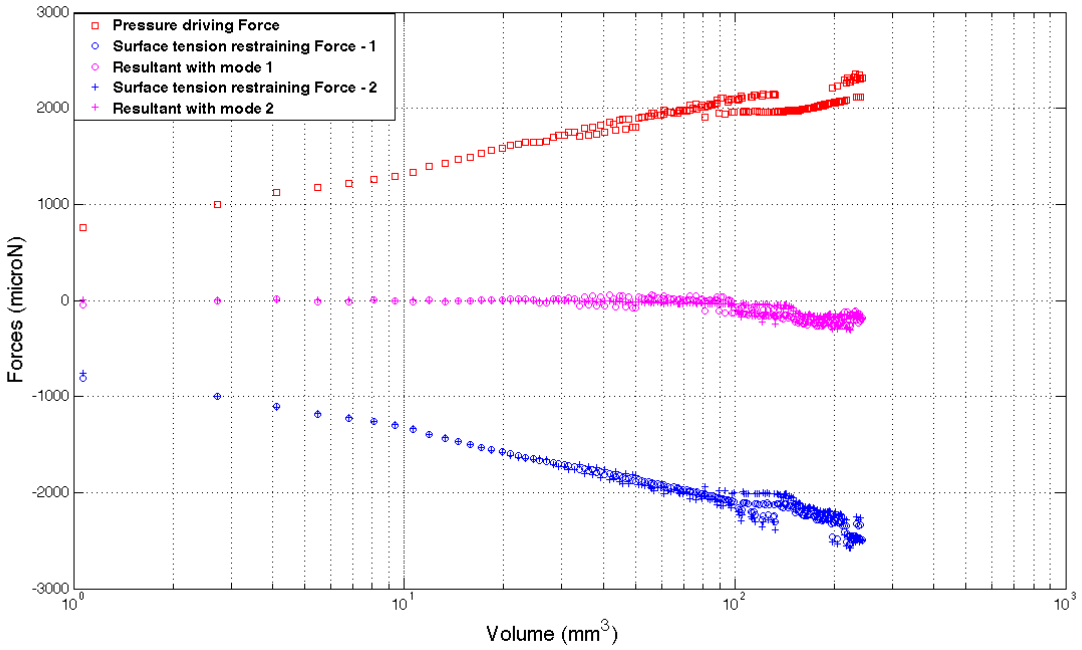

Figure 79: radial force balance application for the case of spreading droplet with imposed flow rate of 1 ml/min. Brass data series.

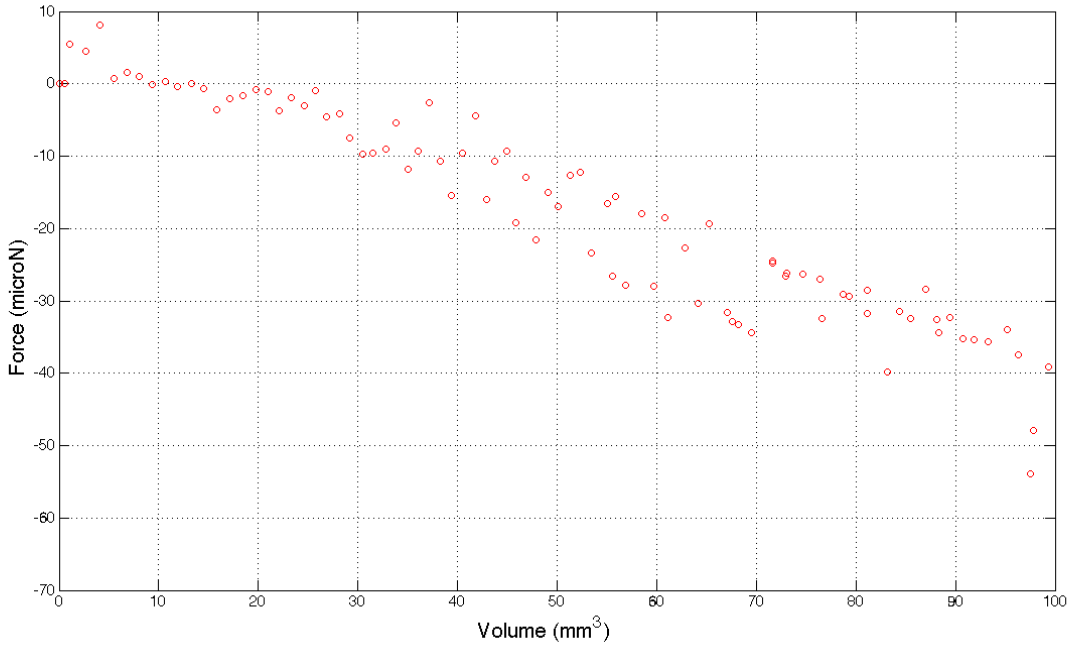

Figure 80: Radial resultant force for the case of spreading droplet. Q = 1ml/min. Brass data series.

Concluding this paragraph on the radial momentum balance, it seems that the spreading process can be divided in three phases:

- A first instant, very short in terms of time and difficult to investigate with the frame used herein (15.6 fps), where the dynamic evolution of the drop is completely driven by the force due to liquid injection.

- A second stage, much longer than the first part, which is the focus of our analysis, during which the droplet seems to be in static equilibrium, with just a change in its boundary conditions. Equilibrium is achieved in the sense that forces (both radial and vertical) are balanced.

- A third stage, where the equilibrium is altered and the resultant spreading velocity, continuously becomes smaller due to the fact that the volume has increased. See the resultant radial force resulting in Figure 79 and in Figure 80.

10 Energy balance

Moving forward in the understanding of the phenomena involved in the general process of spreading and with the aim to understand the relative relevance of these phenomena, an overall energy balance is considered.

Erickson et al. [68] found the expressions of the contribution of every phenomenon to the energy balance for the spreading case where the primary motive force is hydrodynamic. From this assumption, they derived a non-linear first order ordinary differential equation, which they solved with a fourth order Runge-Kutta technique.
To obtain this differential equation they need to make the approximation of spherical cap and to consider the dynamic contact angle as constant.
In the work here proposed, we avoided this approximation and we replaced the terms obtained with the spherical cap approximation with experimental values obtained by image processing of our tests.

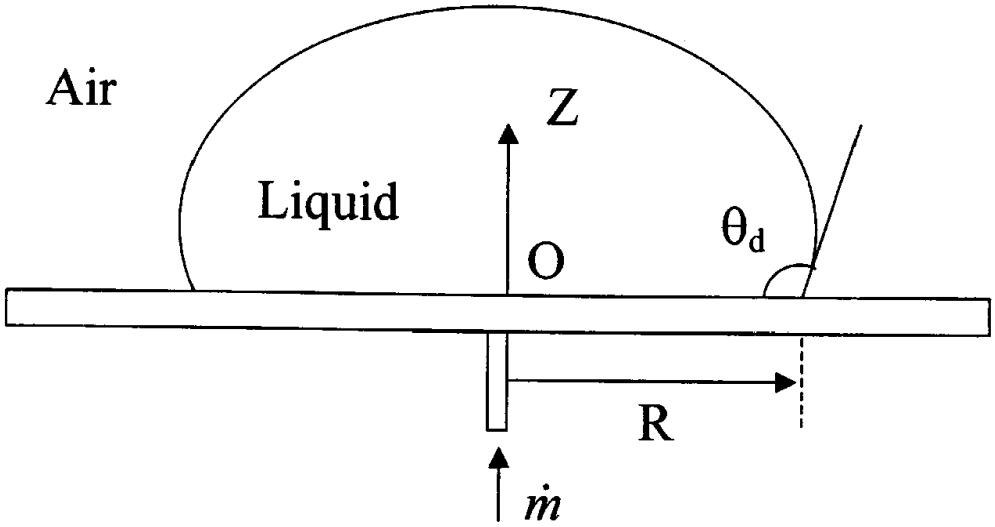

Figure 81: experiments schematics, figure from [68]

The phenomena and their contribution to the change in the energy of the drop are listed below:

- Inlet contribution; this term is mainly due to the pressure developed by the injection system, the inlet velocity and by the pressure inside the drop. It will be labelled as P_{inlet}.

$$P_{inlet} = \frac{dm}{dt}\left[u(T_0) + \frac{p_{base}}{\rho} + \frac{v^2}{2}\right] \tag{55}$$

- Internal energy of the system; this term is referred as the internal energy statically determined as a function of the temperature only. It will be labelled as P_{sys}.

$$P_{sys} = \frac{dm}{dt}u(T_0) \tag{56}$$

This term should account also for $m\frac{du}{dt}$, which is negligible since the internal energy depends only on pressure and temperature, who are not expected to vary.

- Surface potential energy; this term is very effective, it is due to the surface tension energy of the shape and depends on the interface area and the contact area. It will be labelled as P_{surf}.

$$\begin{cases} P_{surf} = (\gamma_{sl} - \gamma_{sv})\dfrac{dA_{sl}}{dt} + \gamma_{lv}\dfrac{dA_{lv}}{dt} \\ \gamma_{lv}cos(\vartheta_{eq}) = \gamma_{sl} - \gamma_{sv} \end{cases} \tag{57}$$

- Gravitational potential energy; this term is due to the height of the barycentre, and its growth. It will be labelled as P_g.

$$P_g = g\left[m\frac{dz}{dt} + z\frac{dm}{dt}\right] \tag{58}$$

- Work at boundaries; this term is due to the work done by pressure in displacing the interface. It will be addressed as P_{bound}.

$$P_{bound} = \frac{dm}{dt}\frac{p_{atm}}{\rho} \tag{59}$$

- Viscous dissipation work; this term is due to the dissipative losses due to the velocity of the fluid and viscous forces. It will be addressed as P_{visc}.

$$\begin{cases} P_{visc} = 6\pi ln(\varepsilon^{-1})\dfrac{R}{\theta_d}\left(\dfrac{dR}{dt}\right)^2 \\ \varepsilon = {}^{L_\delta}/_{L} = microscopic\ length\ /\ macroscopic\ length \end{cases} \tag{60}$$

Finally, the overall energy balance reads as follows:

$$P_{inlet} = P_{sys} + P_{surf} + P_g + P_{bound} + P_{visc} \tag{61}$$

A comparison of the order of magnitude of the different terms revealed that the most influent phenomenon in drop spreading is the work required to increase the surface area.
For high velocity rates this model is not self-determined, but needs experimental curve fitting factors to evaluate the term P_{visc}. Fortunately, since this term is always very low, in most cases it can be neglected.
Furthermore, since L_δ is usually between 1μm and 5μm and L is of the order of magnitude of the contact radius (1mm - 3mm), ε is between $0.3\cdot10^{-3}$ and $5\cdot10^{-3}$. So, the range of variation of $\ln(\varepsilon^{-1})$

is not so large: typically between 5.7 and 8.5. In the subsequent graphs, an average value will be taken.

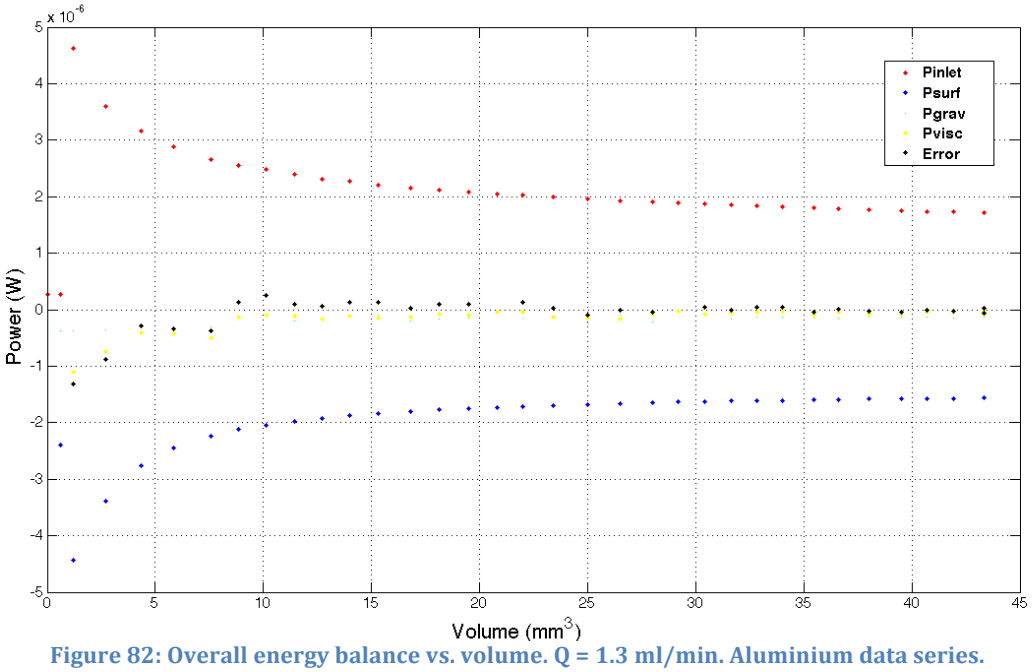

Figure 82: Overall energy balance vs. volume. Q = 1.3 ml/min. Aluminium data series.

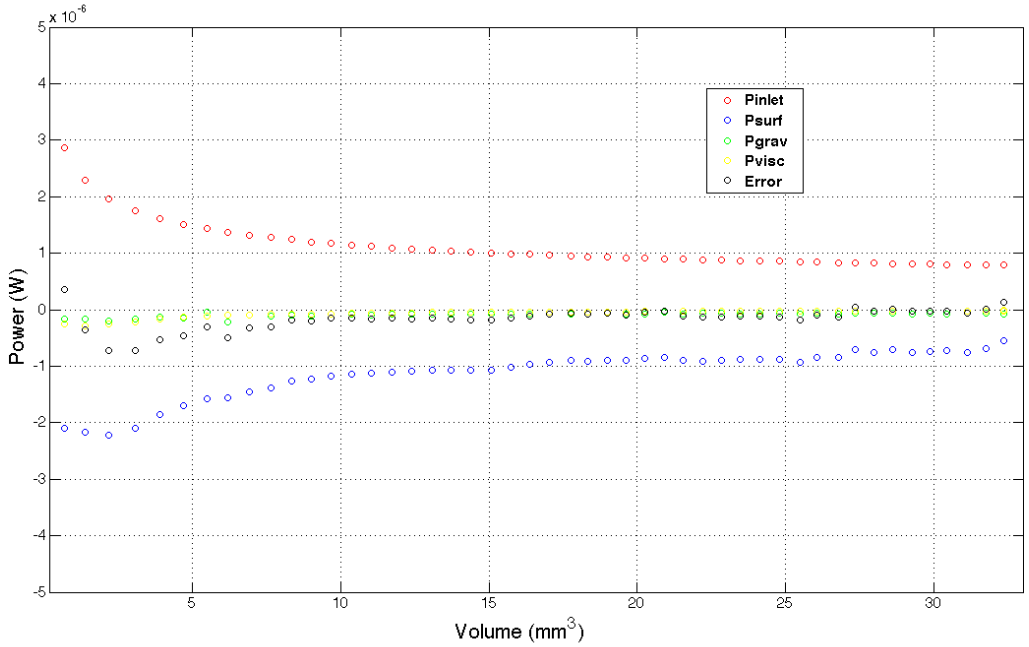

Figure 83: Overall energy balance vs. volume. Q = 0.585 ml/min. Aluminium data series.

In general, the balance proposed by Erickson [68] is satisfied.
This means that most of the inlet power isn't consumed by viscous, but is spent in the creation, during the first instants, and the growing of the both interfaces: solid-liquid and liquid-air, with their respective surface tensions.
This result, found numerically by Erickson on spherical cap droplets, has been verified experimentally on the same geometry, for droplets far from the spherical cap approximation.

11 Comparison of different material behaviours

Many studies have been found in order to understand the conditions for the spreading and the behaviour of the viscous dissipation close to the contact line. Many authors tried to couple the triple line velocity just with the contact angle. They mainly studied various fluids in capillary tubes ([17], [18], [19], [20], [22], [23])
The application of these results on droplets is still in discussion, while many researchers are applying these correlations to the study of droplet impingement and the development of their numerical models ([46], [47], [48], [49], [50]).
This simple physics experiment is usually combined with thermal exchange ([21], [23]).
So, according to Blake [29] and Shikhmurzaev [39], the next comparison reveals that the complexity of the triple line movement has not to be attributed to the kind of the material the surface is made of, but on the details of the flow inside the droplet.

To compare the behaviour of the different surfaces with respect to contact angle and triple line velocity, we will move in two ways:

- A qualitative approach to determine with graphs and plots if surfaces behave in the same way or not.

- A quantitative approach to evaluate which are the quantities characterizing the two most important fittings discussed in Chapter 2.

Insight in the least squares curve fitting theories

Fitting most of the data to find the parameters necessary in the Hydrodynamic Theory (Eq. 16) and in the Molecular Kinetic Theory (Eq. 18), we found, for advancing data, curves like the one shown in Figure 84.
Results of the relevant parameters for fitting data in Figure 84 are reported in Table 8.

As can be noted, the value of $ln(L/L_m)$ has no physical meaning: L is usually associated in literature to the capillary length c of Eq. 34, which for water is 2.7mm [30], and L_m seems to be too low, much smaller than the order of the sub-molecular level.

As Ranabothu [30] found in his study, hydrodynamic model doesn't fit well the dynamic contact angles of water and other simple fluids. Even if the equilibrium contact angle from the fitting is reasonably close to the value he measured (which is also the case of the present study), the slip length (L_m) value, in the order of sub-atomic dimensions, is not comparable to the molecular dimensions and not physically meaningful.

Also Hayes & Ralston [33] found slip length (L_m) values "significantly smaller than the molecular dimensions" for both the advancing and receding cases. The highest value found in this work is reported in Table 12.

Bayer & Megaridis [28] subdivided their analysis on impinging droplets in a "kinematic stage" and a "final stage" with respect to the importance of the kinetic energy of the droplet.
What is important to say is that they applied the Hydrodynamic Theory to both stages mentioned above separately, finding a variation of L_m, which in the first stage was around 10^{-11} m. They found value of the slip length of the order of 10^{-15} m in the final stage of their analysis, where the capillary

number ($Ca \approx 10^{-2}$) is closer to the one investigated in this work ($Ca \approx 10^{-5}$). Demonstrating that as the Capillary number decreases, also the slip length does.
According to [28], the hydrodynamic theory performed well during (kinematic) fast spreading, in which solid/liquid interactions are weak; while application of the molecular kinetic theory yields physically reasonable parameters, which, however, vary with impact conditions.

The same considerations are applicable for the case of receding droplets.

Figure 85 shows the experimental results for both molecular kinetic and hydrodynamic fitting, while Table 9 shows the parameters found in the fitting of its data. As already said, hydrodynamic theory is completely far from predicting the behaviour of such slow velocity fields, and is plotted just for completeness. However, there are cases where hydrodynamic seems to act as well as molecular kinetic, as reported in Figure 86.
Results in terms of slip length are always not physically meaningful.
In any case, the adherence of the microscopic contact angle resulting from hydrodynamic fitting with the static contact angle used in molecular kinetic fitting is always quite good.

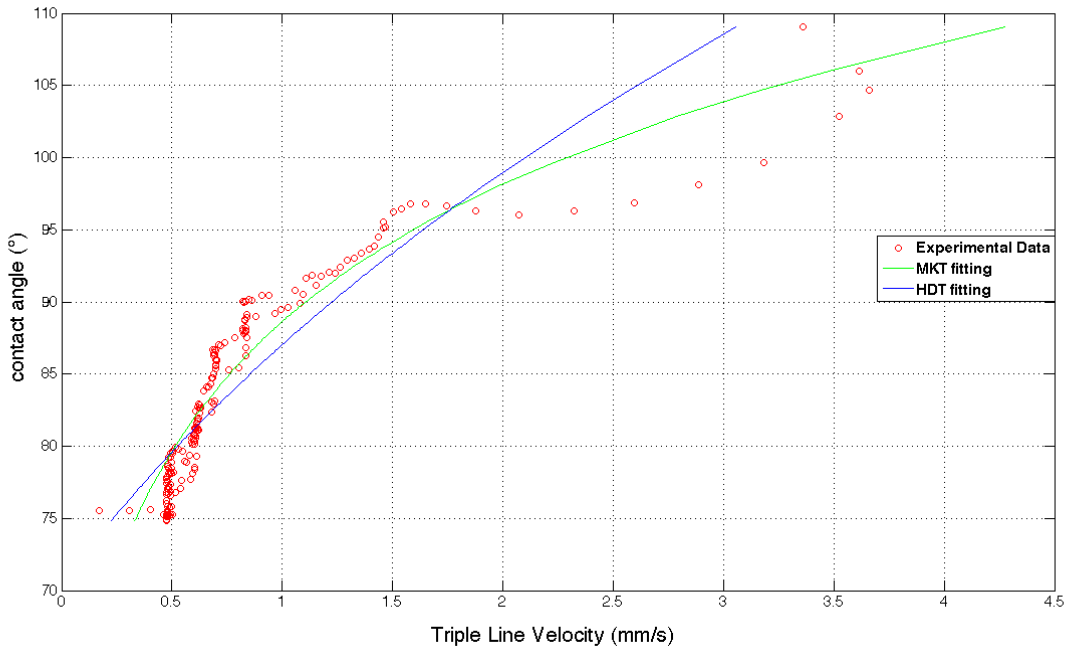

Figure 84: Comparison of the two most common fitting found in literature with the experimental data. Q = 1.05 ml/min. Brass data series.

Parameters	θ_s (°)	θ_m (°)	$ln(L/L_m)$	λ (nm)	k_w (s^{-1})
Brass -1ml/min	65	70.4	1.3×10^4	0.68	2.14×10^5

Table 8: Parameters found suitable for fitting experimental data in Figure 84

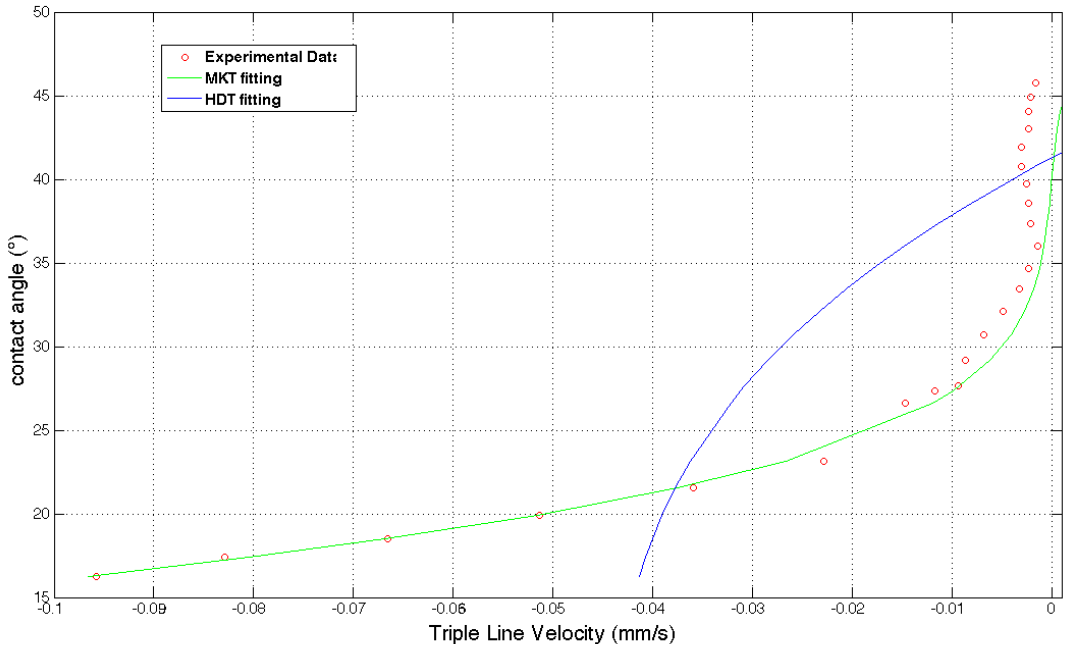

Figure 85: Comparison of the two most common fitting found in literature with the experimental data. Q = -0.005 ml/min. Aluminium data series.

Parameters	θ_s (°)	θ_m (°)	$ln(L/L_m)$	λ (nm)	k_w (s^{-1})
Aluminium – - 0.01 ml/min	40	41.27	6.79×10^4	1.88	110.28

Table 9: Parameters found suitable for fitting experimental data in Figure 85

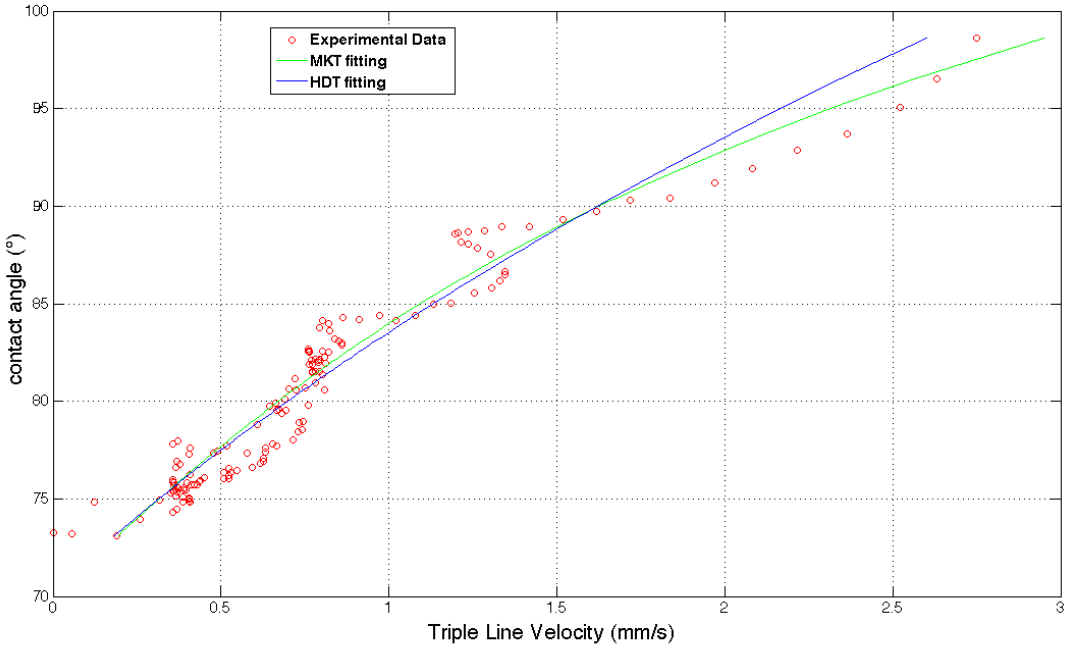

Figure 86: Adequacy of Hydrodynamic theory in fitting fast spreading droplets (Brass, 1.3 ml/min)

Insight in the wetting properties of the materials tested

Wetting properties of the material can be expressed in function of the static contact angle. As already said in Chapter 2 large contact angles express weak interaction between fluid and solid phases, while small contact angles express strong interactions.
Moving from Eq. 3:

$$\frac{\gamma_{SV} - \gamma_{SL}}{\gamma_{LV}} = \cos\theta$$

So, the static contact angle is a measure of the relative importance of surface tensions.
If it is small, this is the case of ethyl alchool on stainless steel ($\gamma_{LV} = 0.022\ N/m$), a droplet is reported in Figure 87. In this case, the relative importance of the numerator compared to the denominator is high. In the case just reported, the contact angle is around 25°, and the ratio between surface tensions is 90%. This is typical for low surface tension fluids, like ethyl alchool, HFE7100 and FC-72. Of course, surface tension is not the only responsible for the contact angle behavior, but has its role.

The couples used in this work are all partially wetting, as can be deduced from the static contact angles measured for all the tested surfaces in Figure 88.

Figure 87: ethyl alcohol droplet at rest on stainless steel

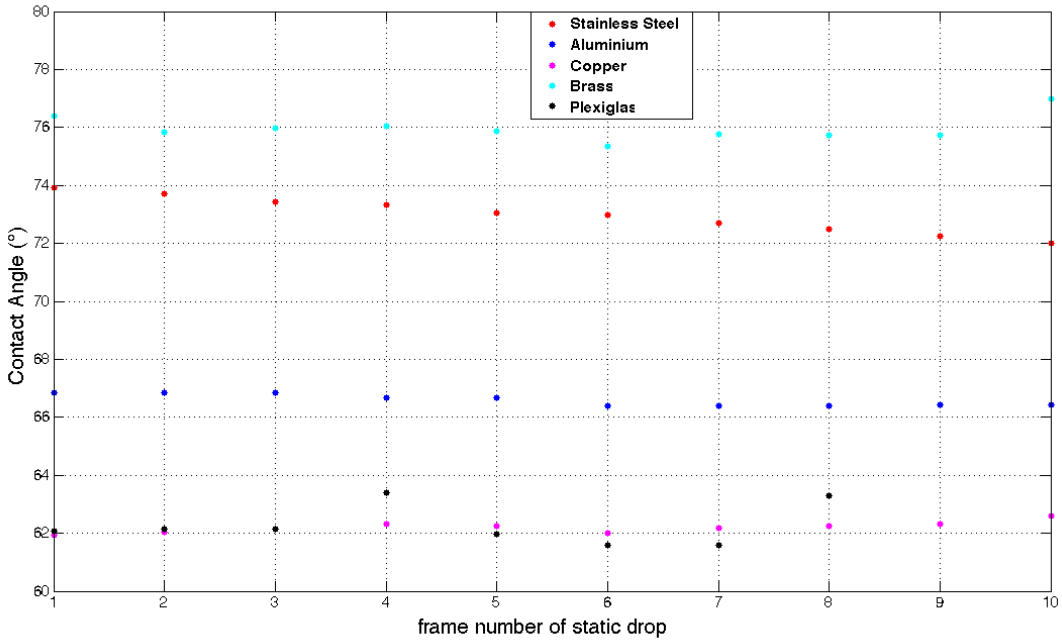

Figure 88: Static contact angles calculated from 10 different images of static drops.

Comparison of surfaces (qualitative – 1st way

Analysing all the surfaces, the results reported in Figures 91-95 were obtained.
It has to be said that results are plotted as they came out from post processing, without any intervention of filtering.
All plots report the measured contact angle vs. triple line velocity. All of them follow the same legend, reported here:

Advancing cases:	Receding cases:
• 0.005 ml/min	• - 0.005 ml/min
• 0.05 ml/min	• - 0.05 ml/min
• 0.1 ml/min	• - 0.01 ml/min
• 0.5 ml/min	
• 1 ml/min	

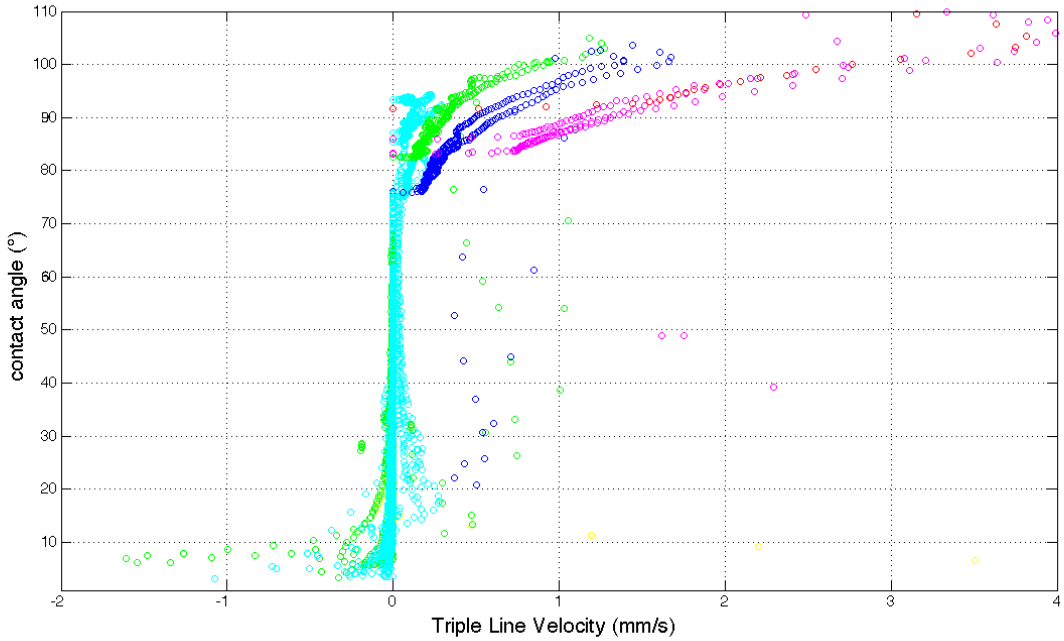

Figure 89: Aluminium, advancing and receding

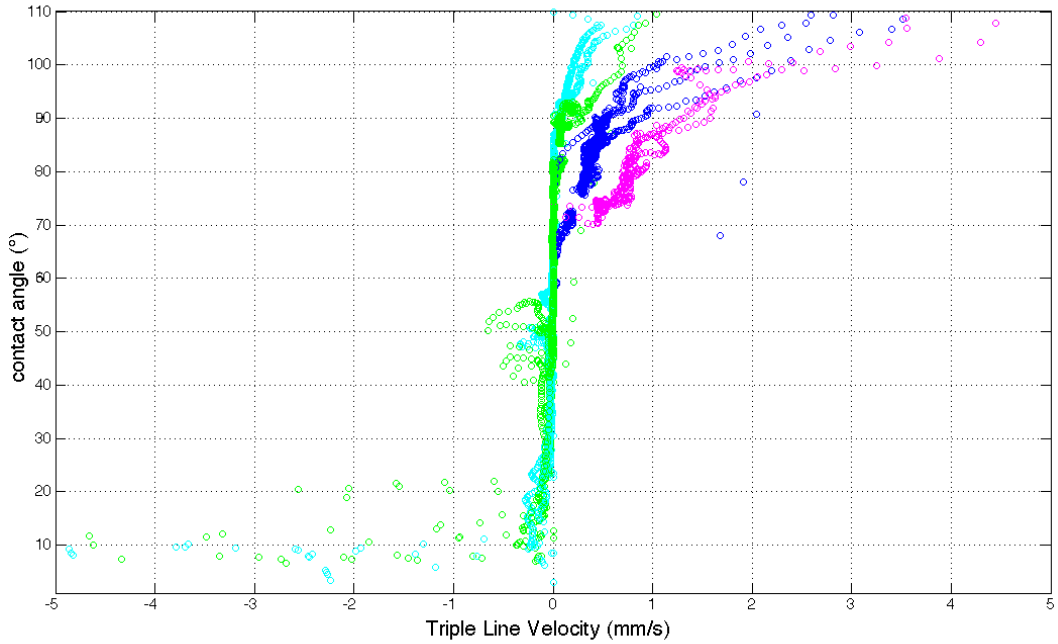

Figure 90: Brass and Brass-2nd, advancing and receding

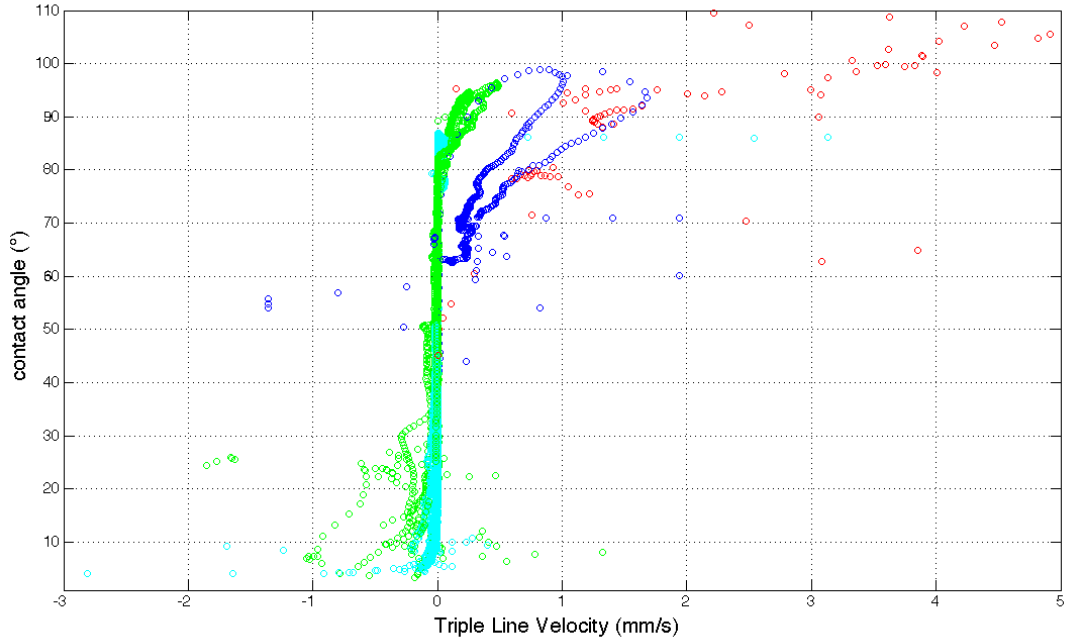

Figure 91: Copper, advancing and receding

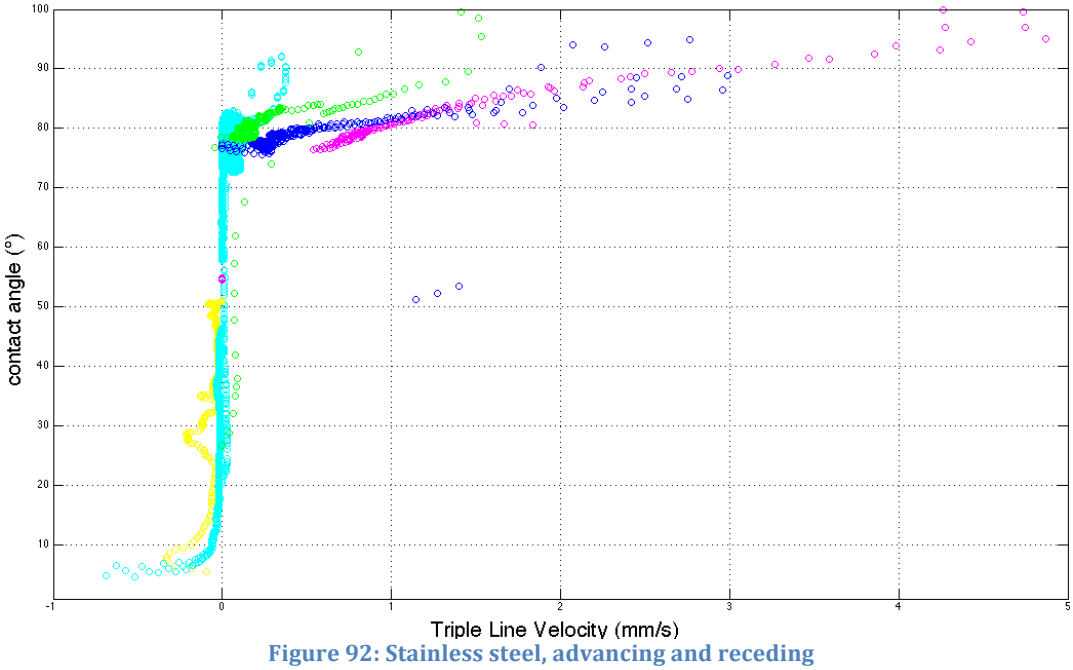

Figure 92: Stainless steel, advancing and receding

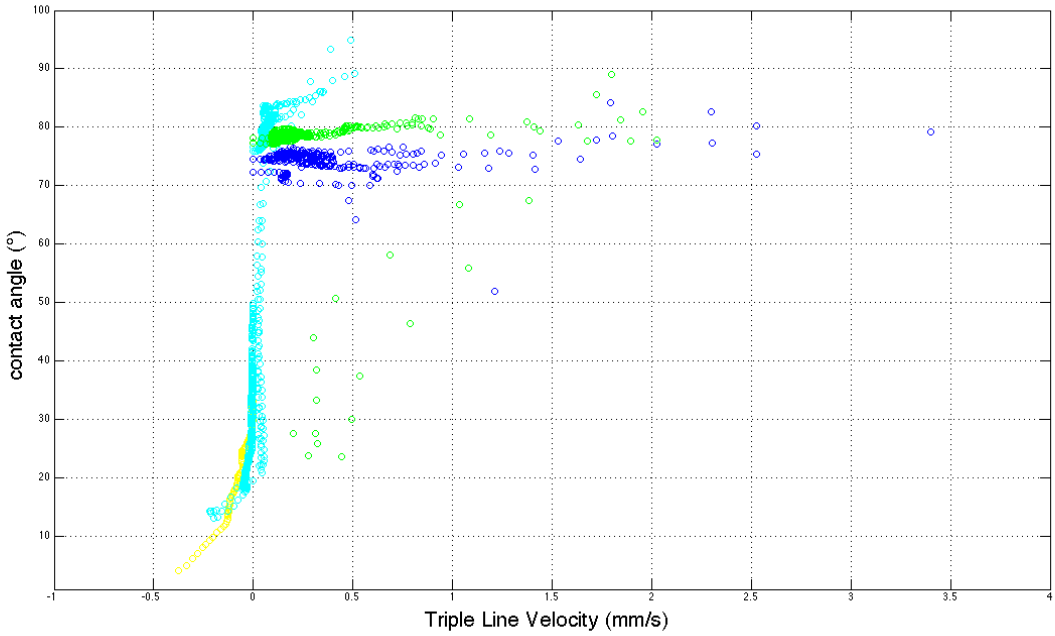

Figure 93: Plexiglas, advancing and receding

To compare different surfaces, in order to have a clearer vision of similitudes between behaviours, we will compare the data for the same nominal flow rate.

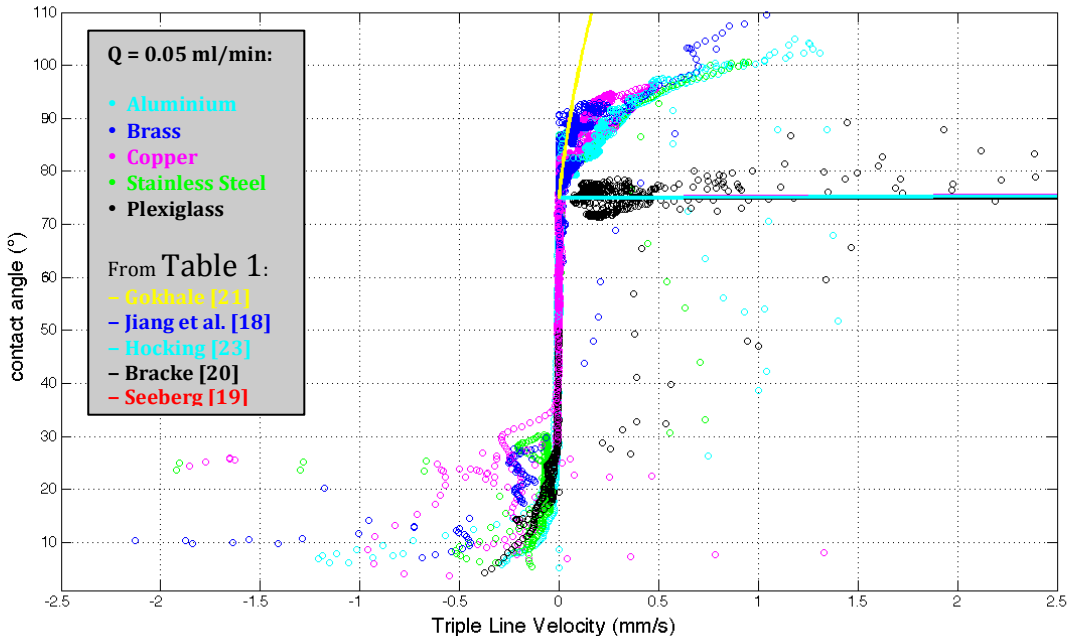

Figure 94: Qualitative comparison of different materials, with the same flow rate in advancing and receding. Lines are the correlations reported in Section 2: State of the art2 , Table 1

Figure 94 allows us to say that what may act as difference in spreading behaviour, better than the kind of surface, is the nature of the surface: we should distinguish between metallic surfaces and non-metallic surfaces.

Metallic surfaces seem to behave in the same way, while non-metallic surfaces seems to have a different behaviour from the others. In particular, Plexiglas surface reveals to be suitable for the approximation of constant advancing angles for flow rates over 0.05 ml/min (see blue and red spots in Figure 93). The value of this constant advancing contact angle in our analysis seems to depend on the magnitude of the flow rate, but we expect that it is constant over a certain value.

Of course, there is a slightly difference between metallic surfaces which cannot be caught from plot in Figure 94, but will be better analysed in the quantitative way of comparing surfaces. Furthermore, the uncertainty can be due also to the different values of the real flow rate, which can vary with an error band of around 25% from surface to surface and from the nominal value.

As shown in the previous figures, most of the correlations are not applicable to the cases here reported, with the exception of the highest flow rates of the Plexiglas's case. Those correlations were derived from experiments taken at higher velocities, here they were extrapolated. The only correlation which seems to catch data of the lowest flow rate (0.005 ml/min) is the one derived by Gokhale et al. [21] which was built with a polynomial regression of small droplets advancing and receding for condensation and evaporation phenomena, thus the velocity was very small and even smaller of the one analysed in the present work.
In any case, as already mentioned, the value of the initial advancing contact angle, the angle at which spreading starts decreasing with increasing the flow rate, thus leading to different starting point for correlations in Table 1.

The smaller flow rate reveals graphs like the one shown in Figure 94, while higher flow rates reduce the gap between metallic surfaces and the Plexiglas one.
From this point, rather than showing plots in order to compare experimental data, we will compare directly the two fitting theories introduced.

Some considerations can be done also for the receding case, even if the dispersion is very high for some tests, not in terms of velocity, for which the calculation is quite accurate thanks to high scale factor, but in terms of contact angle, which becomes very small: order of some degrees (from 2° to less than 10°); accuracy is quite low for those contact angles.
Many tests have been carried on for the receding case with every surface. The number of tests is higher in this condition since sometimes, and in random situations, pinning occurred.
It seemed it could be avoided using very low flow rates (-0.01 ml/min maximum).
The problem was common for metallic surfaces without any assessed reproducibility between surfaces, while for Plexiglas it is much more unlikely to happen.

For receding, we can say that it seems that there was no sensible difference between surfaces and flow rates, as can be inferred from the fitting values shown in the next section.

Comparison of surfaces (quantitative – 2nd way)

The qualitative comparison of surfaces passes through a wide application of molecular kinetic and hydrodynamic fittings. The parameters to compare will be the fitting parameters which have to be compared also with values from literature resumed in Table 2, Table 3, Table 4 and Table 5 of section 2 .

$Q_{nominal}$ [ml/min]	$Q_{calculated}$ [ml/min]	θ_s (°)	λ (nm)	k_w (s^{-1})	θ_m (°)	$ln(L/L_m)$
0.005	0.007	68	0.975	6.618×10^3	81.7	0
0.05	0.069	68	0.835	4.297×10^4	74.9	0
0.1	0.099	68	0.683	2.384×10^5	71.2	0
0.5	0.568	68	0.591	8.264×10^5	70.46	0
1	1.107	68	0.805	1.800×10^5	86	0
- 0.01	- 0.007	40	1.888	110.28	41.27	0
-0.005	-0.004	25	2.96	48.49	26.95	0

Table 10: Aluminium fitting parameters for every flow rate investigated. Non-physical values for the last column.

$Q_{nominal}$ [ml/min]	$Q_{calculated}$ [ml/min]	θ_s (°)	λ (nm)	k_w (s^{-1})	θ_m (°)	$ln(L/L_m)$
0.005	0.007	75	0.947	6.4146×10^4	75.3	0
0.05	0.059	75	1.246	4.8172×10^4	78.33	0
0.1	0.121	75	0.53	2.984×10^6	75.83	0
0.5	0.5225	75	0.613	2.4472×10^6	74.19	0
-0.05	-0.0461	40	1.59	2.6766×10^4	40	0
-0.01	-0.007	45	1.7	163.64	45.14	0
-0.005	-0.004	25	2.97	78.42	27.52	0

Table 11: Stainless steel fitting parameters for every flow rate investigated. Non-physical values for the last column.

$Q_{nominal}$ [ml/min]	$Q_{calculated}$ [ml/min]	θ_s (°)	λ (nm)	k_w (s^{-1})	θ_m (°)	$ln(L/L_m)$
0.005	0.0049	70	0.687	5.365×10^4	70.32	0
0.05	0.058	70	0.9235	1.097×10^4	74.32	0
0.1	0.11	70	0.535	2.232×10^5	66.37	0
1	0.88	70	0.465	2.2475×10^6	60.2	0
-0.01	0.0065	40	1.933	147.86	39.34	0
-0.05	-0.0614	40	2.38	108.1	37.91	8.5×10^{-138}
-0.005	-0.0057	40	1.436	2.07×10^3	42.15	0

Table 12: Copper fitting parameters for every flow rate investigated.

$Q_{nominal}$ [ml/min]	$Q_{calculated}$ [ml/min]	θ_s (°)	λ (nm)	k_w (s^{-1})	θ_m (°)	$ln(L/L_m)$
0.05	0.024	70	0.785	1.59×10^4	85	0
0.1	0.05	70	0.803	3.25×10^4	79.48	0
0.5	0.443	70	0.663	2.368×10^5	72.2	0
1	1.159	70	0.6198	4.9637×10^5	69.9	0
- 0.01	- 0.008	40	1.576	100.5	42.75	0
-0.005	-0.0044	25	2.481	67.3	27.26	0

Table 13: Brass fitting parameters for every flow rate investigated. Non-physical values for the last column.

$Q_{nominal}$ [ml/min]	$Q_{calculated}$ [ml/min]	θ_s (°)	λ (nm)	k_w (s^{-1})	θ_m (°)	$ln(L/L_m)$
0.005	0.005	75	1.25	1.289×10^4	75.7	0
0.05	0.0544	75	1.2	1.487×10^5	76.59	0
0.1	0.11	75	0.18	1.985×10^8	74.09	0
-0.01	-0.0114	30	1.66	7.09×10^3	27.76	0
-0.005	-0.0055	30	1.837	2.58×10^3	28.79	0

Table 14: Plexiglas fitting parameters for every flow rate investigated. Non-physical values for the last column.

There is a difficulty in comparing tables with those present in section 2, since for the latter no information are provided about the flow inside the droplet. Characteristics of the flow inside the drop should allow us to compare different experiments of moving interface.

Anyway, we can compare again data present in table. Many authors [30] suggested a variation of the term k_w with respect to surface tension, but since we focused our attention always on the same fluid, we noted that the variability of this term seems to be due also to characteristics of the flow field, as can be assessed in Figure 95.

Same consideration can be done for the term λ, which seems to vary in function of the flow rate. See Figure 96.

Just as a remind: k_w is the equilibrium frequency of molecular displacement and λ is the length of each molecular displacement.
High or low values of k_w imply, respectively, weak or strong dependence of the contact angle on velocity of the triple line [28].

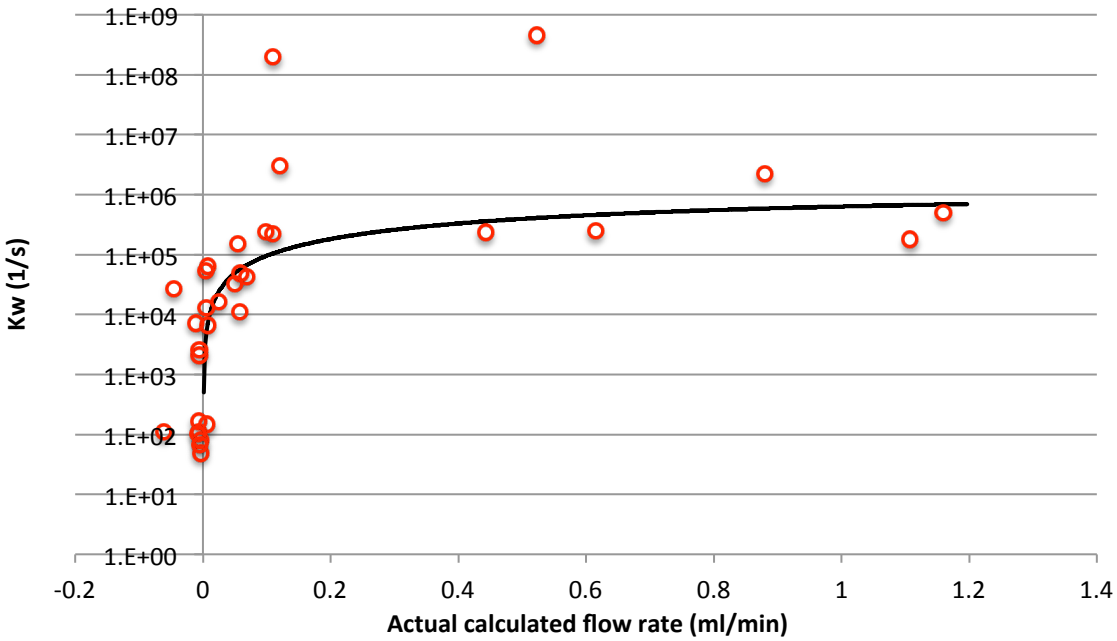

Figure 95: behaviour of *kw* as function of the flow rate and tendency line

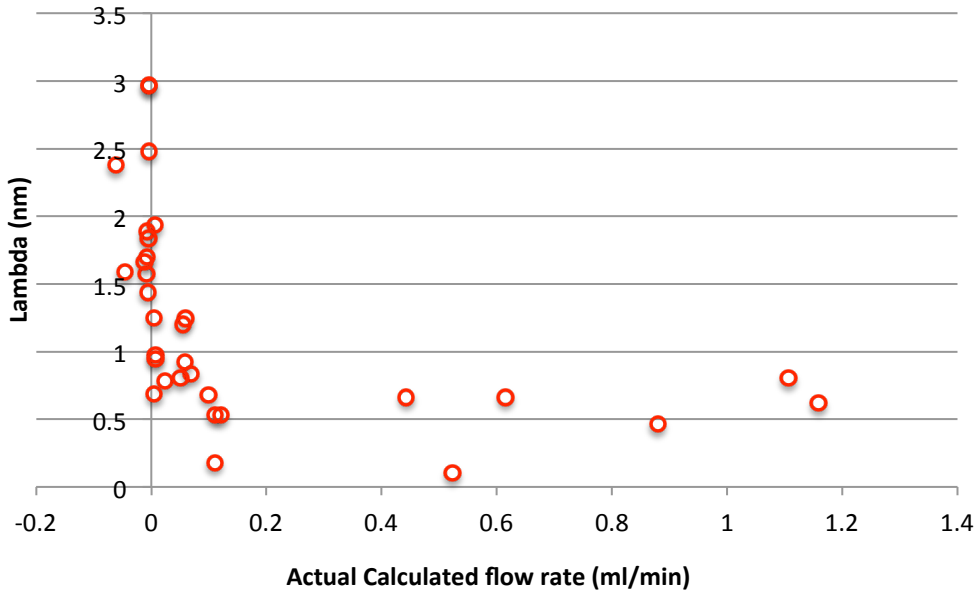

Figure 96: behaviour of λ as function of the flow rate

12 Effects of roughness

To understand the effects of surface roughness on the dynamic behaviour of contact angle, first of all we have to understand how it affects wettability.
According to Kubiak et al. [70] and to Wenzel [69]:

$$\cos(\theta_A) = r \cdot \cos(\theta) \tag{62}$$

Where θ_A is an apparent contact angle and r is the ratio of the real rough surface area to the projected perfectly smooth surface and θ is the contact angle corresponding to the ideal surface.
r is proportional to the extension of surface area due to roughness.
In Figure 97 this law is fulfilled: blue spots are the static contact angles of sessile droplets on the surface of stainless steel mirror polished; red spots represents the static contact angle on the surface of stainless steel polished with P40 paper. The result of this last polishing is an average roughness parameter $R_a = 0.682$ μm (for mirror polishing was: $R_a \leq 0.015$ μm).

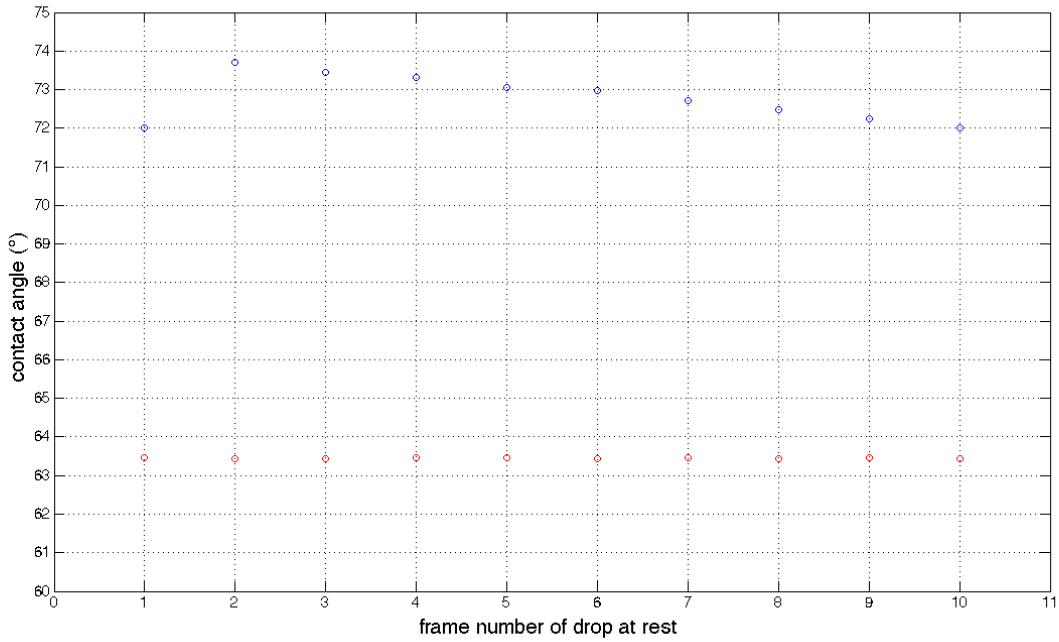

Figure 97: Static contact angle of drops at rest. In blue, Stainless steel mirror polishing. In red stainless steel P40.

To see which is the effect of this roughness over the spreading dynamic contact angle, several tests were performed.

A note has to mentioned, since it will be difficult to catch from graphs: the contact line no more moves in a continuous way, but jumps from a point to another. This behaviour has been already experienced by Jansons [71].

Another thing noted during the experiment was the difficulty of receding: almost all the tests ended with pinning, just one of the tests done succeeded in moving, and very quickly, the triple line: velocity magnitude was in the order of 20 mm/s while the contact angle is 3.4°. Those points are out of scale in Figure 98.

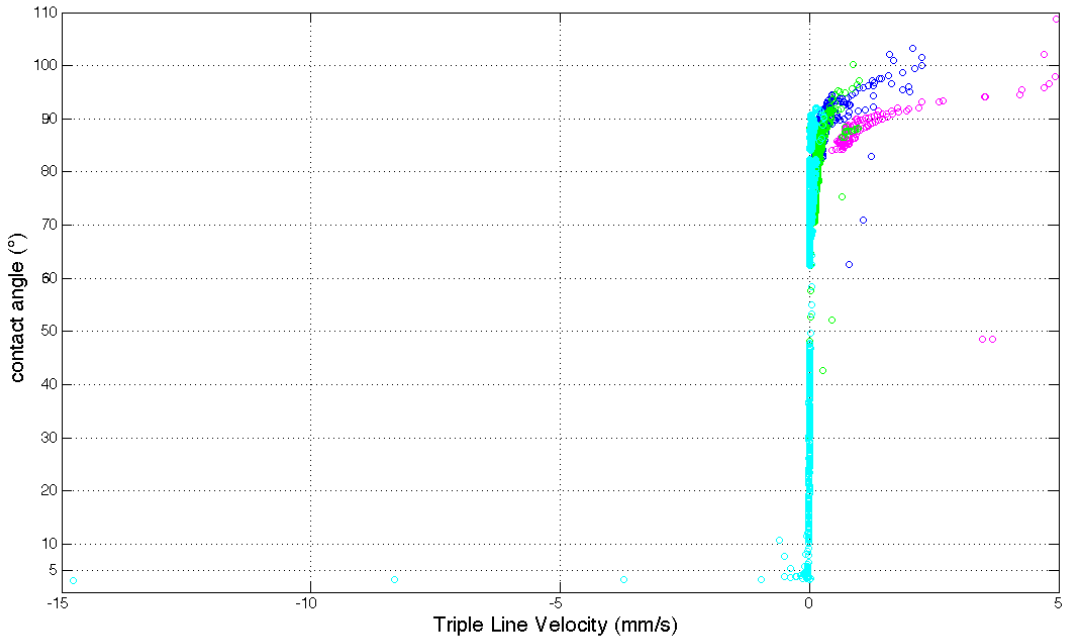

Figure 98: P40 advancing and receding

For the comparison with the same material mirror polishing, we will operate as before: a first qualitative approach (see Figure 99) and a second quantitative approach (see Table 15).

For what concerns Figure 99, we have to say that the behaviour is exactly the same as the stainless steel mirror polishing, remarking in this way its difference from the non-metallic surface seen before.
The only difference with respect to the behaviour of less rough stainless steel surface is that advancing starts at a higher contact angle (this happens for every flow rate) and receding starts at a lower contact angle; in same cases too much lower: the value we got was just of 3°.

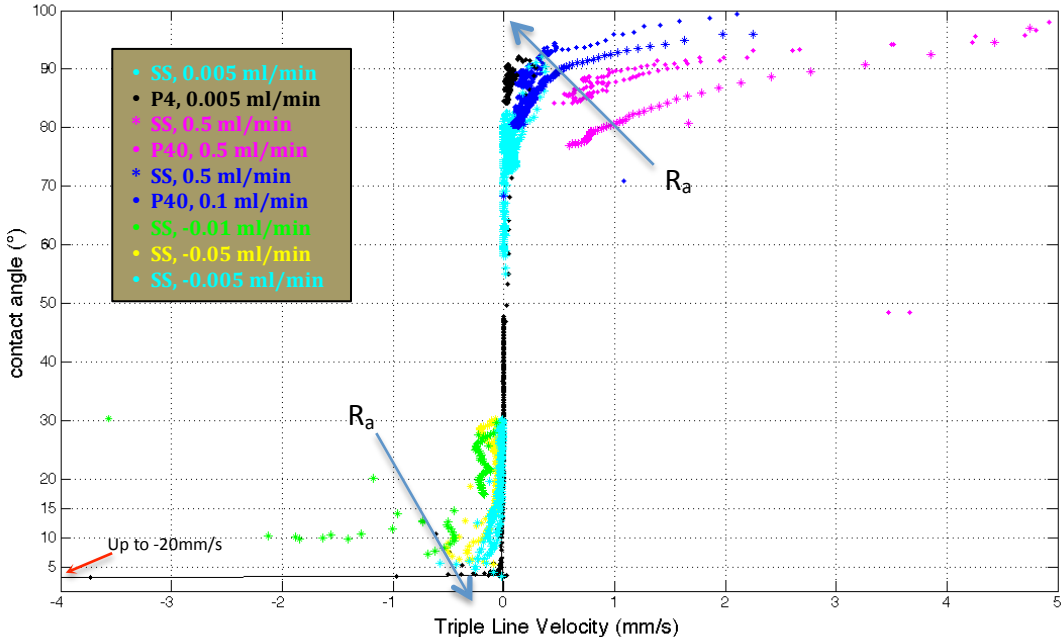

Figure 99: Stainless steel advancing and receding comparison with respect to roughness

In conclusion, it seems like the main effects of surface roughness are:

- To extend the hysteresis zone: there is a much larger zone where the velocity is zero and the contact angle can vary over a wider range.
- To increase wettability of the surface.

$Q_{nominal}$ [ml/min]	$Q_{calculated}$ [ml/min]	θ_s (°)	λ (nm)	k_w (s^{-1})	θ_m (°)	$ln(L/L_m)$
0.1	0.11	65	1.08	5.548×10^3	80.34	0
0.5	0.546	65	1.125	9.64×10^3	84.81	0
0.05	0.0528	65	0.967	9.965×10^3	68.48	0
0.005	0.0050	65	0.798	3.1633×10^4	67.09	0
-0.005	-0.0051	40	1.486	181.3	42.68	0
-0.005	-0.005	3	22.035	27	-81	Inf

Table 15: P40 fitting parameters for every flow rate investigated.

Comparing values in Table 11, with the ones reported in Table 15; for the advancing cases, and for every flow rate investigated, stainless steel mirror polished has always a higher parameter k_w.
The discrepancy in their matching grows with the flow rate: they have the same order of magnitude at Q = 0. 005 ml/min; at Q = 0.5 ml/min P40 has a 2-order of magnitude lower k_w.
It means that for all the advancing cases, P40 has a greater dependence of contact angle on the velocity of the triple line.

For the receding cases, the situation is difficult: there are just few tests on P40 without pinning, both are reported in Table 15, one is higher than the stainless steel mirror polishing case, one is lower. We can just confirm that, for the rough surface, the contact angle is lower and the triple line velocity, and so the interface, jump.

13 Conclusions, acknowledgement and future prospect

In this study, a comprehensive analysis of spreading droplets has been performed starting from its geometrical analysis.

The experimental setup used in this investigation was very simple. Further development should include just a more accurate analysis of the first instants of droplets spreading, with a faster camera than the one used in the present work.

With the flow rate investigated herein, the droplet seems always to respect Laplace-Young equation and all the balances: vertical force balance and the two radial force balances.
From an analysis of the energetic terms of the overall energy balance, it comes out that the surface growth, and by the way, surface tension retention, is the phenomenon storing almost all the energetic contribution due to liquid injection, with a very small and negligible contribution by viscous dissipation.

Higher flow rates can obviously be performed to achieve disequilibrium in those balances and analyse better which are the conditions for the droplet to spread, but the Laplace fitting method (the one by Konduru) has to be abandoned, thus leading to high uncertainty in the calculation of contact angles.

The behaviour of the contact angle with respect to the triple line velocity seems to be more complex than expected in the past literature. Correlations between contact angle and triple line velocity failed in predicting the evolution of droplet spreading in this work.

The surface seems not to be relevant in kind, but in nature: different behaviours have been investigated looking at plastic surfaces (Plexiglas) and metallic surfaces (all the other ones).

Computational fluid dynamics and direct numerical simulation can help in understanding which is the magnitude of the flow field inside the drop: it is supposed to be very small in value, but its distribution inside the droplet is known just qualitatively.

Other experiment involving mass and heat transfer through the liquid-gas interface should be coupled with adiabatic experiments like the one presented in this work to find the effects and contribution to droplet spreading.

Further efforts should be done in investigating similitudes between droplet advancing and receding and bubble growing (liquid receding) and detachment (liquid advancing).

The experiment, named DAIE (*Droplet Analysis Injection Experiment*), has been carried on with the interest and contribution of CEA-Saclay (*Commissariat à l'Énergie Atomique*), in the figures of Dott. Matteo Bucci and Dott. Benjamin Cariteau.

This work is the final step of a path of study and knowledge about droplets and bubbles built with the help, supervision and guidance of Professor Paolo Di Marco.

References

[1] Rohsenow, W. M., and Griffith, P., 1956, "Correlation of Maximum Heat Transfer Data for Boiling of Saturated Liquids", Chem. Eng. Prog., 52, pp. 47.

[2] S.P. Liaw, V.P. Dhir, Void fraction measurements during saturated pool boiling of water on partially wetted vertical surfaces, J. Heat Transfer 29 (2008) 731–738.

[3] R.I. Vachon, G.H. Nix, G.E. Tanger, Evaluation of constants for the Rohsenow pool-boiling correlation, J. Heat Transfer 90 (1968) 239–247.

[4] Satish G. Kandlikar, "A Theoretical Model to predict Pool Boiling CHF Incorporating Effects of Contact Angle and Orientation", J. Heat Transfer 123 (2001) 1071–1079.

[5] N. Ramanujapu, V.K. Dhir, Dynamics of contact angle during growth and detachment of a vapor bubble at a single nucleation site, in: Proceedings of the 5th ASME/JSME Joint Thermal Engineering Conference, San Diego, CA, 1999, AJTE99/6277.

[6] C.P. Costello, W.J. Frea, A salient non-hydrodynamic effect on pool boiling burnout of small semi-cylindrical heaters, AIChE Chemical Engineering Progress Symposium Series, 61-57, pp. 258-268.

[7] H. T. Phan, N. Caney, P. Marty, S. Colasson, J. Gavillet, Surface wettability control by nanocoating: The effects on pool boiling heat transfer and nucleation mechanism, Int. J. Heat Mass Transfer 52 (2009) 5459-5471.

[8] I. Sher, G. Hetsroni, An analytical model for nucleate pool boiling with surfactant additives, Int. J. of Multiphase Flow 28 (2002) 699–706

[9] A. Mukherjee, S. G. Kandlikar, Numerical study of single bubbles with dynamic contact angle during nucleate pool boiling, Int. J. Heat and Mass Transfer 50 (2007) 127–138

[10] G. Son, V. K. Dhir, N. Ramanujapu, Dynamics and Heat Transfer Associated with a Single Bubble during Nucleate Boiling on a Horizontal Surface, J. Heat Transfer 121(3) (1999) 623-631

[11] A.Mukherjee, S.G. Kandlikar, Z.J. Edel, Numerical Study of bubble growth and wall heat transfer during flow boiling in a microchannel, Int. J. Heat and Mass Transfer 54 (2011) 3702-3718

[12] H. T. Phan, N. Caney, P. Marty, S. Colasson, J. Gavillet, A model to predict the effect of contact angle on the bubble departure diameter during heterogeneous boiling, Int. Communications in Heat and Mass Transfer 37 (2010) 964-969

[13] S. G. Kandlikar, M. E. Steinke, Contact Angles and interface behaviour during rapid evaporation on a heated surface, Int. Journal of Heat and Mass Transfer 45 (2002) 3771-3780

[14] S. Chandra, M. di Marzo, Y. M. Qiao, P. Tartarini, Effect of Liquid-Solid Contact Angle on Droplet Evaporation, NIST GCR 96-687; Paper 15; June 1996.

[15] L. Liao, R. Bao, Z. Liu, Compositive effects of orientation and contact angle on Critical Heat Flux in pool boiling of water, Heat and Mass Transfer (2008) 44: 1447-1453

[16] Young, T., 1805, "An essay on the cohesion of fluids," Philos. Trans. R. Soc. London 95, 65.

[17] R. L. Hoffman, "A study of the advancing interface. I. Interface shape in liquid-gas systems," J. Colloid Interface Sci. 50, 228 (1975).

[18] T.S. Jiang, S.G. Oh and J.C. Slattery. Correlation for dynamic contact angle. J. Colloid Interface Sc., 69, 1, p 74-77, 1979.

[19] J.E. Seeberg and J.C. Berg. Dynamic wetting in the low of capillary number regime. Chem. Eng. Sc., 47, p 4455-4464, 1992.

[20] M. Bracke, F. De Voeght and P.Joos. The kinetics of wetting: the dynamic contact angle, Progr. Colloid Pol. Sc., 79, p 142-149, 1989.

[21] S. J. Gokhale, J. L. Plawsky, P. C. Wayner Jr., Experimental investigation on contact angle, curvature and contact line motion in dropwise condensation and evaporation, J. of Colloid and Interface Science, 259 (2003) 354-366

[22] L. M. Hocking, "The spreading of a thin drop by gravity and capillarity," Q. J. Mech. Appl. Math. 36, 55 (1983).

[23] L. M. Hocking, On contact angles in evaporating liquids, Physics of Fluids, 7-12 (1995) 2950-2955

[24] Tanner, L. H.: The spreading of silicone oil drops on horizontal surfaces. J. Phys. D: Appl. Phys. 12 (9) 1473 (1979)

[25] T.D. Blake, J.M. Haynes, Kinetics of liquid/liquid displacement, J. Colloid. Interface Sci. 30 (1969) 421-423

[26] R. G. Cox, "The dynamics of the spreading of liquids on a solid surface. Part 1. Viscous flow". Journal of Fluid Mechanics, Vol 168, 169-194 (1986)

[27] O. V. Voinov, "Hydrodynamics of Wetting", Journal of Fluid Dynamics, Vol 11, 714 -721 (1976).

[28] I. S. Bayer & C. M. Megaridis, Contact angle dynamics in droplets impacting on flat surfaces with different wetting characteristics, J. Fluid Mech. (2006) 558 415–449

[29] T. D. Blake, The physics of moving wetting lines, Journal of Colloid and Interface Science 299 (2006) 1–13

[30] S. R. Ranabothu, Dynamic wetting: Hydrodynamic or molecular-kinetic?, MSC Thesis, Texas Tech University, August 2004.

[31] J. G. Petrov and P. G. Petrov, "Forced advancement and retraction of polar liquids on a low energy surface", Colloids and Surfaces, Vol 64, 143-149 (1992).

[32] T. D. Blake, "Wetting Kinetics- How Do W etting Lines Move?" AICHE International Symposium on the Mechanics of Thin Film Coating, New Orieans, paper la, (1988).

[33] R. A. Hayes and J. Ralston, "Forced Liquid Movement on Low Energy Surfaces", Journal of Colloid and Interface Science, Vol 159, 429-438 (1993).

[34] C: Huh, L. E. Scriven, Hydrodinamic model of steady movement of a solid/liquid/fluid contact line, J. of Colloid and interface science 35-1 (1971)

[35] Dussan, V. E. B. 1976 The moving contact line: the slip boundary condition. J. Fluid Mech. 77, 665–684.

[36] Dussan, V. E. B. & Davis, S. H. 1974 On the motion of a fluid-fluid interface along a solid surface. J. Fluid Mech. 65, 71.

[37] Kistler, S. F. 1993 Hydrodynamics of wetting. In Wettability (ed. J. C. Berg). Dekker.

[38] Ramé, E., Garoff, S. & Willson, K. R. 2005 Characterizing the microscopic physics near moving contact lines using dynamic contact angle data. Phys. Rev. E 70, 031608(1)–031608(9).

[39] Shikhmurzaev, Y. 1993 The moving contact line on a smooth solid surface. Intl J. Multiphase Flow 19, 589–600.

[40] Blake, T. D. 1993 Dynamic contact angles and wetting kinetics. In Wettability (ed. J. C. Berg), pp. 251–260. Marcel Dekker.

[41] Glasstone, S., Laidler, K. & Eyring, H. 1941 The Theory of Rate Process. McGraw–Hill.

[42] P.G. Petrov, J.G. Petrov, Langmuir 8 (1992) 1762.

[43] M.J. de Ruijter, J. De Coninck, G. Oshanin, Langmuir 15 (1999) 2209.

[44] T.D. Blake, K.J. Ruschak, in: P.M. Schweizer, S.F. Kistler (Eds.), Liquid Film Coating, Chapman & Hall, London, 1997, p. 63.

[45] J.G. Petrov, J. Ralston, M. Schneemilch, R. Hayes, J. Phys. Chem. B 107 (2003) 1634.

[46] Legendre, Dominique and Maglio, Marco Numerical simulation of spreading drops. (2013) Colloids and Surfaces A: Physicochemical and Engineering Aspects, vol. 432 . pp. 29-37. ISSN 0927-7757

[47] H. J. Jeong, W. R. Hwang, C. Kim, Numerical Simulations of the Impact and Spreading of a Particulate Drop on a Solid Substrate, Hindawi Publishing Corporation Modelling and Simulation in Engineering doi:10.1155/2012/687961

[48] J. B. Dupont, D. Legendre, Numerical simulation of static and sliding drop with contact angle hysteresis, Journal of Computational Physics 229 (2010) 2453–2478

[49] D. Deganello, T.N. Croft, A.J. Williams, A.S. Lubansky, D.T. Gethin, T.C. Claypole, Numerical simulation of dynamic contact angle using a force based formulation, Journal of Non-Newtonian Fluid Mechanics 166 (2011) 900–907

[50] Simon Van Mourik, Numerical modelling of the dynamic contact angle, Master Thesis - University of Groningen Department of Mathematics August 2002

[51] Petrov, P. G. and Petrov, J. G., 1995, Extrapolated dynamic contact angle and viscous deformation of a steady moving meniscus at a vertical at wall, Langmuir, 11 (8): 3261-3268.

[52] S. Van Mourik, A.E.P. Veldman, M.E. Dreyer, Simulation of Capillary Flow with a Dynamic Contact Angle, Microgravity sci. technol. XVII-3 (2005)

[53] V. Konduru, Static and Dynamic Contact Angle Measurement on Rough Surfaces Using Sessile Drop Profile Analysis with Application to Water Management in Low Temperature Fuel Cells, Master of Science (Mechanical Engineering) Michigan Technological University, 2010

[54] G. Fighera, Experimental investigation on the dynamic contact angle of water drops on stainless steel, Master Degree in Energy Engineering, 2013

[55] P. Di Marco, G. Saccone, Experimental study on the action of electric field on growing gas bubbles by measuring the variation of their curvature, 23rd International Symposium on Transport Phenomena Auckland, New Zealand 19–22 November 2012

[56] O. I. del Rio and A. W. Neumann. Axisymmetric drop shape analysis: Computational methods for the measurement of interfacial properties from the shape and dimensions of pendant and sessile drops. Journal of Colloid and Interface Science, 196:136–147, 1997.

[57] Cheng, Boruvka, Rotenberg, and Neumann. Automation of axisymmetric drop shape analysis for measurements of interfacial tensions and contact angles. Colloids and Surfaces, 43:151–167, 1990.

[58] A. Cattide, P. Di Marco, W. Grassi, Evaluation of the electrical forces acting on a detaching bubble, UIT National Congress 18-20 june 2007

[59] Di Marco P ., Giannini N., Saccone G., Experimental determination the forces acting on a growing gas bubble in quasi-static conditions, ECI 8th International Conference on Boiling and Condensation Heat Transfer, Lausanne, Switzerland, 1-10, (2012), CD-ROM.

[60] P. Di Marco, G. Saccone, Experimental Study on the action of electric field on growing gas bubbles by measuring the variation of their curvature, 23 rd International Symposium on Transport Phenomena, Auckland, New Zealand 19–22 November 2012

[61] Di Marco P., Forgione N., Grassi W., Quasi-static formation and detachment of gas bubbles at a submerged orifice: experiments, theoretical prediction and numerical calculations, XXIII UIT National Heat Transfer Conference, Parma, 20-22 Giugno 2005, pp.237-243.

[62] Pitts, E., The stability of pendent liquid drops. Part2. Axial symmetry, J. of Fluid Mech., 63, 1974, pp.487-508.

[63] Gerlach D., Bishwas G., Durst F., Kolobaric V., Quasi-static bubble formation on submerged orifices, Int. J. Heat Mass Transfer, 48, 2005, pp. 425-438.

[64] Padday J.F., Theory of surface tension, Surface and Colloid Sci., 1, 1969, pp. 39-253.

[65] F.K.Hansen; G. Rodsrun (1991). "Surface tension by pendant drop. A fast standard instrument using computer image analysis". Colloid and Interface Science 141: 1–12. doi:10.1016/0021-9797(91)90296-K.

[66] Roger P. Woodward, Ph.D. Surface Tension Measurements Using the Drop Shape Method (PDF). First Ten Angstroms. Retrieved 2008-11-05.

[67] Panton R.L., Incompressible Flow, 3rd ed., Wiley, 2005, ch.23.

[68] D. Erickson, B. Blackmore, D. Li, "An energy balance approach to modelling the hydrodynamically drive spreading of a liquid drop, Colloids and Surfaces A: Physicochem. Eng. Aspects 182 (2001) 109–122.

[69] R.N. Wenzel, Ind. Eng. Chem. 28, p988, 1936.

[70] K.J. Kubiak, M.C.T. Wilson , T.G. Mathia , Ph. Carval, Wettability versus roughness of engineering surfaces, Vol. 271, Issues 3–4, 3 June 2011, Pages 523–528, The 12th Int. Conf. on Metr. & Prop. of Eng. Surfaces.

[71] Jansons, K. M. 1985 Moving contact lines on a two-dimensional rough surface. J. Fluid Mech. 154, 1–28.